Forschungsbericht 2024-16

Design and Validation of Motion Sickness Models for Rotorcraft

Philippe Joseph Petit

Deutsches Zentrum für Luft- und Raumfahrt
Institut für Flugsystemtechnik
Braunschweig

Deutsches Zentrum
DLR für Luft- und Raumfahrt

Forschungsbericht 2024-16

Design and Validation of Motion Sickness Models for Rotorcraft

Philippe Joseph Petit

Deutsches Zentrum für Luft- und Raumfahrt
Institut für Flugsystemtechnik
Braunschweig

150 Seiten
57 Bilder
21 Tabellen
82 Literaturstellen

Deutsches Zentrum
DLR für Luft- und Raumfahrt

Herausgeber:

Deutsches Zentrum
für Luft- und Raumfahrt e. V.
Wissenschaftliche Information
Linder Höhe
D-51147 Köln

ISSN 1434-8454
ISRN DLR-FB-2024-16
Erscheinungsjahr 2024
DOI: 10.57676/ycwq-9c52

Modellierung von Luftkrankheit, Vorhersage, Bewegungssimulatoren, Kinetose, Bewegungskrankheit, Hubschrauber, e-VTOL, Passagierkomfort, Flugregelung, Flugtests,

Philippe Joseph PETIT
Deutsches Luft- und Raumfahrtzentrum (DLR), Institut für Flugsystemtechnik, Braunschweig

Entwurf und Validierung von Kinetosemodellen für Drehflügler

Dissertation, Technische Universität Braunschweig

Bei modernen Entwicklungen wie beispielsweise elektrischen Lufttaxis wird vermehrt Wert auf einen erhöhten Komfort für Piloten und Passagiere im Flug gelegt. Als Unterstützung dieser Entwicklung behandelt die vorliegende Arbeit die Erstellung eines Modells zur simulativen Vorhersage der Luftkrankheit, fachsprachlich auch als Kinetose bezeichnet. Zu diesem Zweck wurden verschiedene Modelle zur Vorhersage von Kinetose auf ihre Eignung bewertet. Nach der Selektion und Anpassung eines geeigneten Modells wurden dessen Parameter mittels einer numerischen Optimierung nochmals verbessert. Die Basis für diese Optimierung bilden experimentelle Resultate aus Literaturquellen.

Das resultierende Modell wurde anschließend anhand einer Reihe von Hubschrauber-Flugversuchen mithilfe des Bölkow BO-105 Hubschraubers des DLR und insgesamt 32 Versuchspersonen validiert. Hierbei wurde die durch das Modell prädizierte Kinetose mit der im Flugversuch beobachteten Kinetose verglichen. Mehrere Hilfssysteme mussten im Rahmen dieser Flugversuche entwickelt werden, um sowohl die Datenaufnahme flugdynamischer Parameter, als auch die akkurate Einhaltung der vorgegebenen Rollschwingung im Flug zu ermöglichen.

Eine Analyse dieser Ergebnisse zeigt, dass das entwickelte Kinetose-Modell zur Vorhersage mittelschwerer Kinetose besonders geeignet scheint.

Modelling of motion sickness, Prediction, Motion simulators, Kinetosis, motion sickness, Rotorcraft, e-VTOL, Passenger comfort, Flight control, Flight test

(Published in english)

Philippe Joseph PETIT
German Aerospace Center (DLR), Institute of Flight Systems, Brunswick

Design and Validation of Motion Sickness Models for Rotorcraft

Dissertation, Technische Universität Braunschweig

In modern developments such as electric air taxis, higher emphasis is placed on increased passenger and crew comfort in flight. To support this effort, the present thesis deals with the creation of a motion sickness prediction model for rotorcraft aimed at predicting motion sickness also known as kinetosis. For this purpose, various prediction models and standards were evaluated. After selecting and adapting a suitable model, its parameters were further improved via numerical optimization based on the results of experimental motion sickness studies taken from literature.

The resulting motion sickness model was then validated using a series of helicopter flight tests with a total of 32 test subjects onboard DLR's Bölkow BO-105 helicopter, in which the kinetosis predicted by the model was compared to motion sickness observed in the flight test. Multiple support systems had to be developed as part of these flight tests, on the one hand to enable the recording of flight dynamics data and on the other hand to enable accurate tracking of the desired roll oscillation by the pilot in flight.

An analysis of the results shows that the developed motion sickness model appears to be particularly suited for predicting moderate levels of kinetosis.

TU Braunschweig – Niedersächsisches
Forschungszentrum für Luftfahrt

Berichte aus der Luft- und Raumfahrttechnik

Forschungsbericht 2024-13

Design and Validation of Motion Sickness Models for Rotorcraft

Philippe Joseph Petit

Deutsches Zentrum für Luft- und Raumfahrt
Institut für Flugsystemtechnik

Braunschweig

Diese Veröffentlichung wird gleichzeitig in der Berichtsreihe „NFL - Forschungsberichte“ geführt.

Diese Arbeit erscheint gleichzeitig als von der Fakultät für Maschinenbau der Technischen Universität Carolo-Wilhelmina zu Braunschweig zur Erlangung des akademischen Grades eines Doktor-Ingenieurs genehmigte Dissertation.

Design and Validation of Motion Sickness Models for Rotorcraft

Von der Fakultät für Maschinenbau
der Technischen Universität Carolo-Wilhelmina zu Braunschweig

zur Erlangung der Würde

eines Doktor-Ingenieurs (Dr.-Ing.)

genehmigte Dissertation

von:	Philippe Joseph Petit
geboren in (Geburtsort):	München

eingereicht am:	22.06.2023
mündliche Prüfung am:	09.02.2024
Vorsitz:	Prof. Dr.-Ing. P. Hecker
Gutachter	Prof. Dr.-Ing. S. Levedag Prof. Dr.-Ing. S. Langer Prof. Dr.-Ing. M. Vollrath

2023

Abstract

Keywords: *Motion sickness modeling, Flight control, Avionics*

Design and Validation of Motion Sickness Models for Rotorcraft

Modern developments such as electric VTOL aircraft for use in urban terrain or new rotary wing concepts increasingly emphasize comfort of ride for pilots and passengers in flight. To support this effort, the present thesis deals with the creation of a model for the prediction of motion sickness specifically focused on air sickness. Especially for the design of flight control systems or trajectories of modern rotorcraft, such prediction models may crucially contribute to commercial success. For this purpose, different motion sickness prediction models were investigated and compared. After selecting and adapting a suitable model, its parameters were further improved by means of numerical optimization whereby the basis for this optimization was formed by experimental results of motion simulators from literature sources.
In order to validate the resulting model, flight tests were scheduled using DLR's BO-105 helicopter. Multiple support systems had to be developed as part of these flight tests, on the one hand to enable the recording of flight dynamic data and on the other hand to enable accurate tracking of the desired roll oscillation by the pilot in flight. In addition, appropriate questionnaires were designed and filled out by the test subjects during the flight.
The work concludes with a comparison between the predicted motion sickness based on the recorded flight data and the motion sickness observed during the flight test. Analyzing the results of the test flights it was shown that the developed model seems appropriate for predicting moderate motion sickness.

Kurzfassung

Schlagwörter: *Modellierung von Luftkrankheit, Flugsteuerung, Avionik*

Entwurf und Validierung von Kinetosemodellen für Drehflügler

Moderne Entwicklungen wie beispielsweise elektrische VTOL Luftfahrzeuge für den Einsatz im urbanen Gelände oder aber neuartige Drehflügelkonzepte legen vermehrt Wert auf einen erhöhten Komfort für Piloten und Passagiere im Flug. Als Unterstützung dieser Entwicklung behandelt die vorliegende Arbeit die Erstellung eines Modells zur simulativen Vorhersage der Luftkrankheit, fachsprachlich auch als Kinetose bezeichnet. Insbesondere für den Entwurf von Flugsteuerungssystemen oder aber die Auslegung von geeigneten Trajektorien von Hubschraubern und anderen Drehflüglern kann diese Vorhersage entscheidend zum kommerziellen Erfolg beitragen. Zu diesem Zweck wurden verschiedene Kinetosevorhersagemodelle untersucht und in Bezug auf ihre Eignung bewertet. Nach der Selektion und Anpassung eines geeigneten Modells wurden dessen Parameter mittels einer numerischen Optimierung nochmals verbessert. Die Basis für diese Optimierung bildeten experimentelle Resultate von Bewegungssimulatoren aus Literaturquellen.
Um das hieraus resultierende Modell zu validieren, wurden Flugversuche mithilfe des DLR Hubschraubers vom Typ BO-105 durchgeführt. Mehrere Hilfssysteme mussten im Rahmen dieser Flugversuche entwickelt werden, um sowohl die Datenaufnahme flugdynamischer Parameter, als auch die akkurate Einhaltung der vorgegebenen Rollschwingung im Flug zu ermöglichen. Des Weiteren wurden entsprechende Fragebögen ausgearbeitet, die vor und während des Fluges durch die Testpersonen ausgefüllt wurden.
Die Arbeit schließt ab mit einem Vergleich zwischen der prädizierten Kinetose, die anhand der aufgezeichneten flugdynamischen Parameter getroffen wurde, sowie der während des Flugversuchs beobachteten Kinetose. Eine Analyse dieser Ergebnisse zeigt, dass das entwickelte Modell zur Vorhersage mittelschwerer Kinetose besonders geeignet scheint.

Acknowledgment

The journey in completing this project was challenging but also deeply fulfilling. For this reason I would like to thank some people who have helped me along the way.
First and foremost I would like to express my deep gratitude for my advisor, Prof. Stefan Levedag on whom I could always rely for sharing his knowledge and expertise. His continued support and many fruitful discussions made this thesis possible.
I also would like to thank the late Prof. Michael J. Griffin for sharing his insights into the field of motion sickness as well as sharing the papers of his group. Special thanks also goes to Prof. Jelte Bos who shared his large knowledge on motion sickness based on countless years of research on this topic. I learned a lot during our discussions and I cannot emphasize enough how I benefited from this contact.
I would also like to thank my group at the Institute of Flight Systems Department of Helicopters, especially my group leader Daniel Nonnenmacher who always supported this project in every possible way. Special thanks go to Frederick Döring for our many discussions in which I learned a lot about control theory but which must have drawn a lot of energy from him! Without any special order I would additionally like to thank my colleagues and friends Johannes Wartmann, Alexej Dikarew, Daniel Müller, Arti Kalra, Benjamin Fragnière, Tobias Winkler, Steffen Greisser, Rafael Paintner, Reinhard Lojewski and many others who I forgot to mention. Without your support, discussions and laughter the past years would have been not only impossible but also much more dull. I also would like to especially thank Klaus Alvermann who supported me in more ways than the knows and from whom I learned more than he knows. Thanks to you all!
I am also very grateful for the support of the Department of Flight Experiments who operate DLR's BO-105 Helicopter. Especially Elizabeth Buron for her organizational skills which made the flight test possible! Additionally, my thanks go to our test pilots Uwe Göhmann and Sebastian Soffner who not only piloted the flight tests, but also guided me through designing and testing the entire setup. Without their knowledge and dedication these would not have been as successful as they were! Finally the entire flight crew of the BO-105 was willing to work extra hours in order to accommodate these tests and the underlying schedule, I am very grateful for this support.
I would like to sincerely thank my parents Marc and Irmgard Petit for the unwavering

support during my studies and my work. Their encouragement and guidance has led me to this point, which must have been difficult at times to say the least. Without you, all of this truly would not have been possible. I also want to thank my brother and sister who not only set wonderful examples but also offered their continuous friendship and support.
Last, but by no means least, I would like to thank my love Constanze for her love, appreciation and support during all phases of life and especially this project. I am deeply grateful for our love and friendship, and I cannot wait for our next adventures together.

Contents

List of Figures

List of Tables

Nomenclature

Latin Symbols

Symbol	Description	Unit
A_{dis}	Displacement amplitude	m
a	UKF weight matrix parameter	-
a_x	Acceleration, x-axis	$\mathrm{m/s^2}$
a_y	Acceleration, y-axis	$\mathrm{m/s^2}$
a_z	Acceleration, z-axis	$\mathrm{m/s^2}$
$a_{z,w}$	Frequency weighted acceleration, z-axis	$\mathrm{m/s^2}$
$\mathbf{B}$	Input matrix of dynamic system	-
b	UKF weight matrix parameter	-
$\mathbf{C}$	UKF smoother Cross-covariance matrix	-
c	Motion sickness conflict	-
$\mathbf{D}$	UKF smoother gain matrix	-
d	UKF weight matrix parameter	-
$\mathbf{F}$	State transformation matrix	-
$\mathbf{f}(.)$	System dynamics update function	-
f	Frequency	Hz
$\mathbf{g}$	Earth gravitational vector	$\mathrm{m/s^2}$
g	Earth gravitational constant	$\mathrm{m/s^2}$
$\mathbf{H}$	Observation matrix of linear dynamic system	-
$\mathbf{h}(.)$	System dynamics measurement function	-
$I_{susc.(yr.)}$	Illness susceptibility in transport in the past year	-
$I_{travel(yr.)}$	Illness frequency while traveling in the past year	-
$\mathbf{K}$	Kalman gain matrix	-
K_a	Gain for acceleration estimation of internal model	-
K_{ac}	Integration constant acceleration difference	-
K_{out}	Output gain for improved Kamiji model	-

continued on next page

K_{vc}	Integration constant subjective vertical difference	-
K_{ω}	Gain for acceleration estimation of internal model	-
$K_{\omega c}$	Integration constant rotation rates difference	-
k	UKF weight matrix parameter	-
M_{total}	Total susceptibility to motion sickness	-
$MSDV_z$	Motion sickness dose values	-
$\mathbf{m}$	Motion parameter vector	-
n	Number of system states of dynamic system	-
$\mathbf{P}$	State covariance matrix of dynamic system	-
$\mathbf{p}$	Parameter vector for the improved Kamiji model	-
p	Rotational rate x-axis	$\mathrm{rad/s}$
$\mathbf{Q}$	Process noise covariance matrix	-
q	Rotational rate y-axis	$\mathrm{rad/s}$
$\mathbf{R}$	Measurement noise covariance matrix	-
$\mathbf{R}_{21}$	Rotation matrix from system 1 to system 2	-
R_i	Sum of ranks of i-th sample	-
R_{ij}	Rank of i-th sample of j-th observation	-
Rc_{xy}	Cross-correlation between signals x and y	-
r	Rotational rate z-axis	$\mathrm{rad/s}$
$\mathbf{S}$	Cholesky factor of the state covariance matrix $\mathbf{P}$	-
s	Parameter of the Laplace transform	-
T	End time	-
$T_{(yr.)}$	Travel frequency in the past year	
t	Time	s
U	U-value of the Mann-Whitney U test	-
$\mathbf{u}$	Input vector of dynamic system	-
V_{TAS}	True airspeed	$\mathrm{m/s}$
V_{GPS}	Groundspeed measured by the GPS	$\mathrm{m/s}$
$V_{travel(yr.)}$	Vomiting frequency while traveling in the past year	-
$\mathbf{v}$	Measurement noise vector of dynamic system	-
W_E	Wind East	$\mathrm{m/s}$
W_N	Wind North	$\mathrm{m/s}$
$\mathbf{w}$	Process noise vector of dynamic system	-
$\mathbf{w}_c$	UKF Weight matrix for covariance matrix	-
$\mathbf{w}_m$	UKF Weight matrix for mean state vector	-
w_c^i	i-th UKF Weight for $\mathbf{w}_c$	-

continued on next page

w_m^i	i-th UKF Weight for $\mathbf{w}_m$	-
$\mathbf{X}$	UKF unweighted state matrix	-
$\mathbf{X}_s$	Sigma points vector	-
$\mathbf{x}$	State vector of dynamic system	-
x	x-Position	m
$\mathbf{y}$	Vector of motion sickness values	-
y	y-Position	m
$\mathbf{Z}$	UKF unweighted measurement matrix	-
$\mathbf{z}$	Measurement vector of dynamic system	-
z	z-Position	m

Greek Symbols

Symbol	Description	Unit
Δ	Difference between values	-
θ	Euler angle - pitch	rad
τ	Low-pass time constant for subjective vertical estimation	
τ_a	Time constant 'a' for semicircular canals model	
τ_d	Time constant 'd' for semicircular canals model	
φ	Euler angle - roll	rad
ψ	Euler angle - yaw	rad
ω	Oscillation frequency	Hz

Subscripts

Symbol	Description
B	Body Frame

continued on next page

B’	Canted smartphone installation body frame
E	NED Frame
Griffin	Griffin dataset
H	Head frame
i	Inertial frame
k	k-th Time-step
SM	Smartphone
sim	Simulation dataset

Superscripts

Symbol	Description
$\square^{s}$	Smoothed quantity via UKF smoother
$\hat{\square}$	Estimated quantity
$\bar{\square}$	Mean quantity
$\underline{\square}$	Matrix arranged from vectors as shown in Eq. (3.79)

Acronyms

Acronym	Description
ACT/FHS	Active Control Technology/Flying Helicopter Simulator
AFCS	Automatic Flight Control System
AHRS	Attitude Heading Reference System
APT	Advanced Passenger Train
AVES	Air Vehicle Simulator
DLR	Deutsches Zentrum für Luft- und Raumfahrt

continued on next page

GPS	Global Positioning System
HAE	Height above ellipsoide
HAGL	Height above ground level
HHC	Higher Harmonic Control
IBC	Individual Blade Control
IMU	Inertial Measurement Unit
INS	Inertial Navigation System
LIDAR	Light Detection And Ranging
MEMS	Micro-Electro-Mechanical System
MSD	Motion Sickness Degree
MSDV	Motion Sickness Dose Value
MSI	Motion Sickness Incidence
NDA	Non-disclosure Agreement
OS	Operating System
PFD	Primary Flight Display
PMSD	Percentage of people reaching a motion sickness degree of (number between 1 and 6)
RASCAL	Rotorcraft Aircrew Systems Concepts Airborne Laboratory
UAM	Urban Air Mobility
UKF	Unscented Kalman Filter
URTSS	Unscented Rauch-Tung-Striebel Kalman Smoother
VFR	Visual Flight Rules
VTOL	Vertical Take-off and Landing

1 Introduction and Problem Formulation

Rotorcraft vehicles in general and helicopters in particular represent established tools for a multitude of tasks such as air rescue, the transport of people and material or for military use. The unique capability these vehicles possess is the ability to hover in mid-air, which enables them to accurately take off or land in confined spaces and therefore to execute missions no other airborne vehicle is capable of. These traits make rotorcraft vehicles essential for a wide variety of uses.

(a) DLR's Active Control Technology/Flying Helicopter Simulator in flight

(b) The RASCAL helicopter [1]

Figure 1.1: Two helicopter research demonstrators centered around concepts for automatic flight control systems

Increasing miniaturization of electronics and associated digitization of avionic systems has introduced many changes in the aviation industry. Amongst the most prominent in respect to rotorcraft might be the introduction of fully digital automatic flight control systems (AFCS), which massively facilitate the control of rotorcraft. By coupling a digital flight control computer with the input sticks of the pilots and a suitable set of sensors, the AFCS can compute a series of appropriate steering commands which stabilizes the helicopter during flight. These systems do not only improve the handling qualities of the helicopers while lowering the pilot workload, but as research efforts by DLR have

shown, such systems can furthermore support or completely overtake a variety of missions from the pilot. An integrated anti-sway system was researched and tested at DLR, which is intended to either simplify or completely automate the external slung-load transport in helicopters in order to ultimately reduce the pilot's workload [2, 3]. This system was then demonstrated in flight onboard the Active Control Technology/Flying Helicopter Simulator (ACT/FHS), DLR's modified Airbus Helicopter EC 135 helicopter equipped with a reprogrammable fly-by-wire/fly-by-light AFCS as depicted in Fig. 1.1a. Furthermore, automatic environment and obstacle perception were developed, implemented and demonstrated in flight, using this helicopter in combination with a Light Detection And Ranging (LIDAR) sensor. This system combination led to the demonstration of an automatic landing approach during flight trials in Brunswick [4]. Other similar research activities have been carried out by the NASA Ames Research Center, whereby a modified JUH-60A Black Hawk helicopter, named RASCAL, equipped with an AFCS and LIDAR sensor was used to also demonstrate automatic approach and landing at unprepared landing sites [1, 5]. The RASCAL demonstrator is depicted in Fig. 1.1b.

1.1 Urban Air Mobility Concepts

Such advances in digital flight control technology also enable the new (envisioned) Urban Air Mobility (UAM) vehicles, as depicted in Fig. 1.2. Under the umbrella term UAM [6], several typically electric Vertical Take-off and Landing (VTOL) concepts are currently being developed, which shall be deployed in urban areas for passenger transport. The advantage of these concepts is that on the one hand they can land in very confined spaces due to their VTOL capabilities and on the other hand can bridge large distances in a short time because of the utility of airborne transport. The idea is that a customer digitally calls the UAM vehicle to a suitable landing spot, he/she will board the aircraft which will then transport the passenger to the destination. Additionally, the lower emissions both in noise and exhaust gases favor their integration in urban areas. Such vehicles shall ultimately enable fast and cheap transport for densely populated areas which otherwise suffer extreme traffic congestion [6].
It is important to note that a key enabler for UAM vehicles is that of autonomous flight. While first stages of deployment are planned with safety-pilots onboard, later stages heavily lean on autonomy to reduce weight and the need for highly specialized personnel. Only the absence of a pilot allows sufficient scalability of transport services and therefore a low enough price for a majority of potential customers.

(a) The Volocity concept by Volocopter [7]

(b) The Joby Aircraft prototype in flight by Joby Aviation [8]

Figure 1.2: Two Urban Air Mobility concepts

1.2 Vibrational Discomfort

Future helicopters and new concepts such as that of UAM rely heavily on automation up to and including autonomy. However, this increasing focus on the AFCS push previous design methods for these systems to their limits. Design recommendations such as the widespread „ADS-33 - Handling Qualities Requirements for Military Rotorcraft“ [9] contain some guidelines for the design of control behavior and autopilots for helicopters, but there are no recommendations for autonomous flight segments.
However, a well-adapted design of the autonomous flight can be quite important. With conventional helicopters, the stated goal is to decrease the workload of a pilot by increased automation. If the pilot loses confidence in the automatic systems, the effectiveness of the system is lost. The same principle also applies to passenger transport with the help of autonomous aircraft: The more likely it is that passengers feel uncomfortable or find an uncomfortable environment while utilizing such vehicles, the more likely they are to look for conventional alternatives. The Volocopter white paper states this as follows: "The customer is at the center of the UAM ecosystem. Customers determine all passenger-related demands for air taxi services. People will only adopt the services and remain loyal to them if they meet their expectations, spark excitement and delight, and deliver the promised value offering" [10].
The engineer is therefore faced with the task of not only enabling the aircraft's autonomy, but also of doing this in such a way that the pilot and passenger will *want* to use it. Of course, the AFCS, responsible for generating the steering commands which ultimately fly the helicopter, plays a special role here. In autonomous flight, the AFCS takes control of the aircraft and steers it to its destination along the predetermined or dynamically determined trajectory. The design of the AFCS thus determines how the

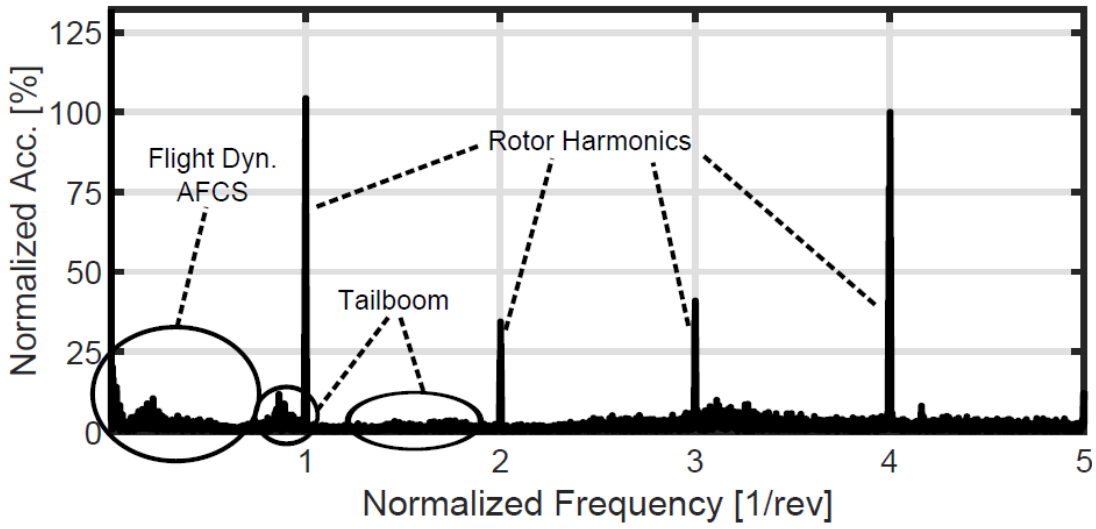

Figure 1.3: Relevant helicopter vibration sources in the spectrum, taken from [14]

pilot or the passenger evaluates the flight.
This places an increased focus on the comfort of ride of such a vehicle, and therefore especially in the context of rotorcraft, on the reduction of vibrations during flight. The topic of reducing such vibrations has accompanied the helicopter industry for a long time and many methods have been conceived to rate [11] and to alleviate vibrations of rotorcraft. The typical vibration spectrum of a helicopter is displayed in figure 1.3, normalized to the main rotor frequency. The most predominant vibrations are those associated with the main rotor frequency and multiples of this frequency. This motivates the focus of traditional vibrational alleviation techniques such as passive vibration isolation [12], which already reduced the vibration level of around 0.3 - $0.6\,\mathrm{g}$ in the 1950s to around $0.1\,\mathrm{g}$ in 1985 as shown in [13]. Newer research increasingly focuses on active technologies like Higher Harmonic Control (HHC) or Individual Blade Control (IBC), which in one form or the other try to actively control the angle of attack of the rotorblades in order to reduce vibration induced by aerodynamic loads [15].
As can be seen in figure 1.3, these are however not the only source of vibration in traditional helicopters. For the new application of UAM, such techniques do not necessarily apply at all, since UAM vehicles may not possess a traditional main rotor system, but rather rely on an array of propellers. Other vibration sources include structural vibrations and effects of the AFCS.
As noted by the ISO 2631-1 standard [16], the relevant vibrational spectrum falls into two categories, classified as motion sickness on the one hand and health, comfort and perception on the other hand as displayed in Table 1.1. Of these two types of vibration, a typical well-design AFCS can only influence the spectrum associated with motion sickness. This conclusion can also be reached if comparing Table 1.1 with Fig. 1.3. The main rotor frequency of an EC 135 is around $6.5\,\mathrm{Hz}$, therefore the area indicating

"Flight Dyn. AFCS" in Fig. 1.3 lies approximately at the frequency band responsible for motion sickness. The argument becomes even more evident by considering the ADS-33 AFCS recommendation which states that the most desirable (level 1) handling qualities for pitch/roll lies at most (Target Acquisition and Tracking) at a frequency of around $0.32\,\mathrm{Hz}$ $(2\,\mathrm{rad/s})$ for pitch, and $0.4\,\mathrm{Hz}$ $(2.5\,\mathrm{rad/s})$ for roll [9, Fig. 5, p. 75]. For this reason, it is concluded that the vibration spectrum which can be best influenced by the AFCS is the one responsible for motion sickness.

Table 1.1: ISO 2631 Classification of vibrational discomfort frequency range

Frequency (Hz)	Classification
0.1 - 0.5	Motion sickness
0.5 - 80	Health, comfort and perception

1.3 Motion Sickness

So what is motion sickness? According to [17], motion sickness is a malady "[...] caused by certain kinds of motion. The signs and symptoms include malaise, pallor, cold sweating, nausea, and vomiting".
Motion sickness is also known as kinetosis in a scientfic context but more often referred to as seasickness, airsickness, carsickness, simulatorsickness etc. It also should be noted, that motion sickness is gradual in symptoms. At first, people generally feel unwell, before developing stronger symptoms whereby (repeated) vomiting can be seen as the ultimate manifestation of motion sickness. It should be further noticed that people can get accustomed to the motion causing the motion sickness. This is illustrated by the fact that during military training, 5.7% of student pilots suffer from motion sickness during their first training flight, while on the 10th flight this percentage dropped to 1.1% [17, p. 2]. However, it should be noted that especially in the military context, denial or alternate interpretation of symptoms can be expected, which might lead to these numbers being low in general. Nevertheless, the general trend of accustomization can also be frequently observed in other examples such as seafaring. It was observed that at moderate turbulences at sea, $25 - 30\%$ become severly motion sick during the first days of an atlantic crossing [17].

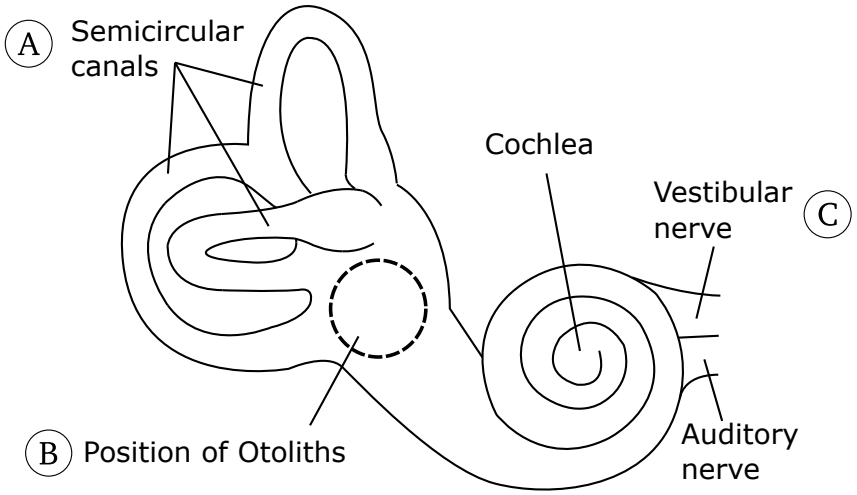

Figure 1.4: Sketch of the inner ear, taken with adaption from [18]

1.3.1 Conflict Theory

Probably the most accepted theory for the cause of motion sickness is the "conflict theory"[1] [17,19,20]. This theory, first developed by Reason and brand [21], postulates that motion sickness arises from a conflict of sensory inputs between the vestibular system and the eye.

The vestibular system consist of the semicircular canals (or semicircular ducts) (A) and the otolithic organ (or otoliths) (B) as depicted in Fig. 1.4. To enable the semicircular canals to detect rotary motion, this organ consists of three fluid-filled canals or ducts, which are oriented orthogonally to one another. Due to inertia, the fluid inside these ducts moves relative to the canals when the head is rotated, whereby the fluid flow is detected by hair cells called crista amullaris. The corresponding nerve impulse is then transmitted to the brain via the vestibular nerve (C) [22]. Such a system can be compared very well to its technical counterpart, the "Gyroscope", which also detect rotary movement.

The second part of the vestibular system called the otolithic organ (B), is responsible for detecting translational movement and can be compared to the working of modern "accelerometer", as they determine translational movement with the help of flexibly-mounted small mass which due to inertia resists movement change. This information is again detected by small hair cells and transported to the brain via the vestibular nerve (C) [22]. It is therefore evident that the vestibular system contains the same "building blocks" as a modern Inertial Measurement Unit, or short IMU, namely that of independent rotary and translatory movement detection. Such IMUs can be found in many technical applications from airplanes to smartphones.

[1] sometimes also called "sensory conflict theory" or "sensory rearrangement theory"

In the case of the eye, movement of the head is determined by the visual scene. A technical counterpart of such a system could be optical flow techniques which estimate the subjective movement by tracking certain features in a given set of images over time.
The ability to judge a motion conflict between the eye and the vestibular system is an acquired skill. Over the lifetime, a human learns what movement and therefore sensor information to expect given specific movements. For example tilting, or nodding the head creates a specific sequence of stimuli of the eye and the vestibular system, which is learned to be a normal movement.
The conflict theory now states that if a human receives stimuli from the vestibular system as well as from the eye which contradict each other given his subjective learning history, a motion conflict arises which manifests as motion sickness. Typically, this is triggered by unusual motions which are not often experienced in everyday life featuring high centrifugal forces such as riding on a tilting train or flying in an aeroplane. However, if a human is repeatedly exposed to a motion sickness inducing environment or movement, he/she will get accustomed to this type of motion and will no longer experience motion sickness, something that can be observed, for example, in people experiencing seasickness.

1.3.2 Railway Research on Motion Sickness and Active Control

Figure 1.5: The Advanced Passenger Train, taken from [23]

Avoiding motion sickness on vehicles is not a problem exclusive to flying vehicles like aircraft, helicopters and UAM vehicles. The first similar application, in which the roll angle of the vehicle was actively controlled, historically occurred with the introduction of the first tilting train, the Advanced Passenger Train (APT) displayed in Fig. 1.5, which was first put into service in 1981. Originally, tilting trains were conceived for traversing curvy tracks faster than conventional trains. A feature especially useful for countries with either very rugged topography (e.g. Sweden), numerous legacy tracks with tighter

curve radii then conventional tracks (e.g. Great Britain) or a combination of both (e.g. Japan). Tilting trains were envisioned to be faster on such curvy tracks while not exceeding lateral forces inside the passenger train when traversing curves at high speeds. However, it was soon discovered that while the general concept of tilting trains worked in practice, it presented new technical challenges. Amongst these was also the fact that this new technology provoked motion sickness amongst its passengers, a fact which led the British press to nickname the APT the "queasy rider". This, and other technical problems ultimately led to the abandonment of the APT in favor of more conventional albeit slower trains. Eventually, tilting trains were reintroduced to Great Britain in 2002 in form of the Pendolino trains manufactured by the French company "Alstom". The relevant patents for the tilting train technology was sold to "Fiat" in the aftermath of the APT failure. Fiat then used these patents to supply tilting train technology for the Pendolino trains, which are also used in the UK.

Today a wide variety of tilting trains are in service, with a matching variety of strategies to alleviate motion sickness incidence onboard these trains through suitable control of the tilting mechanism. A common feature of several strategies is to reduce the "compensation" [24, 25]. This term describes the amount of lateral acceleration which is not "compensated for" by tilting of the vehicle. As an example, 70% compensation would mean that the train is tilted such that the passenger only observes 30% of the original lateral acceleration. In aerospace terms, this can also be described as follows: When a vehicle is moving through a curve, it is subject to gravitational acceleration and lateral acceleration (seen from the inertial frame). The body of the vehicle is now rotated around the roll-axis such that the z-axis of body frame aligns with the resulting force acting upon the passenger. When a compensation of less than 100% is chosen, the roll-axis is rotated to only a certain percentage of the lateral acceleration.
Förstberg et al. [24] determined via empirical trials including 80 passengers on six different settings aboard Swedens X2000 train that the ideal compensation is 55% for these trains. Other studies also found that less then 100% compensation reduces motion sickness [26] to a higher amount than full compensation. A slightly different approach was

Table 1.2: Motion sickness scale as used by Suzuki et al. [27]

1	Not wholly uncomfortable
2	Slightly irritating
3	Uncomfortable, but in the acceptable range of railway riding comfort
4	Extremely uncomfortable and not acceptable as railway riding comfort

taken by Suzuki et al. [27]. This study does not explicitly target motion sickness, but rather aims at rating ride comfort directly. For this, 293 test subjects evaluated riding

comfort on curved sections of track, rating comfort/discomfort on a scale from one to four as displayed in Table 1.2.

Suzuki et al. derived from these tests two distinct comfort rating criteria, one for standing one for sitting passengers.

$$\text{Standing:} \quad TC_{-TR} = 0.6 \cdot \ddot{y} + 0.3 \cdot \dddot{y} + 0.03 \cdot \dot{\varphi} + 0.12 \cdot \ddot{\varphi} + 0.5 \tag{1.1}$$

$$\text{Seated:} \quad TC_{-TZ} = 0.4 \cdot \ddot{y} + 0.4 \cdot \dddot{y} + 0.02 \cdot \dot{\varphi} + 0.04 \cdot \ddot{\varphi} + 0.8 \tag{1.2}$$

with $\ddot{y}$ denoting maximum lateral acceleration, $\dddot{y}$ maximum jerk, $\dot{\varphi}$ maximum roll velocity and $\ddot{\varphi}$ maximum roll acceleration. Note that in contrast to motion sickness models, such a model has a broader scope of rating comfort directly. It also has the advantage of having clear and directly comparable metrics suited for informing the design of a control algorithm for tilt control.

The downside to all of these empirical metrics and models which are determined via on-track tests is that they are tailored to the specific train they were tested on. Therefore, no general correlation between motion variables and motion sickness or discomfort can be identified [28]. This is especially problematic for the transfer of these metrics and models to flying vehicles, as the involved magnitudes of acceleration and velocities are vastly different.

1.4 Trajectory and Motion Assumptions

Before defining a scientific question, it is worthwhile to think about a typical trajectory and expected motion of rotorcraft vehicles. This will help to identify the work needed to improve the comfort level of these vehicles. The following section will hereby concentrate on UAM vehicles.

1.4.1 Urban Air Vehicles

At the time of writing, no commercial UAM route has been put into service, therefore no real-life trajectories can be taken as example. However, as the name already states, these types of aerial vehicles are intended to fly in an urban environment. Manufactures and operators published white papers [6, 10], which hint towards relevant parameters

for such trajectories. Together with these sources, it is easy to see that the urban environment together with the intended high density of flight traffic from UAM vehicles forms a highly challenging air space. No-fly zones will be most likely erected over sensitive infrastructure such as powerplants, airports, military infrastructure etc. but also above inner city districts and sensitive buildings like schools and nurseries. On the other hand, because high air traffic is predicted, a suitable advance air traffic management system and integrated collision avoidance strategies are proposed by these white papers. Such a system will be a challenging factor in the introduction of UAM vehicles as it needs to account for numerous shareholders such as commercial aviation, police, rescue helicopter operations, and drone operations [10].
Another factor for UAM vehicles is the effect of turbulence on the vehicle. Especially during the start and landing phase, the vehicle operates close to the ground and potentially also close to obstacles which may lead to atmospheric turbulence and in turn affect the flight of that aircraft. Especially for fixed-pitch speed-controlled multi-rotor concepts with limited control bandwidth [29], this may lead to significant uncommanded translational and rotational motions [30].
All of this combined makes it clear that a UAM trajectory will **not** be a straight path from origin to destination as implied for example by the uber white paper [6]. In the scope of this thesis, it is argued that the flight path of future UAM vehicle over urban areas will rather consist of a high number of turns interconnected with straight lines. Additionally, it will be assumed that the trajectory will be "flat", therefore the UAM vehicle will mostly perform horizontal maneuvers, while vertical maneuvers are only needed for start and landing of the vehicles including climbing/descending phases. The reason for this assumption is that while collisions with other air traffic can be avoided by vertical maneuvering, most other obstacles will be evaded by horizontal maneuvering. Additionally, atmospheric turbulence are neglected as these are assumed to act mostly during the start and landing phase and therefore are of short duration. These assumptions also significantly simplifiy the process of setting the envelope of a suitable motion sickness model.
Note that horizontal maneuvering of almost all man-carrying vehicles use the horizontal "bank-to-turn" strategy in order to change their heading. This maneuver is characterized by the fact that during a heading change or horizontal turn the aerial vehicle rolls around its longitudinal axis (banks) in order to compensate the lateral centrifugal force of the turn as illustrated in figure 1.6. During this maneuver the altitude of the vehicles stays constant. The typical motions implied by this motion are the rotatory motion of banking, followed by a slight increase in vertical acceleration of the vehicle (because of the vector addition of gravitational and centrifugal forces). As a worst case scenario, the riding passengers are assumed to never have experienced this mode of transport.

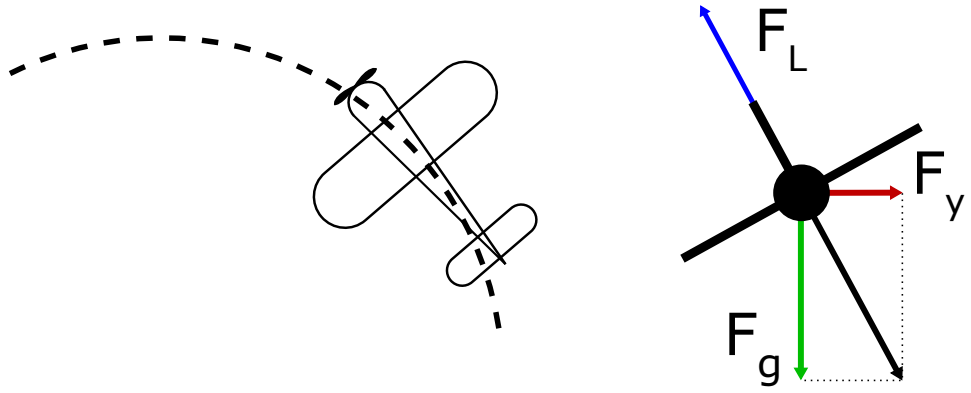

Figure 1.6: View from top and behind of a turning airplane, employing the bank-to-turn strategy. F_g is the gravitational force, F_y the centrifugal force and F_L the lift force of the aircraft

Regarding the time length of the envisioned flight path, it is assumed that it ranges between 10 and 30 minutes as specified in the uber white paper [6].
Additionally, we assume that the passengers riding on such a vehicle are of mixed gender and age and it is furthermore assumed that these are unadapted to motion sickness as extended exposition to a mode of transport and its inherent motion will create an immunization effect [21].

To summarize, it is assumed that the trajectory of a UAM will take 10 to 30 minutes flight time with a multitude of horizontal bank-to-turn maneuvers except for the approach and landing phase as well as start and climb-out which are vertical maneuvers.

1.4.2 Conventional Helicopters

The trajectory of conventional helicopters on the other hand, differs significantly based on what type of mission is required. While VIP transport or medical air services require a smooth ride, military applications might need highly dynamic nap-of-the-earth trajectories. The same goes for duration of these flights: While some missions only last a couple of minutes, others might take more then two hours. The usage of conventional helicopters is simply too divers in order to conclude general remarks. It is up to the designer of the specific flight control system to foresee how that system can best be utilized. For the following text we assume out of simplicity that the same mission requirements of those formulated for UAM vehicles also apply to conventional helicopters.

1.5 Scientific Question

This thesis aims to make a contribution to minimizing motion sickness during aerial transport with a special focus on vertical lift. The design and development of modern flight control systems shall be facilitated by delivering research results and tools aimed at quantifying the impact of various control systems on the motion sickness of pilots and passengers. Such tools are envisioned to be especially helpful for the future design or improvement of existing designs in the UAM sector. Moreover, traditional helicopter flight control designs can also benefit, as improved ride comfort typically decreases the fatigue of pilots and therefore leads to higher mission effectiveness.

As a first step, UAM and traditional helicopter trajectories and motions were defined, which serve as a basis for determining the research question of this thesis. Based on this and the general introduction, the overarching scientific question is formulated as follows:

How can the effect of motion sickness of pilots and passengers be quantified and predicted for the design of rotorcraft?

The question is further subdivided to highlight specific aspects: First and foremost, motion sickness shall be mathematically modeled in order to be able to quantify trajectories or movements of a rotorcraft in respect to their effect on motion sickness. The first question is therefore how such a model can be determined.

1. **How can motion sickness be mathematically modeled and simulated as a function of a given trajectory or motion?**

After an appropriate model has been specified, it has to be validated to show that it indeed gives accurate predictions of motion sickness, resulting in the following questions:

2. **How can the developed motion sickness model be validated?**

    a) **Are motion simulators a viable option for validating the motion sickness model?**

    b) **How can a corresponding study be implemented from a technical standpoint?**

c) **How does the prediction quality of the motion sickness model compare to its validation?**

As a last step and outlook, the work shall clarify how the developed and validated model and the knowledge gained from this process can be leveraged for the design of a flight control system.

3. **How can such a motion sickness prediction model be deployed and used for the development of more comfortable flight control systems?**

1.6 Thesis Structure

Based on the scientific question, the following work is structured in four main parts:

1. Determination of a motion sickness model
2. Execution of flight tests and flight test methodology
3. Comparison of predicted and experimentally determined motion sickness of the flight tests
4. Conclusion and answer to the scientific question

Chapter 2 starts with an exact definition of the assumed trajectory. Furthermore, current motion sickness metrics are introduced and evaluated for usage as motion sickness prediction models for the proposed application and the intended application as stated at the beginning of Chapter 2. The direct modeling of the motion conflict responsible for motion sickness is then evaluated and further refined by tuning the parameters of that simulation model with the help of published data.

In Chapter 3, the realized flight tests are introduced together with the technical systems which had to be developed in support of these flight tests. This includes the description of the general methodology of the survey, the development of suitable questionnaires, the development of a suitable flight path reconstruction filter and the development of a suitable auditive cueing system. All of these techniques or systems are crucial in one way or another for the successful completing of the flight tests.

Chapter 4 compares the results of the predicted motion sickness model of Chapter 2 and the flight tests of Chapter 3. For this a statistical analysis is performed.

As a last step the work is summarized and concluded in Chapter 5, furthermore answering the scientific question posed in Chapter 1 and summarizing the scientific contributions.

2 Motion Sickness Metrics

As stated, the goal of this thesis is to deliver tools in order to design a *comfortable* AFCS, that is an Automatic Flight Control System which minimizes motion sickness. A first step in this process is to enable the design engineer to assess a given design proposal regarding how strongly it provokes motion sickness. Only with the insights of such a first step, the design can be improved or adapted in order to comply better with a given design goal. Therefore a metric of motion sickness is needed, or in other words, a motion sickness model.
A good motion sickness metric or model should be able to judge a given motion in respect to its provocation of motion sickness. Typically, such a motion would originate from either suitable simulation data or real flight data in a time-index manner. Ideally it should also be able to correlate specific portions of such data to it nausogenicity for easy identification of critical maneuvers or flight portions. Last but not least such a metric should entail as broad of a motion spectrum as possible. Furthermore, it should be noted that not every motion has to be quantified in this regard. In some cases such as aerobatic or emergency maneuvers, the judgment of comfort is not relevant for obvious reasons.

2.1 Legacy Motion Sickness Models

As pointed out in the introduction, motion sickness is a common problem for a variety of transports. Equally, a lot of research exists to predict motion sickness. The following section will discuss several established metrics for estimating the extent of motion sickness in respect to a given motion based on a short literature review.

2.1.1 ISO 2631-1

The international norm ISO 2631-1:1997-05: "Mechanical vibration and shock - Evaluation of human exposure to whole-body vibration - Part 1: General requirement" [16] is

(at the time of writing) the current norm for measuring and quantifying vibrations and their effect on the human body. This norm consists of two parts, whereby the second part deals with vibrations in buildings. For this reason only part 1 is considered in the following. It arguably represents the most used document of this type and is widely adopted not only in industry but also in science. It was first published in 1985 and has been updated several times, the last time in 1997.
The primary purpose of the ISO 2631-1 is stated to be [16]:

- Human health and comfort
- The probability of vibration perception
- The incidence of motion sickness

It furthermore subcategorizes vibration into two vibrational ranges depending on the frequency:

- $0.1\,\mathrm{Hz}$ - $0.5\,\mathrm{Hz}$: Motion sickness
- $0.5\,\mathrm{Hz}$ - $80\,\mathrm{Hz}$: Health, comfort and perception

The ISO 2631-1 also defines how to measure vibration data by defining sensor location, sensor direction, time of measurement and pose of the human body. It should be noted that the ISO 2631-1 specifies that the "primary quantity of vibration magnitude shall be acceleration", therefore "vibration data" in the context of the ISO 2631-1 is used synonymously with "vibration acceleration" with one exception in which rotational vibration is used.
Generally speaking, this norm quantifies the impact of vibrations upon the human body by filtering the acceleration via one of several frequency weighting curves which are selected according to the different axes of vibration, the pick-up location of the accelerometer and also the intended analysis application. The norm then specifies guidelines on how to use the filtered data by providing exact evaluation methods and also upper bounds for certain vibrational scenarios.

2.1.1.1 Shortcomings in Respect to Motion Sickness

The ISO 2631-1 also includes a guide on how to evaluate low-frequency vibration in respect to motion sickness. For this it specifies the calculation of the so-called Motion Sickness Dose Value

$$MSDV_z = \sqrt{\int_0^T a_{z,w}(t)^2 dt} \tag{2.3}$$

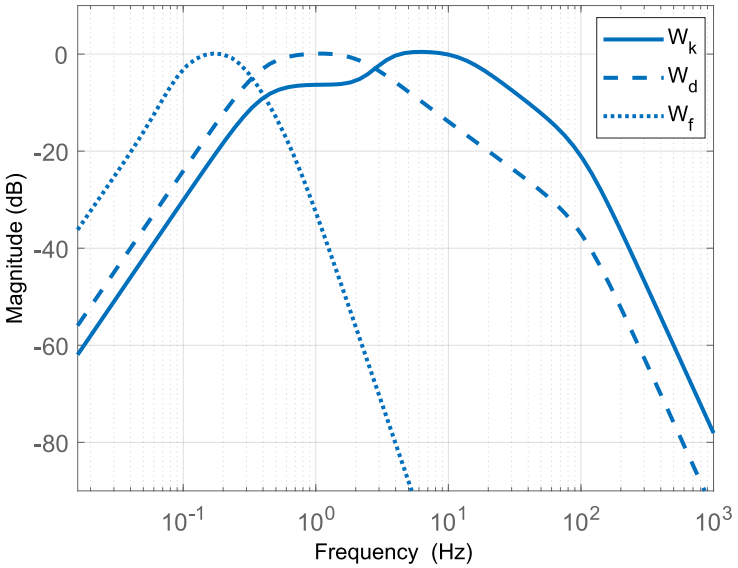

Figure 2.1: Examples of ISO 2631-1 frequency weighting curves

with T being the total time of exposure in seconds, and $a_{z,w}$ being the frequency weighted vertical acceleration (therefore the index z) signal in m/s^2. In case of the MSDV, the frequency weighting which shall be applied is the W_f filter, which is also depicted in figure 2.1. Several methods of applying this filter to the acceleration signal are specified, however probably the most convenient is the direct application of a digital filter transfer function to the vertical acceleration by means of numerical simulation. The exact definition of the ISO 2631-1 W_F filter is given in Appendix A.

After the frequency weighted acceleration signal $a_{z,w}$ has been computed, the motion sickness dose value $MDSV_z$ defined in equation 2.3 can be calculated. Given this value, the percentage of people vomiting can be estimated by multiplying the $MSDV_z$ with a factor of $1/3$ which yields the Motion Sickness Incidence (MSI) as introduced by O'Hanlon [31]. The ISO 2631-1 notes that this factor is determined for unadapted equally mixed male and female population.

In chapter 1.4 it was determined that expected trajectories and motions of the vehicles mainly consist of bank-to-turn maneuvers which are characterized by rolling into a curve followed by a slight increase in the vertical acceleration. It therefore becomes immediately obvious that the ISO 2631-1 is not well suited for the evaluation of such maneuvers, as it does not consider the rotational motion associated with banking turns. This analysis is validated by a study from M. Turner et. al. [32] in which only linear acceleration data was measured, but no clear correlation between these linear accelerations and motion sickness (airsickness) could be determined. Griffin [19, p. 317-318] on the other hand notes that rotational motions of an aircraft are less likely to affect motion sickness, but also notes that it should not be expected that acceleration in the z-axis alone will accurately predict motion sickness.

While it is unclear which method is best suited for predicting motion sickness, the author of this thesis draws the conclusion that the ISO 2631-1 is not ideal for predicting motion sickness for complex movement scenarios as those encountered in aerial vehicles. This is mainly due to the focus on vertical acceleration, while aerial vehicles also exhibit lateral and longitudinal acceleration as well as rotatory movement.

2.1.2 ADS-27 A

Traditionally, other models to judge the effect of vibration on human crew have been developed. Probably the two best known are the ADS-27A [33] which is a standard defining requirements for vibration and equipment installed of rotorcraft vehicles as well as the NASA Ride Quality Index.
The ADS-27A standard defines that "The total vibratory environment of the rotorcraft shall be such that compatibility between the airframe, engines, subsystems, and installed equipment is achieved and the ability of the rotorcraft, its crew, and any passengers or troops to perform the required missions is not compromised" [33]. It should be noted that such a definition is somewhat broader then discomfort. A vibration is only then considered to be unacceptable if it interferes with the "ability" of the crew to not perform its task. The assessment of the helicopter vibration is performed via the so-called Intrusion Index which "includes the effects of all frequencies below $60\,\mathrm{Hz}$". In order to calculate this index, first the measured vibrations shall be normalized (weighted) according to defined frequency normalization (weighting) curves, then "The four largest peaks, excluding the one-per-revolution peak, for each of the three normalized spectra shall be identified [...]" [33]. The Intrusion Index is then calculated by drawing the square root of the sum of square of these twelve values. Two facts are noteworthy in this context:

1. The vibrations which are to be measured are defined as a velocity "ips" (inch per second), and not as an acceleration

2. The lowest considered vibration is $5\,\mathrm{Hz}$, below this frequency the frequency normalization (weighting) curves are not defined.

2.1.3 NASA Ride Quality Index

In contrast the NASA Ride Quality Index focused on quantifying ride comfort inside a typical, modern[1] jet-liner type cabin. For this, 2200 test subjects were seated on a three-degree-of-freedom motion simulator with the seating configuration of a contemporary jet-liner. Various frequencies for sinusoidal and random vibrations were tested depending on the axis involved, and ranged from 1 to $30\,\mathrm{Hz}$ whereby the test subjects were simultaneously exposed to noise played over speakers. The model distinguished between single axis discomfort and combined axis discomfort. Both metrics are then united into a singular discomfort model [34].

2.1.4 Conclusion on Motion Sickness in Norms

While the NASA RQ model does not explicitly state frequency weighting curves, Rath et al. [14] showed that frequency weighting curves are implicitly defined over frequency-dependent coefficients of the assessment of sinusoidal and random vibrations. Furthermore, the authors compared the different comfort criteria and found that the ISO 2631-1, the ADS 27 and the Nasa RQ index showed very comparable predictions in the sense that the explicit and implicit frequency weighting curves of all three standards are very similar. It was also found that the ISO 2631-1 is the most universal of the three standards, as its definition spans over the widest frequency range. Additionally, it also offered better and broader definitions of sensor locations. This leaves the conclusion that the ISO 2631-1 standard sufficiently entails the ADS-27 as well as the NASA RQ index for the evaluation of ride comfort. However, it should be noted that the ride quality does not entail motion sickness. The ISO 2631-1 does define ride quality in three vibrational axes with several sensor locations (feet, seat, backrest). However, as pointed out earlier, the metric for motion sickness does not entail more than the vertical axis, which emphasizes the need for a better metric containing effects in more then one axis. A couple of conclusions from this short literature review on ride quality metrics can be drawn. First of all Rath et al. noted that while the authors of the NASA RQ index differentiated between sinusoidal and random vibrations, the tests performed for that index showed similar sensitivity for sinusoidal and random vibrations. This is an import note for the later applicability of models which have been identified for sinusoidal vibrations and shall be applied to more complex scenarios. Furthermore, Rath et al. noted that only the ISO 2631-1 extended to frequencies lower than $1\,\mathrm{Hz}$. However, as noted in the

[1] for the time, the paper was written in the 1980s

introduction and figure 1.3, frequencies below $1\,\mathrm{Hz}$ are also an important factor in the overall vibration exposure of pilot and crew [14].
All in all we can conclude that available norms suffer from two main shortcomings, primarily in respect to quantification of motion sickness:

1. Definition/model does not contain low enough frequencies for motion sickness

2. Definition/model does not contain information about more then one motion axis or coupled axis motions

2.1.5 Railway Research on Motion Sickness

These shortcomings were also identified by the railway community, which investigated motion sickness in regards to typical motions of tilting trains. One especially noteworthy contribution was performed by Donohew et al. [35] who, based on motion sickness experiments, synthesized a new frequency weighting curve for lateral oscillation. For this, data from a motion simulator capable of moving along a $12\,\mathrm{m}$ track while simultaneously tilting around one axis (roll or pitch) was used. This motion simulator is displayed in figure 2.2. Each test subject was exposed to 30 minutes of continuous lateral oscillation at one of several candidate frequencies while self-rating their motion sickness level every minute on a scale from 0 to 6: (0: No symptoms; 1: Any symptoms, however slight; 2: Mild symptoms, e.g., stomach awareness but not nausea; 3: Mild nausea; 4: Mild to moderate nausea; 5: Moderate nausea but can continue; 6: Moderate nausea and want to stop). This experiment will be further discussed in Section 2.3.1. Together with results obtained from previous similar experiments conducted by the same research group, Donohew et al. could define a new frequency weighting curve parametrized in the same manner as those of the ISO 2631-1 as described in appendix A. This frequency curve was however defined with data of motion sickness level 3 (Mild nausea) as this rating offered the best compromise between specificity and sensitivity. Past experiments [37] suggested an approximately linear dependency of motion sickness upon the acceleration amplitude, however motion simulators cannot offer constant acceleration excitation over all frequencies as the available velocity and displacement limits of the motion simulator are constraining the maximum acceleration. This relationship can be easily seen when looking at a sinusoidal vibration defined

Figure 2.2: The $12\,\mathrm{m}$ Tilting and Translating Cabin motion simulator of the Institute of Vibration at the University of Southampton. Taken from [36]

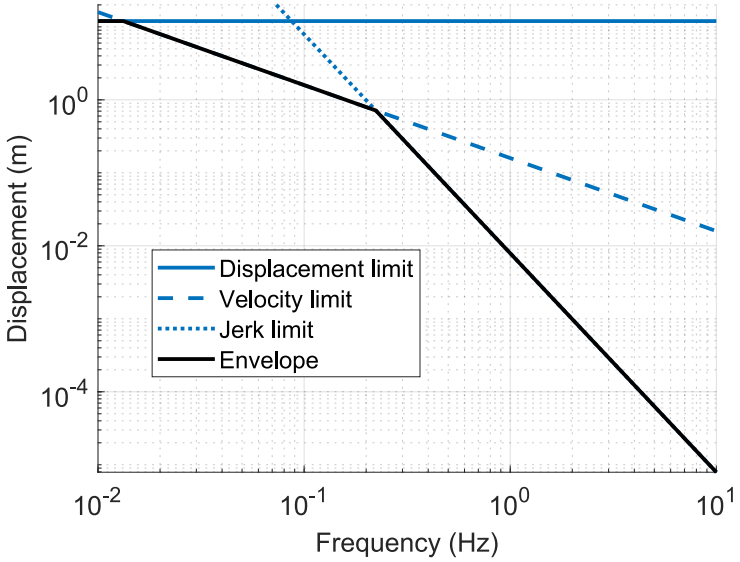

Figure 2.3: The motion range limits of the University of Southampton's $12\,\mathrm{m}$ Tilting and Translating Cabin

by its displacement amplitude A_{dis} at a fixed frequency and its derivatives:

$$x = A_{dis} \cdot \sin(\omega t) \tag{2.4}$$

$$\dot{x} = A_{dis} \cdot \omega \cos(\omega t) \tag{2.5}$$

$$\ddot{x} = -A_{dis} \cdot \omega^2 \sin(\omega t) \tag{2.6}$$

Combining this with the limits of Southampton's motion simulator (Fig. 2.2) taken from [35], this point can be further visualized in a logarithmic plot as shown in figure 2.3 for this specific simulator. Therefore, Donohew et al. normalized the motion sickness incidence ration with the RMS value of acceleration at each frequency in order to obtain datapoints for lateral vibration without simultaneous tilting. The resulting frequency weighting is depicted in figure 2.4. This research is interesting for a couple of reasons:

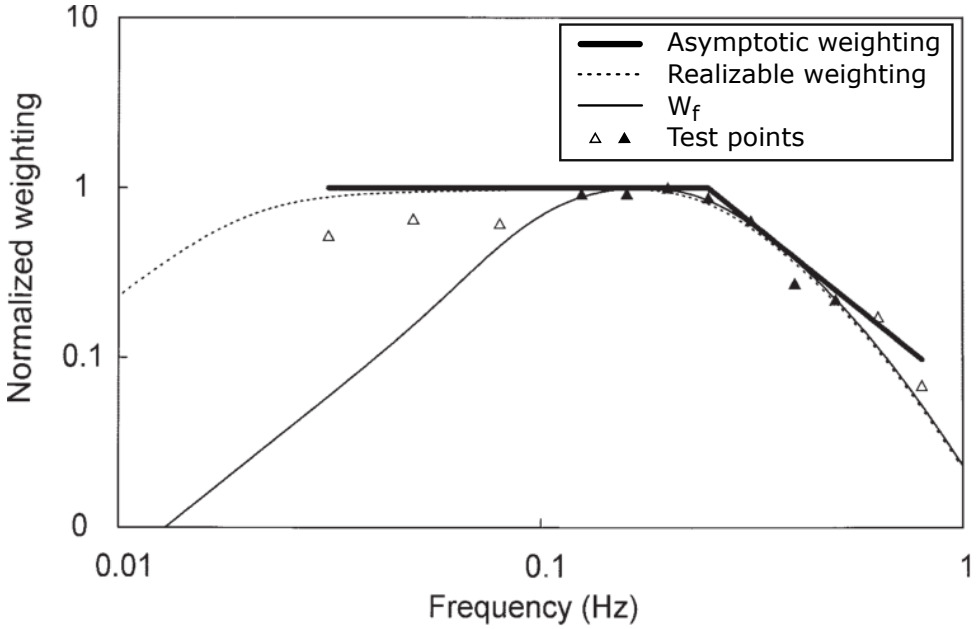

Figure 2.4: Frequency weighting for motion sickness of lateral oscillation, taken from [35] with addition of a legend

- It shows how empirical data can be used for defining new frequency weightings.
- For the definition of its frequency weighting, it uses motion sickness level 3. This is interesting, as such a definition offers more nuanced differentiation compared to the ISO 2631-1 standard which only offers the Motion Sickness Incidence (MSI) rating as a percentage of people getting motion sick.
- However, such research only offers an additional frequency weighting for lateral oscillation, a combination of several axis is not defined.

The same research group has published numerous papers on experiments with additional motion parameters which combine lateral with roll oscillation in varying setups including varying amplitude, compensation relations, phase relationships, center of rotation offset etc. [25, 38–43]. However, this work never culminated in any other metric or frequency weighting curve.

2.1.6 Conclusion on Norms and Available Literature

From this analysis of current literature and norms, two main points can be concluded:

1. There is no established standard judging motion sickness in the generality as is needed for vertical lift application

2. Experimental data sources on motion sickness are available and can be used for the definition of either frequency weightings or other means of building motion sickness models

Specifically the various research topics of tilting railway research should not be left out if one is considering motion sickness during flight. While vertical lift vehicles or aircraft do not seem to have much in common with railway vehicles, it can be concluded that large portions of the movement characteristics of the two classes of vehicles are very similar. In chapter 1.4 it was identified that the vertical lift vehicles considered in this thesis perform mostly flat maneuvering, while vertical flight segments such as take-off and landing are very short compared to the length of the entire flight. Of course tilting railway vehicles do not have a starting or landing phase however while traveling, the movement also consists of horizontal turns with a simultaneous tilting action. The specifics of the two vehicles classes may vary, especially the amplitude or vibration spectrum might not be immediately comparable, however the research performed for either can be more comparable then is intuitively expected. This makes it clear that the aforementioned papers do have a high relevance for the construction of motion sickness models for aeronautical applications. However, it is also true that this work did not culminate in an applicable standard or metric which can be either readily applied or transformed to fit for the application in question. It seems that most train manufacturers deem the problem of motion sickness to be sufficiently solved by either relying on one of the empirical tunings as presented in chapter 1.3.2 or tuning the controller responsible for tilting the railway carbody with trial runs during initial tests of new trains.

2.2 Direct Modeling of Motion Conflict

In contrast to the classical method of fitting mathematical functions to experimental data as performed for the ISO-2631-1, another approach of modeling motion sickness is the attempt to directly model the human motion sickness mechanism. As detailed in chapter 1.3.1 the prevalent theory for motion sickness states that motion sickness arises whenever a motion sensation as perceived by the vestibular system differs from the motion sensation as perceived by the eye from expected or learned motion sensation. The direct modeling of this motion conflict is the attempt to use continuous modeling techniques in order to retrace the underlying principle of the conflict theory. Numerically simulated, such a model can be very useful in order to predict motion sickness given a motion trajectory, for example in order to design or verify an AFCS design. The

benefit of this approach is that the structure of the underlying model helps in addressing particular properties of the results. Furthermore, multi-axis inputs in acceleration and rotatory velocities can be seamlessly integrated in such modeling. However, it is intuitively clear that intimate knowledge of the motion sickness mechanism is needed for an accurate model. This is a difficult task, as the mechanism has to be identified from appropriate tests using human test subjects. The design of these experiments is by no means trivial and the corresponding modeling naturally underlies a great variability. The solution space of this modeling problem is relatively large and therefore no singular solution can be confidently called correct. Nevertheless, this problem was tackled by several researchers as can be seen in the following.

2.2.1 Model by Bos and Bles

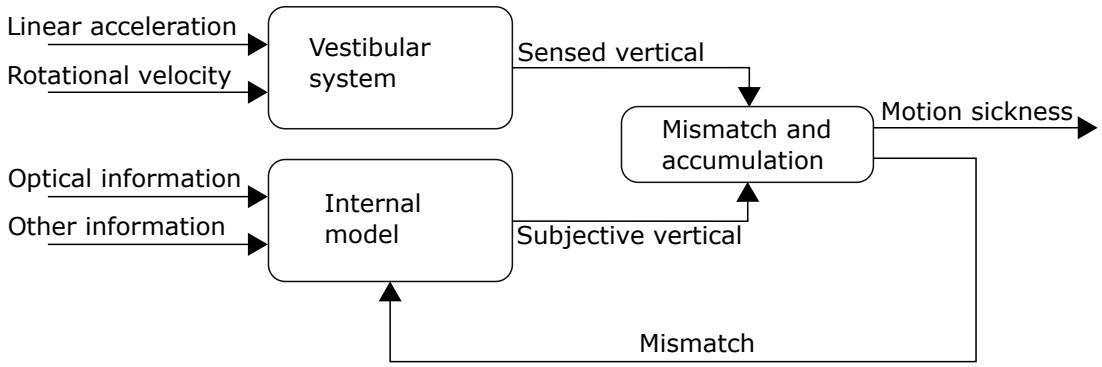

Figure 2.5: Sketch of the information flow regarding the conflict theory modeling as proposed by Bos and Bles [20]

To the best knowledge of the author of this thesis, this approach was first suggested by Bos and Bles [20]. A sketch of the information flow is displayed in Fig. 2.5. Hereby the conflict theory is modeled by constructing the vector difference between a *sensed vertical* and *subjective vertical*. Both vectors represent the vertical axis, however once as a result of the sensory information, which means as a result of both the otolithic organ sensing the acceleration as well as the semicircular canals sensing rotational speed and once based on the internal model which uses optical information combined with past experience. This *conflict* is then fed through an appropriate nonlinear conflict transfer function followed by an *accumulation function* in order to accumulate the stimuli to a measure of motion sickness.

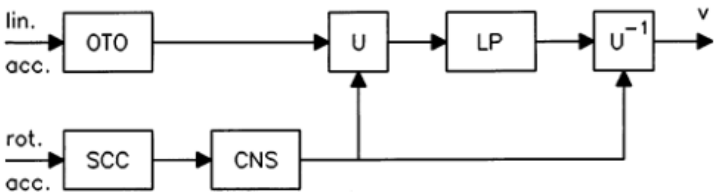

Figure 2.6: The determination of the sensed vertical taken from [20]

2.2.1.1 Sensed vertical

For the *sensed vertical* system as shown in Fig. 2.6, the authors suggest a system in which the linear accelerations sensed by the otolithic organ (marked as "*OTO*" in Fig. 2.6) are rotated with the help of the rotational speeds as sensed by the semicircular canals (*SCC*), in order to obtain a vertical acceleration vector. That information is additionally processed by the Central Nervous System ("*CNS*"). The block determining the rotation is marked as U. This vector is then low-pass filtered ("*LP*") before being transformed back ("U^{-1}") to a "head-fixed" coordinate system which then represents the *sensed vertical* v. The low-pass filtering of the "earth-fixed" acceleration vector is performed in order to filter out accelerations from head-movement, which are argued to have a relatively short time constant compared to other accelerations.

2.2.1.2 Subjective vertical

The authors speculate on the presence of a internal estimation algorithm, which uses visual information, motor commands etc. in order to form an internal *subjective vertical*. It is also speculated that techniques similar to optimal control strategies are applied to estimate the subjective as fast and efficient as possible under all circumstances. In order to keep things simple however, the same transfer functions as used for the *sensed vertical* is used. The time-constant of the low-pass filter is adjusted to adhere to experimental results with human test subjects.

2.2.1.3 Conflict and Accumulation

The conflict between the *subjective vertical* as well as the *sensed vertical* is calculated as a vector sum in order to catch differences in magnitude as well as direction. The conflict is also fed back into the *subjective vertical* as the brain naturally tries to eliminate this conflict. The conflict itself is first fed through a nonlinear transfer function which serves

the purpose of scaling the conflict between 0 and 1 such that the maximum motion sickness value is reached asymptotically while small conflicts are transmitted exponentially. For this task, the authors chose a Hill-function as described by the following equation:

$$h = \frac{(c/b)^n}{1 + (c/b)^n} \tag{2.7}$$

with c being the conflict (or input to the function), h representing the resulting conflict and b and n being parameters which in this specific case were chosen as $b = 0.7$ and $n = 2$.
As a last step the afore calculated value h is accumulated inside a leaky integrator described by the following equation:

$$MSI = \frac{P}{(\mu s + 1)^2} \cdot h \tag{2.8}$$

With P representing the maximum value, and μ being the time constant. This leaky integrator shall model that fact that the Motion Sickness Incidence (MSI) value cannot exceed 100% as well as the fact that if the stimulus ceases, the MSI value returns to zero asymptotically.
Bos and Bles then used a simplified model neglecting rotational stimulus which was fed with vertical sinusoidal accelerations of varying frequency and peak accelerations. The authors showed that the qualitative results of this model closely resembled those of empirical results found by McCauley et al. [37] on motion sickness in response to vertical oscillation. These encouraging results show that the proposed modeling approach is capable of predicting motion sickness given appropriate motion information.

However while the paper proposes ideas for incorporating rotational stimuli, it does not specify a model for incorporating these information. This leaves the interested reader with the following conclusion: While this research offers very interesting insights particularly in potential modeling techniques of motion sickness, the presented simplified model does not solve the downsides of the existing ISO 2631-1, namely that only one axis is considered.

2.2.2 Model by Kamiji et al.

Building upon the model by Bos and Bles [20], the authors Kamiji N., Yoshinoria K., Wada T. and Shun'ichi D. proposed an improvement and extension of the proposed model to three degrees in freedom in acceleration as well as rotation [44]. This work focused specifically on carsickness and the rotation of the head while riding automotive

vehicles, however the general idea of this model is very similar to that of Bos and Bles, albeit with special incorporation of the rotational stimulus of the semicircular canals. The complete model as proposed by Kamiji et al. is displayed in 2.7. Note that the input to the model, the acceleration a and the rotational velocity ω are 3-dimensional, time-based vector quantities. The model is again split up into two systems: On the one hand the "real" or "physical" model, meaning the model of the physical sensory organs and interconnections consisting of the otolithic organ (OTO) as well as the semicircular canals (SCC) and the corresponding interconnection of the gravity vector component (G) acting upon the otolithic organ. The block G is inserted because the otolithic system cannot differentiate between the acceleration due to inertial effects and gravity, therefore the force on the otoliths becomes $f = a + g$. Additionally, the estimated rotational rate $\hat{\omega}$ acts on the low-pass filter (LP) to form the subjective vertical, as described above. On the other hand, the "internal" model represents the same values as estimated internally by the brain based on *visual* input, therefore *not* using the otolithic organs or semicircular canals. In order to differentiate the "internal" from the "physical" model, the corresponding blocks of the "internal" model are marked with a bar over the name (e.g. $\overline{SCC}$). Quantities which are estimated by the "internal" or "physical" model are marked with a hat over the signal (e.g. $\hat{\omega}$), while quantities of the "internal" model are denoted with a tilde sign (e.g. $\tilde{\omega}$) or a combination of the two, if it is an estimated "internal" quantity (e.g. $\hat{\tilde{\omega}}$). The signals Δa, $\Delta\omega$ and Δv represent the errors between the "internal" and "physical" in acceleration, rotational rate and subjective vertical respectively. Analogously to the model by Bos and Bles, these are integrated and added to the respective quantities of the internal model in order to establish a feedback loop.
The generation of the motion sickness conflicts as well as the accumulation function is very similar to the model by Bos and Bles, but acting in three dimensions. The gains K_a and K_ω represent the limited ability of the visual system to accurately measure the angular velocity and translational acceleration. Some of the dynamic blocks are defined as simple passthrough blocks, therefore containing no dynamic components. For the sake

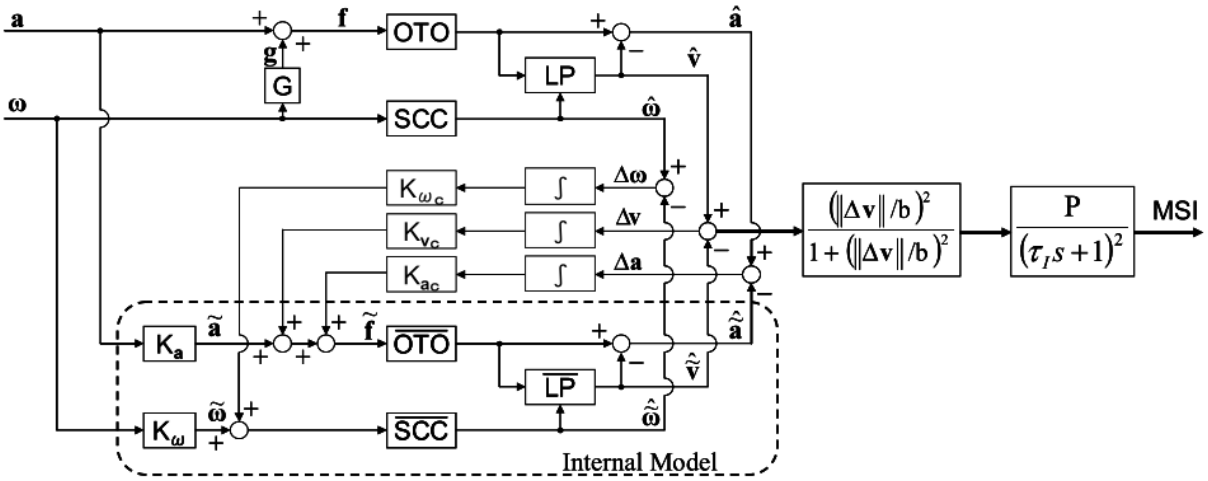

Figure 2.7: The complete model as proposed by Kamiji et al., taken from [44]

of completeness the transfer functions of all blocks are listed in Eqs. (2.9) to (2.15).

$$OTO : \hat{f} = f \tag{2.9}$$

$$SCC : \hat{\omega} = \frac{\tau_d \tau_a s^2}{(\tau_d s + 1)(\tau_a s + 1)} \cdot \omega \tag{2.10}$$

$$LP : \frac{d\hat{v}}{dt} = \frac{1}{\tau}(\hat{f} - \hat{v}) - \hat{\omega} \times \hat{v} \tag{2.11}$$

$$G : \frac{dg}{dt} = -\omega \times g \tag{2.12}$$

$$\overline{OTO} : \hat{\tilde{f}} = \tilde{f} \tag{2.13}$$

$$\overline{SCC} : \hat{\tilde{\omega}} = \frac{\tau_d s}{\tau_d s + 1}\tilde{\omega} \tag{2.14}$$

$$\overline{LP} : \frac{d\hat{\tilde{v}}}{dt} = \frac{1}{\tau}(\hat{\tilde{f}} - \hat{\tilde{v}}) - \hat{\tilde{\omega}} \times \hat{\tilde{v}} \tag{2.15}$$

For completeness, the accumulation function processing the mismatch Δv is given by

$$h = \frac{(\|\Delta v\|_2 / b)^n}{1 + (\|\Delta v\|_2 / b)^n} \tag{2.16}$$

with $n = 2$ and $b = 0.5$.

2.2.2.1 Shortcomings

Kamiji et al. tested their proposed model on several cases taken from literature. These included the case of lateral oscillations and the proposed lateral frequency weighting curves [35] which was also discussed in chapter 2.1.5. It was then proposed to manually tune the model in order to achieve better performance. The authors argue that a mathematical analysis of the model is hardly possible but propose building intuition via

empirical tuning. Such an approach is of course highly subjective and, depending on how thorough the process is carried out, also not trivial. Another critique point is the limited validation set for which the tuning process is carried out. As described before, only limited models on motion sickness are available, especially models combining rotational and translational movements are very sparse or not present at all. Therefore only limited insight can be gained from the direct comparison of the Kamiji model against other models as these only offer very limited scopes. Most import of all is that the model, while exhibiting good tracking of the general shape of the data, does not agree well in quantitative tracking. This will be shown in Section 2.3.4.

Additionally, it should be noted that the motion sickness conflict generated by the Kamiji model is heavily dependent on the structure and type of transfer functions used by the model. For example Kamiji et al. decided to use simple gains in order to represent the ability of the eye to track movements. Bos and Bles speculated that some kind of optimal control strategy is used for this task [20]. Which model represents the inner working of how the brain estimates movement given visual information more accurately is unknown. Additionally, determining the exact mechanism is a difficult problem, as it is not trivial to design a suitable experiment to determine this relation. The same goes for a lot of other assumptions and specifically transfer functions used inside the Kamiji model. However, the results of this model are quite promising, because they match the experimental results quite well qualitatively. To sum up, the following conclusions of the Kamiji model can stated:

- It offers a convenient way to include 6-DoF movement data
- It uses time-referenced data
- It is straight-forward and easy to implement
- It directly outputs motion sickness incidence (MSI) data
- The results of the model mirror motion sickness data qualitatively
- It is unkown if the Kamiji model mirrors the structure of the human motion sickness mechanism
- The model has to be improved if it shall be used in order to accurately predict motion sickness

2.3 Improving the Kamiji Model

As will be shown in Section 2.3.4, the Kamiji model is not able to predict simulator experiments accurately. For this reason, the Kamiji model will be improved via a two-fold strategy. First the model will be slightly adapted in order to improve its capability to predict motion sickness. In a second step, the various inherent parameters in this model will be tuned with the help of numeric optimization techniques with data taken from a suitable, experimental dataset on motion sickness. Both processes will be described in the following.

This approach and large parts of the following results were first published by the author in [45, 46] and are taken from these publications.

2.3.1 Griffin Paper Dataset

Before the work on the model and the subsequent optimization can begin, a suitable database which can serve as a basis for the optimization process has to be found. The requirements for such a dataset are as follows:

- Shall be experimental data on motion sickness
- Obtained with the use of a suitable motion simulator or on a suitable vehicle
- Sufficient number of test subjects/participants
- Consistent and well-documented test setup
- Motion profile is well documented (frequency, amplitude, etc.) and repeatable
- Motion sickness of test subjects/participants recorded throughout the test

Due to the extensive effort, time, cost and know-how involved in designing and conducting experimental tests on motion sickness which satisfy such requirements, it was decided to use already existing data from literature. The Griffin paper dataset which will be presented in the following, was identified to satisfy the requirements above and will be used in the following for the optimization process.
Under the guidance of Professor Griffin, the PhD[2] candidates Donohew, Josephs and

[2] at the time

Table 2.1: Motion sickness scale used by Griffin et al.

0	No Symptoms
1	Any symptoms, however slight
2	Mild symptoms
3	Mild nausea
4	Mild to moderate nausea
5	Moderate nausea but can continue
6	Moderate nausea and want to stop

Beard published a total of seven different papers [25, 35, 39–43] which contained empirical data and analysis of motion sickness experiments with humans, in order to better understand the effects of different motion forms on motion sickness. Because of the trajectory and motion assumptions described in chapter 1.4 only papers considering *lateral* oscillations with and without simultaneous tilting or rolling of the cabin were considered for the selection of these papers. Additionally, the paper [42] was excluded from the dataset because the test conditions were not consistent with the other papers while [43] focused on only roll and pitch oscillation without lateral oscillation which is also not suitable for this dataset.

The resulting dataset, which shall be referred to as "Griffin dataset" in the following, consists of the following five papers [25, 35, 39–41]. The approach was similar for all of these publications: One or several candidate motion forms were chosen and generated with the help of the $12\,\mathrm{m}$ Tilting and Translating Cabin setup of the Institute of Sound and Vibration Research, University of Southampton, as depicted earlier in Fig. 2.2. Because of the layout of the motion simulator, the test compromised either lateral or horizontal translational accelerations with or without simultaneous tilting or pitching of the cabin at different frequencies and different excitation amplitudes.

The frequencies of the generated motions ranged from $0.0315\,\mathrm{Hz}$ to $0.8\,\mathrm{Hz}$. Due to the harmonic nature of the oscillation, jerk, acceleration, velocity and displacement are physically linked. However, the limits of these values are naturally dictated by the limit of the motion generator. The limits of this particular $12\,\mathrm{m}$ Tilting and Translating Cabin are displayed in figure 2.3, tabulated in Eq. (2.17) and are taken from [39]. All tests were conducted with the simulator performing at its limits. For this reason, frequency is directly linked to maximal jerk, acceleration, velocity and displacement via the envelope bound of the simulator. The mathematical description of these envelope bound for a motion simulator are derived in 3.1.

The Griffin dataset consists of 560 subjects completing a total of $620\,\mathrm{hours}$ of testing inside the Southampton motion simulator. The setup of the different tests was remark-

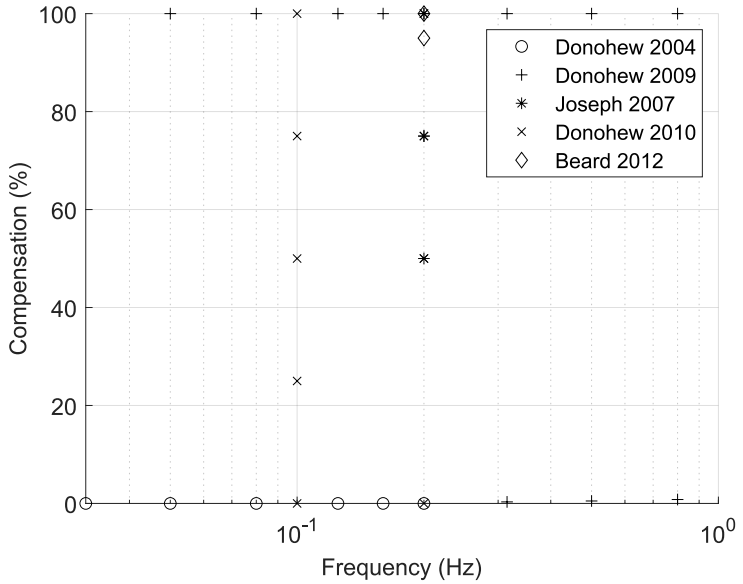

Figure 2.8: Motion parameter space covered during experiments performed in [25, 35, 39–41] for determining motion sickness. Each point was tested with 20 test subjects

ably similar over the various papers: each subject completed 30 minutes of exposure to one candidate motion, while rating the subjective motion sickness every minute on the Griffin motion sickness scale Table 2.1. During the tests, the subjects sat inside the cabin lit by a $40\,\mathrm{W}$ lightbulb with headphones emitting white noise. No visual contact to the outside was provided by the cabin.
In total 31 motion test points, each consisting of one sinusoidal lateral translation at different frequencies coupled with different degrees of compensation, were tested. Each testpoint and its capability of provoking motion sickness was tested on 20 subjects.

This data was extracted from the aforementioned papers, and compiled into a unified dataset in the MATLAB® programming language. An overview of the extracted testpoints plotted over frequencies and compensations is shown in figure 2.8. The interested reader might note that some test points coincide with each other. This stems from the fact that some points were tested several times across papers therefore appearing multiple times in the dataset.

$$D(f) = \begin{cases} 12 & f \leq 0.013\ \text{Hz} \\ 12 \cdot 2\pi f & 0.01328\ \text{Hz} < f < 0.223\ \text{Hz} \\ 12 \cdot 1.96 \cdot \frac{1}{2\pi f} & 0.223\ \text{Hz} \leq f \end{cases} \tag{2.17}$$

It should be noted that the rolling motion was parametrized by percentage compensation, which denotes to which degree the cabin was tilted in order to compensate for

lateral acceleration such that the acceleration felt by the subject would still be vertical. For example, a 100% compensation would mean that the cabin was tilted exactly so that the test subject does not feel any lateral acceleration, but only an oscillating, slightly higher vertical acceleration. In aerospace terms this would be the equivalent of a coordinated turn. On the other hand 0% compensation would mean that the cabin would be accelerated laterally without any tilting (rolling) of the cabin. Different compensation values were originally tested in order to emulate a railway vehicle "leaning" or "tilting" into a curve with various degrees as [24] empirically found that less then 100% compensation might lead to less motion sickness onboard such tilting trains. This relation can be mathematically expressed as

$$\varphi(t) = -\arctan\left(c \cdot \frac{a_y(t)}{g}\right) \tag{2.18}$$

whereby the tilt angle is denoted by φ, the earth acceleration by g, the lateral acceleration by a_y and the compensation c ranging from 0 to 1 which corresponds to 0% to 100%. The used coordinate system is shown in 2.9.

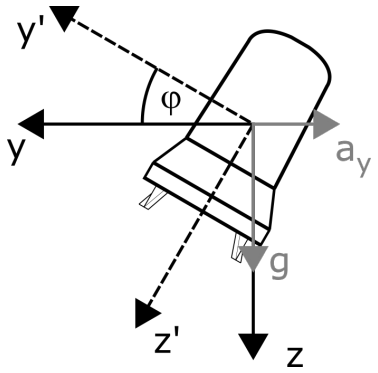

Figure 2.9: The coordinate system used for describing the lateral acceleration compensation

While this research was originally intended for general motion sickness research with a focus on railway applications, the Griffin dataset is afterall a good fit for the purpose of this study. It offers reliable high-quality data with a consistent experiment setup with a high number of test candidates. Especially this last point is not trivial to replicate, as the cost and effort of conducting $620\,\text{hours}$ of human trials should not be underestimated. Additionally, the data entails horizontal motions with combined roll motion closely mimicking coordinated turns in horizontal flight. The downside of this datset compared to a dedicated dataset tailored towards aerospace applications is the limited range of motion of the employed motion simulator as well as the fact that the test subjects had no external view during testing. Also this dataset does not include vertical oscillations which, although to a lesser degree then horizontal turns, still play a major

role in vertical lift applications. However, considering the extent of the data and the effort, cost and time it would take to produce a motion sickness dataset suitable for such a study, the Griffin dataset seems to be well enough suited for tuning a motion sickness model intended for vertical lift aerial transport applications under the assumptions formulated in chapter 1.4.

2.3.2 Kamiji Model Modifications

As a preliminary step for the subsequent optimization of the Kamiji model with the Griffin dataset, some modifications to the original model will be introduced in this chapter. The improved Kamiji model is depicted in figure 2.10. The added blocks are marked by a dashed outline. The main goal of the performed modification was to improve the optimization result and to adapt it to common aerospace standards. A list of modification is given in the following:

1. Introduction of low-pass filters: While the ISO 2631-1 details that frequencies provoking motion sickness lie in the range of $0.1\,\mathrm{Hz}$ to $0.5\,\mathrm{Hz}$ [16], this interval is extended in this work up to a frequency of $1\,\mathrm{Hz}$. However, during initial assessment, the Kamiji model showed insufficient roll-off at frequencies above $1\,\mathrm{Hz}$. In order to correct this behavior, a simple second order low-pass filter with a conservatively placed cut-off frequency of $4\,\mathrm{Hz}$ was introduced in the signal paths leading to the model. The transfer function for this filter is given in Gl. (2.19).

$$LP = \frac{1}{0.0638s^2 + 0.3573s + 1} \tag{2.19}$$

   These low-pass filters are marked as LP in figure 2.10.

2. Replacement of the “G” block: This block is intended to rotate the gravity vector into the head-frame. In order to assure congruence between the gravity vector and the external acceleration, this transformation is now explicitly stated as

$$\mathbf{g}_H = \mathbf{R}_{HI} \cdot \mathbf{g}_I \tag{2.20}$$

   with the subscript $_I$ denoting the inertial frame, the subscript $_H$ the head frame and $\mathbf{R}_{HI}$ the rotation matrix from the inertial to the head-frame.

3. Additional gain K_{out} at the MSI Output: Initial optimization results indicated that depending on the selected motion sickness rating defined by the Griffin paper set given in table 2.1, the predicted motion sickness level could not be matched. For this reason the gain K_{out} was introduced to the output of the improved Kamiji

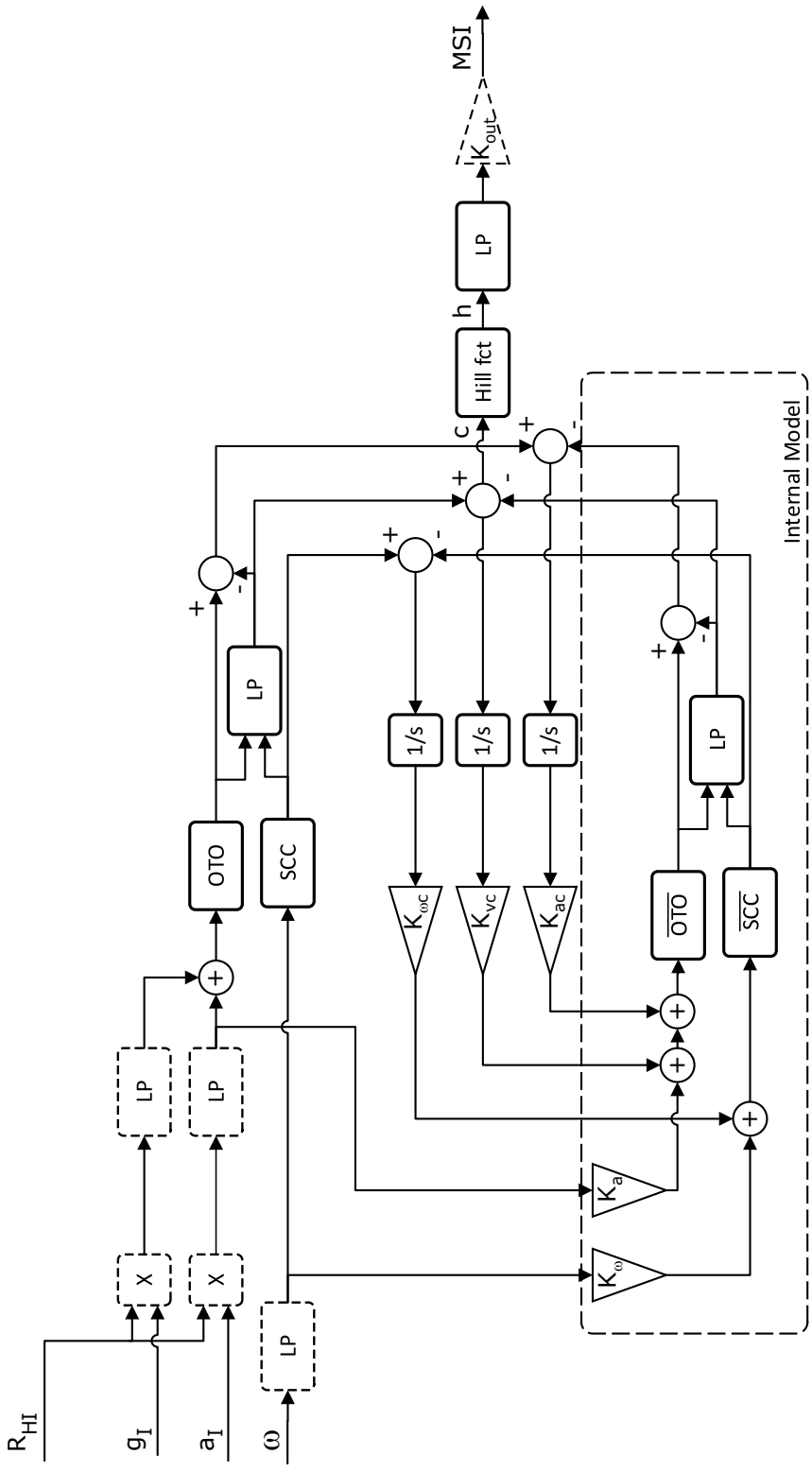

Figure 2.10: The block diagram of the improved Kamiji motion sickness model. Newly added blocks are marked with a dashed outline

model. This way, the optimizer can increase the models output magnitude for a given motion candidate. However, it is important to notice that one of the properties of the hill-function, namely that the output can never exceed 100%, is broken by this modification.

2.3.3 Optimization

The goal of the optimization is to determine an improved set of parameters for the Kamiji model, which, given the motions of the Griffin dataset, predicts the same motion sickness levels as observed in this dataset. In order to achieve this, a numerical optimization approach will be leveraged, which attempts to minimize the difference between the motion sickness level as predicted by the model and that of the Griffin dataset.

The task of the optimization problem is to find the optimal set of parameters $\mathbf{p}^*_{MSD}$ with which the results of the simulation $\mathbf{y}_{sim,MSD}(\mathbf{p}^*_{MSD})$ most closely match those of the Griffin dataset $\mathbf{y}_{Griffin}$ at a given motion sickness degree (MSD). The optimization problem is formally described as

$$\underset{\mathbf{p}_1 \cdots \mathbf{p}_6}{\text{minimize}} \quad \left\| \begin{pmatrix} \mathbf{y}_{sim,1}(\mathbf{p}_1) - \mathbf{y}_{Griffin,1} \\ \vdots \\ \mathbf{y}_{sim,6}(\mathbf{p}_6) - \mathbf{y}_{Griffin,6} \end{pmatrix} \right\|_2 \tag{2.21a}$$

$$\text{subject to} \quad \begin{aligned} &\mathbf{p}_1 \geq \mathbf{p}_{lb}, \\ &\quad \vdots \\ &\mathbf{p}_6 \geq \mathbf{p}_{lb}, \end{aligned} \tag{2.21b}$$

$$\begin{aligned} &\mathbf{p}_1 \leq \mathbf{p}_{ub}, \\ &\quad \vdots \\ &\mathbf{p}_6 \leq \mathbf{p}_{ub} \end{aligned} \tag{2.21c}$$

with $\mathbf{p}_{MSD}$ describing the various gains and block parameters of the improved Kamiji model as described in Eqs. (2.9) to (2.16). The vector $\mathbf{p}_{MSD}$ takes the form

$$\mathbf{p}_{MSD} = \begin{pmatrix} K_a & K_{ac} & K_\omega & K_{\omega c} & K_{vc} & \tau & \tau_a & \tau_d & K_{out} \end{pmatrix}^\mathsf{T} \tag{2.22}$$

with one set of model parameter $\mathbf{p}_{MSD}$ for each of the six models ($\mathbf{p}_1$, $\mathbf{p}_2$ etc.), whereby the subscript MSD indicates the motion sickness degree for which the specific parameter set is valid.
The vector $\mathbf{y}_{sim,MSD}(\mathbf{p}_{MSD})$ holds the predicted percentage of people reaching a certain motion sickness degree (indicated by the subscript MSD), for a given set of parameters $\mathbf{p}_{MSD}$ and for each simulated motion case. The vector $\mathbf{y}_{Griffin,MSD}$ holds the value for the same motion cases as recorded in the Griffin dataset. Different motion cases are structured as motion parameters which contain the frequency, percentage compensation, amplitude etc. in the vector vector $\mathbf{m}_i$. The Griffin dataset consists of 31 discrete sets of motion parameters, which are indicated by the subscript $_i$ with i denoting the i-th dataset. The vectors $\mathbf{y}_{sim,MSD}(\mathbf{p}_{MSD})$ and $\mathbf{p}_{MSD}$ for the 31 motion cases can therefore be expanded to

$$\begin{aligned}\mathbf{y}_{sim,MSD}(\mathbf{p}_{MSD}) = (\ & MSI_{sim}(\mathbf{p}_{MSD}, \mathbf{m}_1, t_{end}),\ MSI_{sim}(\mathbf{p}_{MSD}, \mathbf{m}_2, t_{end}),\ \dots \\ & ,\ MSI_{sim}(\mathbf{p}_{MSD}, \mathbf{m}_{31}, t_{end}))^\intercal\end{aligned} \tag{2.23}$$

$$\begin{aligned}\mathbf{y}_{Griffin,MSD} = (\ & MSI_{Griffin,MSD}(\mathbf{m}_1, t_{end}),\ MSI_{Griffin,MSD}(\mathbf{m}_2, t_{end}),\ \dots \\ & ,\ MSI_{Griffin,MSD}(\mathbf{m}_{31}, t_{end}))^\intercal\end{aligned} \tag{2.24}$$

with the subscripts $\dots_{Griffin,MSD}$ and $\dots_{sim,MSD}$ each denoting that the data stems from the Griffin dataset or from simulated data using the improved Kamiji simulation for a specific motion sickness degree (MSD). Note that the *final* motion sickness is compared, meaning that the percentage of people reaching a certain motion sickness value at the *end* of the experiment respectively simulation is compared, therefore after $30\,min$ of oscillation.

The cost function of Eq. (2.21a) is designed such that is minimizes the two-norm of a vector consisting of the differences between the improved Kamiji model ($\mathbf{y}_{sim,MSD}(.)$) and the experimental Griffin dataset ($\mathbf{y}_{Griffin,MSD}$) for each of the six MSD levels and additionally the weighted variances of the parameters of the improved Kamiji model. This leads to an optimization problem which determines the parameters of the six improved Kamiji models $\mathbf{p}_1$ to $\mathbf{p}_6$ in parallel, one parameter set for each motion sickness degree while preventing local minimas by penalizing too high differences between the parameter sets.
Variances between the different model parameters are normalized, weighted and minimized to prevent the optimization to find local minima. The argument of the variance is calculated as the fraction between the original Kamiji parameters (e.g. $K_{a,0}$) and the one found by the optimization (e.g. $K_{a,1}$, $K_{a,2}$ etc.). A weighting matrix **W** is introduced to enable the user to emphasize parameters in relation to one another and to the rest of the optimization function.

Table 2.2: The chosen upper and lower parameter vector bounds for $\mathbf{p}_1$ to $\mathbf{p}_6$.

	K_a	K_{ac}	K_ω	$K_{\omega c}$	K_{vc}	τ	τ_a	τ_d	K_{out}
ub	2	10	10	10	10	20	500	20	100
lb	0.01	0.1	0.1	0.1	0.1	0.1	1	0.1	0.5

For the sake of verification, implementation speed and traceability, the improved Kamiji model was first implemented using MATLAB/Simulink®. However, due to long invocation and compilation time of Simulink, the simulink model could not be used directly for the optimization. For this reason, the model was rewritten as an ODE executed by a suitable MATLAB® ODE solver in the MATLAB® programming language. The model was subsequently autocoded to a *.mex* file, which significantly decreased simulation and therefore overall execution time of the optimization.
The simulation model itself was setup such that it reflected the Griffin papers as detailed above, therefore the simulation time was set to $t_{end} = 30\,\mathrm{min}$, with the motion mirroring those of the specific motion candidate. For the optimization process, MATLAB®'s constrained nonlinear multivariable optimization function *lsqnonlin* was chosen.
The limits in Eqs. (2.21b) and (2.21c) have been chosen to roughly match the values as described by Bos and Bles [20] as well as Kamiji et al. [44] and to set reasonable bounds for the optimization algorithm without sacrificing too much of the design aspects of the original model. The chosen limits for the parameter vectors $\mathbf{p}_{MSD}$ are listed in Table 2.2. The results were achieved with a weighting function **W** with diagonal entries.
Initial optimization results indicated that the optimization tended to overamplify high frequencies. One of the root causes for this problem was identified as being the inherent coupling of the frequency with the acceleration amplitude of the Griffin dataset. The limits of the simulator are set such that experiments conducted at approximately $0.223\,\mathrm{Hz}$ experienced the highest acceleration with an acceleration of around $1\,\mathrm{m/s^2}$ RMS, while accelerations with lower and higher frequencies fall of linearly with frequency as can be seen in Fig. 2.3. For this reason, additional "virtual" test points with 0% symptoms were handed to the optimization algorithm. These were placed at a frequency of $1.5\,\mathrm{Hz}$ with a compensation of 100% and acceleration values corresponding to 1, 1.5 and $2\,\mathrm{m/s^2}$ RMS oscillations, therefore enforcing high-frequency roll-off.

2.3.4 Results

As described above, in total six different motion sickness prediction models, one for each motion sickness level of Table 2.1, were generated. The majority of literature on the subject however uses the Motion Sickness Incidence (MSI) metric introduced by

Table 2.3: The values of the optimized parameter vectors $\mathbf{p}_1$ to $\mathbf{p}_6$.

Mdl	K_a	K_{ac}	K_ω	$K_{\omega c}$	K_{vc}	τ	τ_a	τ_d	K_{out}
Orig.	0.1	1.2	0.9	4	6	5	190	7	1
1	0.0143	0.4859	1.7316	4.7373	1.1598	1.4053	162.2744	7.1613	2.7371
2	0.0198	0.6432	1.6274	4.2530	1.5417	1.2651	149.5719	7.2885	2.2895
3	0.0252	0.8076	1.6575	4.2136	2.7071	1.5723	167.5377	7.1589	1.7903
4	0.0276	0.8054	1.7272	4.3289	2.6063	1.6064	167.3826	6.9032	1.1866
5	0.0110	0.7420	1.7307	4.1625	2.7944	1.6805	150.6739	6.4697	0.9226
6	0.0462	0.8864	1.7157	4.3600	2.5651	1.6843	157.3176	7.0882	0.7547

O'Hanlon [31], which was pragmatically defined to be the percentage of people vomiting given a certain condition. Studies using MSI include the aforementioned motion sickness models by Kamiji et al. [44], the motion sickness model developed by Bos and Bles [20], and also the vertical oscillation model of the ISO 2631-1 [16]. The definition of MSI is equivalent to the Griffin motion sickness scale level 6. Donohew et al. [35] on the other hand, used motion sickness level 3 for fitting a motion sickness model for lateral acceleration as this level offered a good compromise between data fidelity and meaningful indication to ride comfort. The Griffin dataset offers lower data fidelity at high motion sickness levels, simply because the examined motions were not nausogenic enough such that only minor percentages of people reached the higher end of the Griffin motion sickness scale. The opposite is true for the low end of the motion sickness scale. Pretty much all people reached motion sickness level 1 and 2 resulting in an abundance of 100% values in the dataset. The optimized models solve this discrepancy poorly, which is why also the models for these motion sickness levels may deliver unsatisfactory results. Nevertheless for the sake of completeness, it was chosen to create six different motion sickness models, one for each motion sickness level defined in Table 2.1.

The optimized parameters are displayed in Table 2.3. Because of the optimization cost function which penalizes deviations in respect to one another, the parameters lie close together in general. An obvious trend can be observed for the parameter K_{out} which decreases from a value of over 2.7 for the model predicting MSD 1 to ≈ 0.75 for the model predicting MSD 6 as in general it is harder to reach these high sickness levels. The obvious choice for the optimizer was therefore to decrease the output value of the improved Kamiji model for higher MSD values by simply, decreasing K_{out}.
Other parameters such as $K_{\omega c}$, τ_d differ only marginally from one another and their initial value, while other factors such as K_a or τ show a large deviation from their original value. The parameters which were found to have considerably smaller values then the original model are the K_a, K_{vc} and τ parameters whereby the K_a parameter for

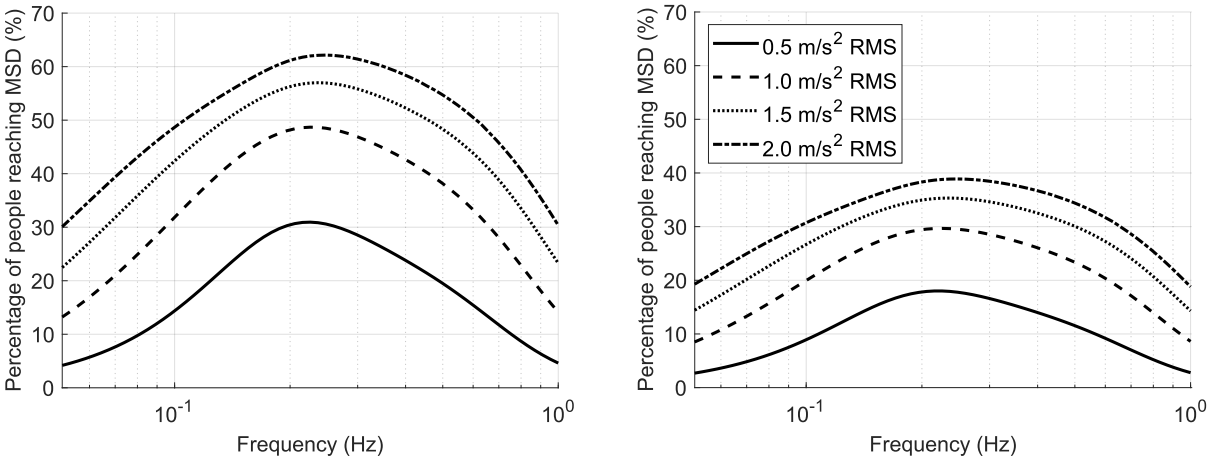

(a) Improved Kamiji model for MSD 4 **(b)** Improved Kamiji model for MSD 6

Figure 2.11: Sweep of the improved Kamiji model at two sickness levels for 100% compensation with fixed RMS values of acceleration

MSD 5 are determined to be only 11% of the original value. The K_ω value on the other hand was increased to a mean of 188% of its initial value. The parameter τ represents the time constant of the low-pass filter estimating the "subjective vertical". Bos and Bles [20], mentioned that this time constant was experimentally determined to be $2\,\mathrm{s}$ up to $20\,\mathrm{s}$ which is 3 to 12 times slower then the result of the optimization.
It is not trivial to interpret most of these changes meaningfully, however some insight of the resulting changes can be gained by plotting the predicted motion sickness for two of the six models under constant acceleration conditions at at 100% compensation as displayed in Fig. 2.11. Here it can be seen that both motion sickness prediction models exhibit a maximum at $\approx 0.25\,\mathrm{Hz}$ which lies close to $0.2\,\mathrm{Hz}$, the frequency at which literature places maximum motion sensitivity [35, 47].

Furthermore, the developed models can be plotted in conjuncture with the Griffin dataset. Because the Griffin dataset is recorded with the $12\,\mathrm{m}$ Tilting and Translating Cabin motion simulator which has a limits for maximum travel, velocity and jerk it can produce, the frequency of the realized oscillation for each testpoint is linked to jerk, acceleration, speed and travel of that testpoint as the simulator was always performing at one of these limits for the Griffin dataset. The exact relationship as well as the envelope were introduced in Eqs. (2.4) to (2.6) and visualized in Fig. 2.3. For example, the maximum acceleration at $0.1\,\mathrm{Hz}$ is limited by the maximum velocity this simulator is able to achieve and equates to roughly $A_{max}(f = 0.1\,\mathrm{Hz}) = 0.63\frac{m}{s^2}$, while at a frequency of $0.3\,\mathrm{Hz}$ the limit is the maximum achieved jerk of the simulator resulting in a maximum acceleration of $A_{max}(f = 0.3\,\mathrm{Hz}) = 1.04\frac{m}{s^2}$.
In order to compare the Griffin datapoints to the improved Kamiji model, the improved

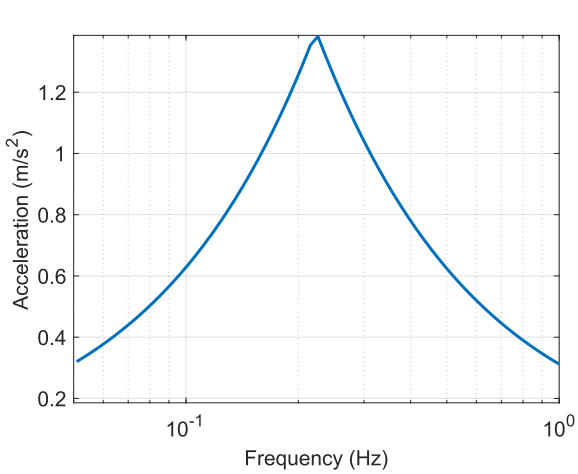

(a) Frequency dependent acceleration of the Southampton motion simulator

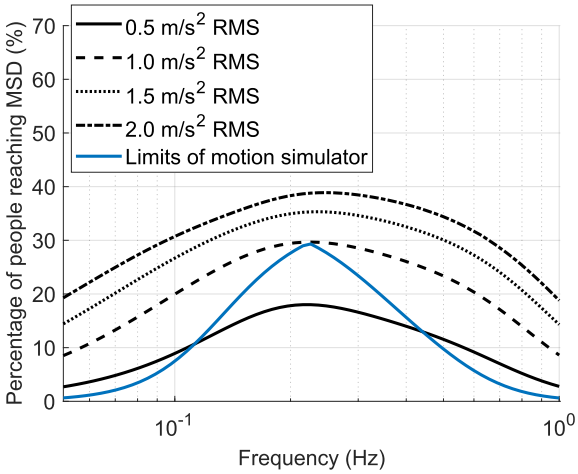

(b) Improved Kamiji model for MSD 6 evaluated at constant and Southampton motion simulator accelerations

Figure 2.12: Acceleration profile and effect on the improved Kamiji model

Kamiji model was evaluated at the acceleration limits dictated by the Griffin dataset. For convenience, these limits are again visualized in Fig. 2.12a. The output of the improved Kamiji model for MSD 6 in response to constant accelerations an to the acceleration limits of the Griffin dataset at $100\,\%$ compensation is plotted in Fig. 2.12b.
Given this linkage, the motion sickness prediction of the original and improved Kamiji model together with the data points of the Griffin simulator can be visualized in a common plot. In Fig. 2.13 and Fig. 2.14 the graphs are visualized for level 4 and 6 with compensation running from 0 to $100\,\%$. Note that the original Kamiji model with parameters taken from [44] only supplies values for MSI which would correspond to motion sickness level 6. For comparative reasons, the original Kamiji model was also plotted in the plot for motion sickness level 4 shown in Fig. 2.13.
As can be seen in these two figure, the improved Kamiji model shows better coherence to the Griffin test points in comparison to the original Kamiji model. This is true not only for the level 4 model shown in Fig. 2.13, but also for the level 6 model shown in Fig. 2.14. To some extent, this was to be expected due to the lower sensitivity of the MSI metric in comparison to the model predicting motion sickness level 4 or “mild to moderate nausea“, however for level 6 which should be directly comparable to MSI, the improved Kamiji model still shows 3x higher sensitiviy more accurately predicting the Griffin dataset.
Furthermore, it can be observed that the Griffin data points are spread out quite significantly in some places. For example, at MSD 4 at 50% compensation shown in Fig. 2.13 the Griffin dataset contain three vertically stacked test points indicating motion sickness of 10%, 25% and 45% for the same frequency of $0.2\,\mathrm{Hz}$. As expected and shown before,

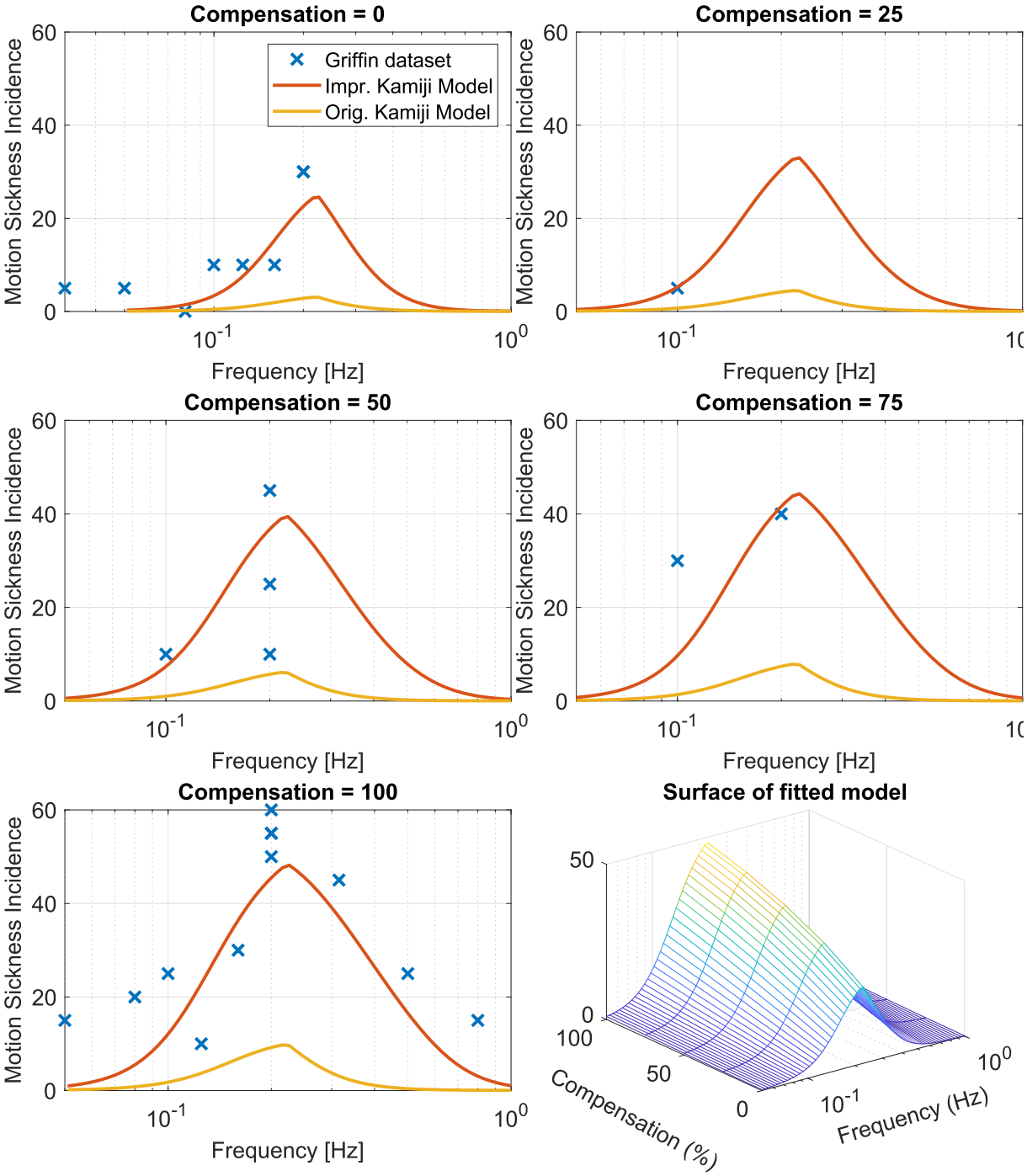

Figure 2.13: Fitting of original and improved Kamiji model to Griffin dataset with Griffin's motion sickness level 4 for acceleration profile of the Griffin dataset

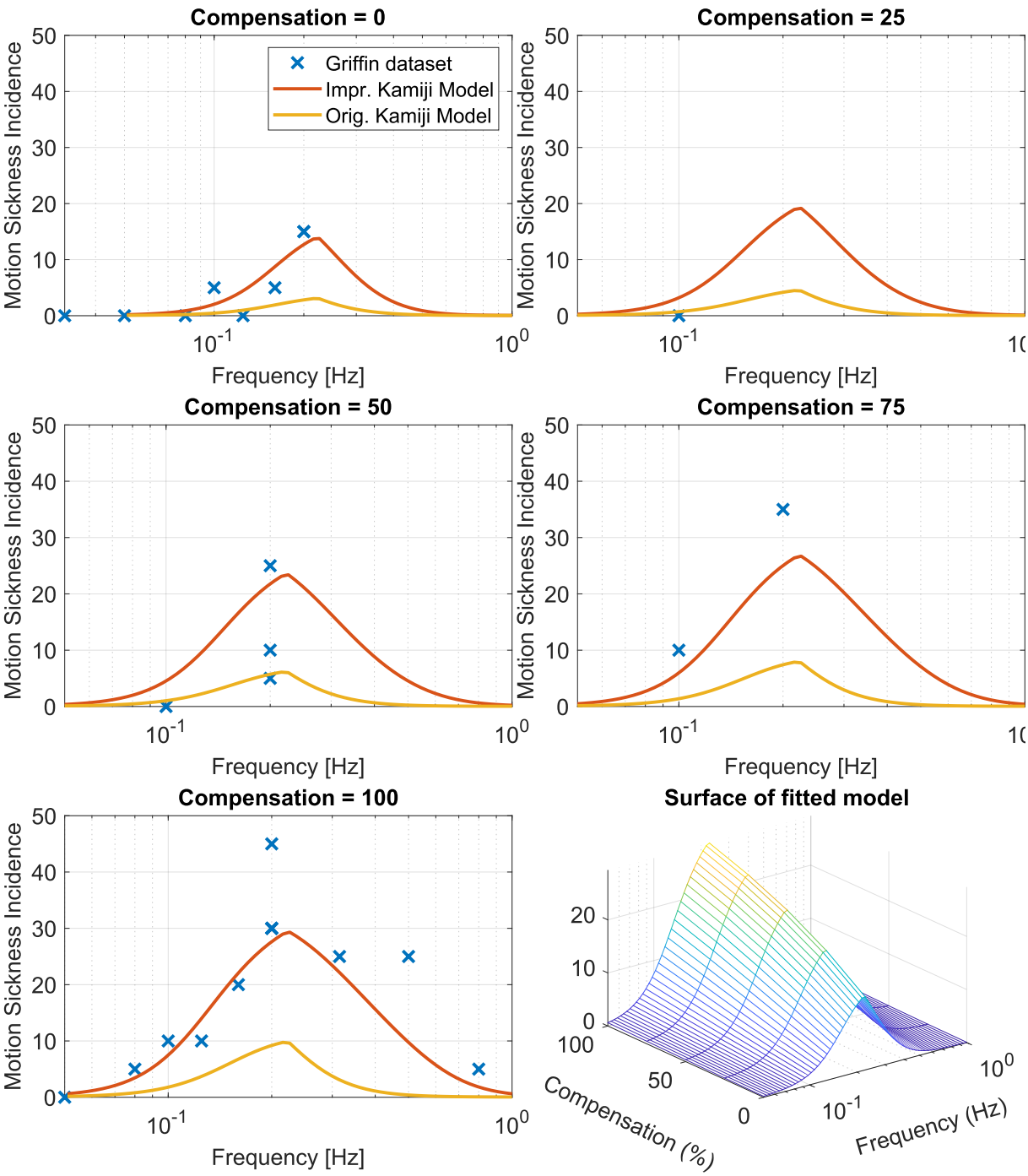

Figure 2.14: Fitting of original and improved Kamiji model to Griffin dataset with Griffin's motion sickness level 6 for acceleration profile of the Griffin dataset

a peak for all models is visible at $0.23\,\mathrm{Hz}$ which stems from the acceleration profile of the Griffin simulator as already shown in Fig. 2.12. In general however, the improved Kamiji model shows a good fit to the Griffin dataset confirming that the modifications as well as the optimization performed well.

Also worth noticing is that the amplitude of the improved Kamiji model is monotonically increasing with increasing compensation. This effect is not confirmed by experiments. Donohew et al. [40] stated that minimum motion sickness can be expected in the range of 25% to 50% of compensation. These findings were also experimentally confirmed by [24] who discovered that reducing the compensation value from 70% to 55% reduced the symptoms of motion sickness by $25 - 40\%$. Translated to Fig. 2.13 and Fig. 2.14, this would mean that a saddle shape of the 3D-plot has to be expected. The data points of the Griffin dataset do not represent these results as is evident in both Fig. 2.13 and Fig. 2.14. Furthermore, it is unknown if the improved Kamiji model could offer the flexibility to represent this expect saddle shape. In any way, the model cannot reproduce these results which should be kept in mind for the relevant applications.
It should be noted that especially for very low and very high motion sickness levels, the optimization conditions are not optimal. This is evident in Fig. 2.14 in which especially at 0% compensation practically all data points are zero or close to zero which incentivizes the optimization algorithm to fit a model which outputs zero at all times. Part of this problem is the relatively low number of test subjects reaching motion sickness level 6 during these conditions, apparently because the motion was too light to provoke satisfactory levels of motion sickness.

3 Flight Test Methodology

A motion sickness prediction model was designed in Chapter 2 based on a mix of an analytical model augmented with experimental data for the case of horizontal harmonic oscillation with roll compensation of the lateral acceleration. Naturally, such a model should be validated with data which mimics the intended purpose of the motion sickness model as close as possible. The intended purpose is that described in Section 1.5 and Section 1.4, which is stated to be horizontal, lateral oscillation with compensation at or close to 100%. The requirements for an experimental dataset, aimed at validating these results, are almost the same as for the Griffin dataset described in Section 2.3.1:

- Shall be experimental data on motion sickness
- Obtained with a suitable vehicle
- Sufficient number of test subjects/participants
- Consistent and well-documented test setup
- Well-documented and repeatable motion profile (frequency, amplitude, etc.), mimicking air taxi transport as outlined in Section 1.4
- Motion sickness of test subjects/participants recorded throughout the test

However, to the best of the author's knowledge, a dataset satisfying these constraints or at least a comparable dataset did not exist before the work of this thesis.

The following section shall first evaluate the usage of motion simulators in order to gather such an experimental dataset. Then, the approach of the flight test experiment design followed by a description of methodology involving technical aspects for pilot cueing, questionnaires and data gathering will be shown.

3.1 Computing Motion Simulator Envelopes

Motion sickness experiments are often conducted inside motion sickness simulators such as the $12\,\mathrm{m}$ Tilting and Translating Cabin motion simulator operated by the Institute of Vibrations of the University of Southampton as well as DLR's Air Vehicle Simulator (AVES) Fig. 3.1. The key advantage of a motion simulator in contrast to flight tests it the decreased cost. Motion simulators are in general cheaper than flying vehicles while also offering better availability and lower turn-around time resulting in more useful test-time. For this reasons, it is worthwile to consider the use of a motion simulator for motion sickness tests. In the following, the question is discussed if a simulator, especially DLR's AVES, can serve as a platform for executing motion sickness tests in the context of this thesis.

A convenient way of displaying the limitations of motion simulators in respect to their displacement, velocity and acceleration limits both in translation and rotation, is to plot the displacement envelope of the given motion simulator. This task is relatively trivial if a translational harmonic oscillation is assumed and therefore only limitations of displacement, translational velocity and translational acceleration are taken into account.

(a) DLR's Air Vehicle Simulator AVES

(b) The 12 m Tilting and Translating Cabin motion simulator

Figure 3.1: Two different motion simulators

Differentiating the equation for a harmonic oscillation

$$x(t) = A_{dis} \cdot \sin(\omega t) \tag{3.25}$$

three times, one arrives at

$$\dot{x}(t) = A_{dis} \cdot \omega \cdot \cos(\omega t) \tag{3.26}$$

$$\ddot{x}(t) = -A_{dis} \cdot \omega^2 \cdot \sin(\omega t) \tag{3.27}$$

$$\dddot{x}(t) = -A_{dis} \cdot \omega^3 \cdot \cos(\omega t) \tag{3.28}$$

with $x(t)$ denoting displacement, A_{dis} the translational displacement amplitude and ω the frequency. In order to evaluate the displacement envelope, the respective limits for displacement, velocity and acceleration have to be inserted into Eqs. (3.25) to (3.28) which then can be solved for the displacement amplitude A_{dis} in order determine the maximum permissible displacement of that specific limit at that specific frequency. This relationship can then plotted for a given set of displacement, velocity and acceleration constraints as displayed in Fig. 2.3 for the $12\,\mathrm{m}$ Tilting and Translating Cabin. From this graph, the engineer can then quickly deduct at which frequencies the amplitude, velocity or acceleration limit, constrain the oscillation. For the case of the $12\,\mathrm{m}$ Tilting and Translating Cabin, from Fig. 2.3 we can deduct that in the frequency band relevant for motion sickness the simulator is *not* constraint by the massive $12\,\mathrm{m}$ track, but rather by the maximum velocity of the simulator. Such information helps to identify constraints of a given simulator quickly.

Table 3.1: Horizontal motion limits of the AVES and Southampton motion simulator, taken from [48] and [35]

	x_{max}	$\dot{x}_{max}$	$\ddot{x}_{max}$	max. φ	max. ω	max. $\dot{\omega}$
AVES	$1.26\,\mathrm{m}$	$1\,\frac{\mathrm{m}}{\mathrm{s}}$	$0.66\,\frac{\mathrm{m}}{\mathrm{s}^2}$	$27\,^\circ$	$21\,\frac{^\circ}{\mathrm{s}}$	$140\,\frac{^\circ}{\mathrm{s}^2}$
Southampton	$12\,\mathrm{m}$	$1\,\frac{\mathrm{m}}{\mathrm{s}}$	$1.96\,\frac{\mathrm{m}}{\mathrm{s}^2}$	N.A.	N.A.	N.A.

In case of the AVES, the situation is however slightly more complicated. The oscillation defined in Section 1.4, are however a combined translatory and rotatory oscillation. While the AVES is capable of simulating such motion, the formulas Eqs. (3.25) to (3.28) only describe oscillations in the horizontal plane. Without loss of generality, assuming a lateral translational oscillation with a synchronized rotational oscillation at the same frequency equivalent to 100% compensation, we can formulate the connection

$$\tan\varphi = \frac{a_y}{g} \tag{3.29}$$

between the roll-angle φ and the lateral acceleration a_y. Given the substitution

$$A = \frac{A_{dis} \cdot \omega^2}{g} \tag{3.30}$$

and inserting the lateral oscillation of Eq. (3.27) into Eq. (3.29) yields

$$\varphi(t) = \arctan\left(-A \cdot \sin\left(\omega t\right)\right). \tag{3.31}$$

Now differentiating Eq. (3.31) twice, one arrives at

$$\dot{\varphi}(t) = -\frac{A \cdot \omega \cdot \cos(\omega t)}{A^2 \cdot \sin^2(\omega t) + 1} \tag{3.32}$$

$$\ddot{\varphi}(t) = \frac{A \cdot \omega^2 \cdot \sin(\omega t) \cdot (A^2 \cdot \cos(2 \cdot \omega t) + 3 \cdot A^2 + 2)}{2 \cdot (A^2 \cdot \sin^2(\omega t) + 1)^2}. \tag{3.33}$$

In order to determine the motion simulator limits, the maximum values of Eqs. (3.25) to (3.27) and (3.31) to (3.33) have to be found. It is easy to realize that the equations of this harmonic oscillation reach their maximums at

$$t = \frac{\pi}{2\omega} \pm k \cdot \frac{2\pi}{\omega} \tag{3.34}$$

for position and acceleration terms (e.g. Eqs. (3.25), (3.27), (3.31) and (3.33)) and at

$$t = 0 \pm k \cdot \frac{2\pi}{\omega} \tag{3.35}$$

for velocity terms (e.g. Eqs. (3.26) and (3.32) with $k = 1, 2, ...$).

Inserting these back into Eqs. (3.25) to (3.27) and (3.31) to (3.33), finally yields the maximum values for the different equations:

$$x_{max} = A_{dis} \tag{3.36}$$

$$\dot{x}_{max} = A_{dis} \cdot \omega \tag{3.37}$$

$$\ddot{x}_{max} = A_{dis} \cdot \omega^2 \tag{3.38}$$

$$\varphi_{max} = \arctan(-A) \tag{3.39}$$

$$\dot{\varphi}_{max} = A \cdot \omega \tag{3.40}$$

$$\ddot{\varphi}_{max} = \frac{A \cdot \omega^2 \cdot (2A^2 + 1)}{(A^2 + 1)^2} \tag{3.41}$$

Note that because of the symmetric nature of such oscillations, k of Eqs. (3.34) and (3.35) was chosen such that positive results are obtained.
Lateral translational oscillation accelerations are typically small. Additionally, motion sickness frequencies are centered below $1\,\mathrm{Hz}$. Therefore, it is possible to assume that $A \ll 1$, thus quadratic and higher terms can be neglected and $\arctan(x) \approx x$. With these assumptions, Eqs. (3.39) to (3.41) can be simplified which yields

$$\varphi_{max} = -A \tag{3.42}$$

$$\dot{\varphi}_{max} = A \cdot \omega \tag{3.43}$$

$$\ddot{\varphi}_{max} = A \cdot \omega^2. \tag{3.44}$$

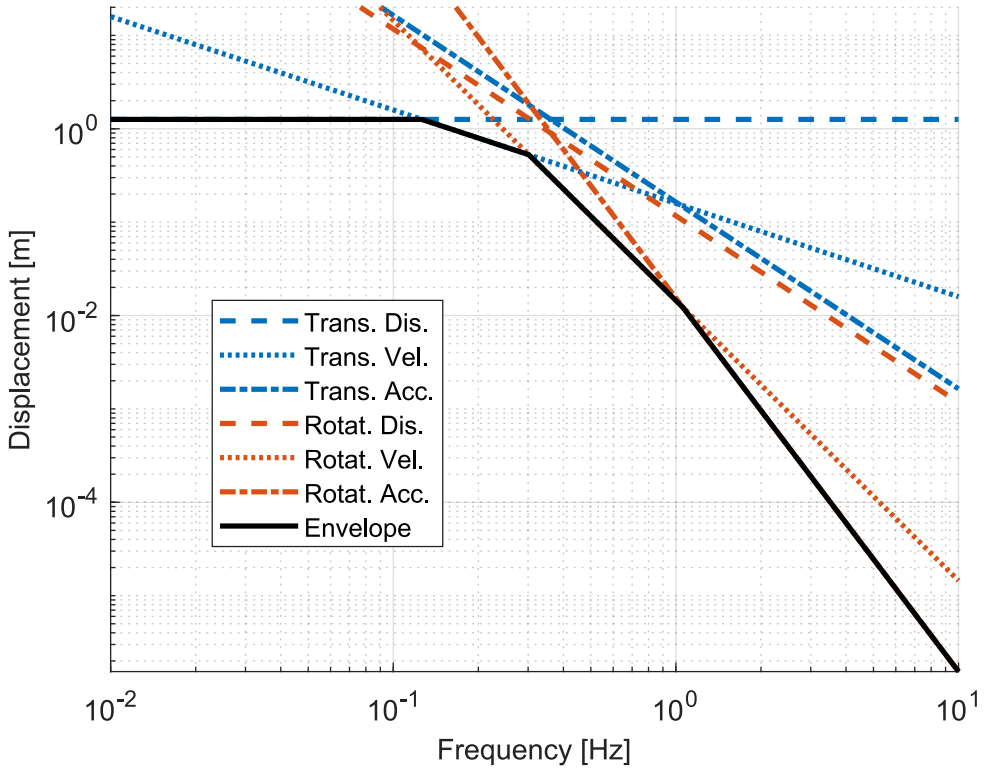

Figure 3.2: Limits of DLR's Air Vehicle Simulator for fully compensated lateral oscillations expressed as displacement limits. Graph displayed without time delays

By solving Eqs. (3.36) to (3.38) and Eqs. (3.42) to (3.44) for A_{dis} and inserting the respective limits of the motion simulator given in Table 3.1, one obtains the limit of the simulator expressed as displacement limits. For DLR's Air Vehicle Simulator (AVES) and its limits given in Table 3.1, the approach described above results in Fig. 3.2 similarly to Fig. 2.3 discussed earlier.

This graph shows the resulting maximum displacement as a result of limits in acceleration, velocity and displacement under the assumption that the motion is a coupled translational and rotational oscillation as described above. Every acceleration, velocity and displacement limit, either translational (displayed in blue) or rotational (displayed in red) is converted to a displacement limit and displayed in Fig. 3.2. The resulting envelope is displayed as a thick black line. Displacement limits (naturally) yield a horizontal line, whereby velocity and acceleration limits restricted the maximum available displacement for higher frequencies. Note that due to the order of Eqs. (3.37), (3.38), (3.40) and (3.41), it is convenient to display the results in a double log plot. The same process can be repeated for rotational displacement. For this, the limits found for A_{dis} in Fig. 3.2 have to be substituted back into Eq. (3.39). This then yields Fig. 3.3.

Fig. 3.2 and especially Fig. 3.3 show that the AVES simulator offers an only very limited motion range overall. This can be illustrated by a short calculation: Based on the

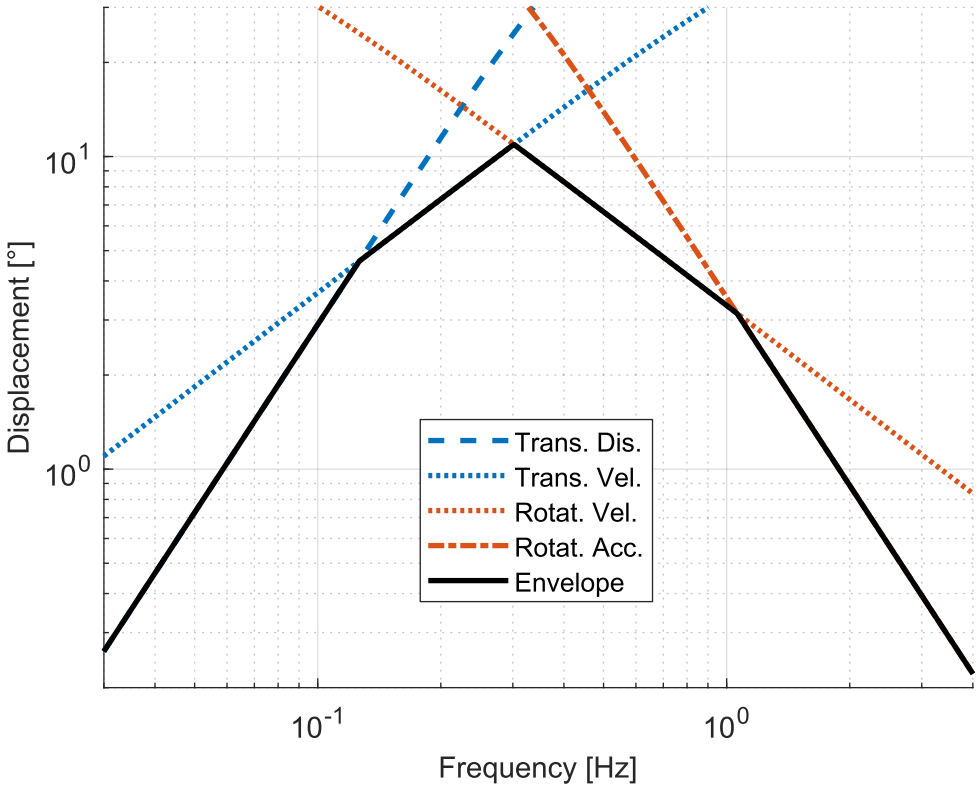

Figure 3.3: Limits of DLR's Air Vehicle Simulator for fully compensated lateral oscillations expressed as rotational limits. Note that translational acceleration limits and rotational angle limits were neglected, as these do not influence the limit envelope

formula for calculating the bank angle for a coordinated curve

$$\varphi = \tan^{-1}\left(\frac{V^2}{g \cdot R}\right) \tag{3.45}$$

a rough calculation involving the typical flight speed and curve radius can be performed. This reveals that already at $60\,\mathrm{knots}$ airspeed and a curve radius of only $250\,\mathrm{m}$, a bank angle of $20°$ is needed for a fully coordinated curve. As can be seen in Fig. 3.3, the AVES is not capable of simulating bank angles in excess of approximately $11°$ at best under the assumptions of motion detailed above. For lower frequencies, the performance is even worse. This of course, is a general trait of motion flight simulators. While these are designed to provide the most realistic visual representation and corresponding motion feeling possible, they of course have to cope with limited actuator travel of the motion system. This problem is typically solved by replacing an actual movement with a close representation which *feels* similar to the pilot [49, 50]. Typically, a combination of filters and strategies is employed to derive a set of feasible commands for the motion system. First and foremost, low frequencies of the translational and rotational motions are eliminated by a set of high-pass filters (washout filters) which simulated quick and transient motions while lower frequencies are filtered out to limit the resulting (actua-

tor) travel. This way, sustained linear accelerations can be emulated by slowly tilting the cabin such that the gravitational force simulates low frequency acceleration, while the slow rotational motion stays under the limit of human perception. Lastly, a centering algorithm has to be implemented which slowly re-centers the motion simulator in the middle of the actuator travel such that future motions can be effectively executed [51]. This design is naturally aimed at exploiting the limited detection capabilities of the human vestibular system. Because it is unknown how these classical motion simulator techniques interact with motion sickness, these cannot be used for emulating motion in flight simulators. It is therefore concluded that the AVES motion simulator only offers limited fidelity for the use cases formulated in this thesis. In contrast to this, a flying vehicle such as an helicopter offers several key properties which are advantageous for generating relevant data:

1. The visual stimulus of test subjects is comparable to the intended purpose
2. No restrictions concerning bank angle or displacement limits
3. Realistic vibration environment

Due to these reasons and the fact that the German Aerospace Center operates a fleet of different aircraft and helicopters, it was decided to perform a series of flight tests in order to create the needed motion sickness dataset.

3.2 Flight Test Goals

The intended purpose of the ensuing dataset is twofold:

1. **Validation of the developed motion sickness prediction model**
2. **Acquisition of a motion sickness dataset for helicopters for general use**

While the first goal is obviously important for the remainder of this thesis, the latter aims at facilitating research on this topic for other researchers. A well-characterized and well-documented flight test for motion sickness might have multiple benefits for different research directions, such as other motion sickness metrics, the design of new flight control system algorithms or for comparative studies with new or existing aircrafts. Furthermore, to the best of the author's knowledge, currently no dataset on motion sickness exists which contains motion sickness data and the motions of the rotorcraft. For these reasons, it is aspired to make this dataset publicly available with all collected data.

In the following the different aspects of the flight tests will be described. First, the general design of the experiment will be shown, followed by the data acquisition and processing approach, flight test execution and an analysis and discussion of the results.

3.3 Experimental Design

The general idea of the flight tests or flight experiment, is to fly an appropriate oscillation which shall provoke motion sickness of test subjects. The exact motion shall be recorded by a suitable measurement device while the test subjects rate their motion sickness via a motion sickness questionnaire. As known from literature, motion sickness is primarily dependent on the frequency of the oscillation [16], therefore several frequencies shall be flown in this experiment in order to build a trend.

For the flight tests, it was decided to use DLR's Bölkow BO-105 Helicopter, registration sign D-HDDP (Fig. 3.4a). While this helicopter when compared to DLR's most modern helicopter the ACT/FHS (Fig. 3.4b), does not feature experimental electronics for recording its flight state or active control inceptions in order to computerize the controls of the helicopter, it *is* equipped with seats for two pilots and three passengers, therefore offering the possibility to fly several passengers at once saving costs and effort. The plan

(a) DLR's Bölkow BO-105 helicopters, registration sign D-HDDP

(b) DLR's ACT/FHS a heavily modified Eurocopter EC135, registration sign H-HFHS

Figure 3.4: DLR's helicopter fleet

of the experiment was to fly the helicopter on a sinusoidal trajectory with a fixed frequency, therefore the helicopter pilot would command a series of coordinated turns. It was decided to concentrate the experiment on effects of different frequencies, as earlier literature studies found out that motion sickness is primarily a function of the oscillation frequency [16]. The total length of the experiment was chosen to be 30 minutes of oscillation without considering necessary flight time to take-off, flight to the experiment zone, flight from the experiment zone to the airport and landing. The choice of

30 minutes is not arbitrary, but rather reflects the experiment time of the Griffin dataset and therefore increases compatability and comparability between the different datasets and also closely matches the trajectory assumptions of Section 1.4 for UAM vehicles.

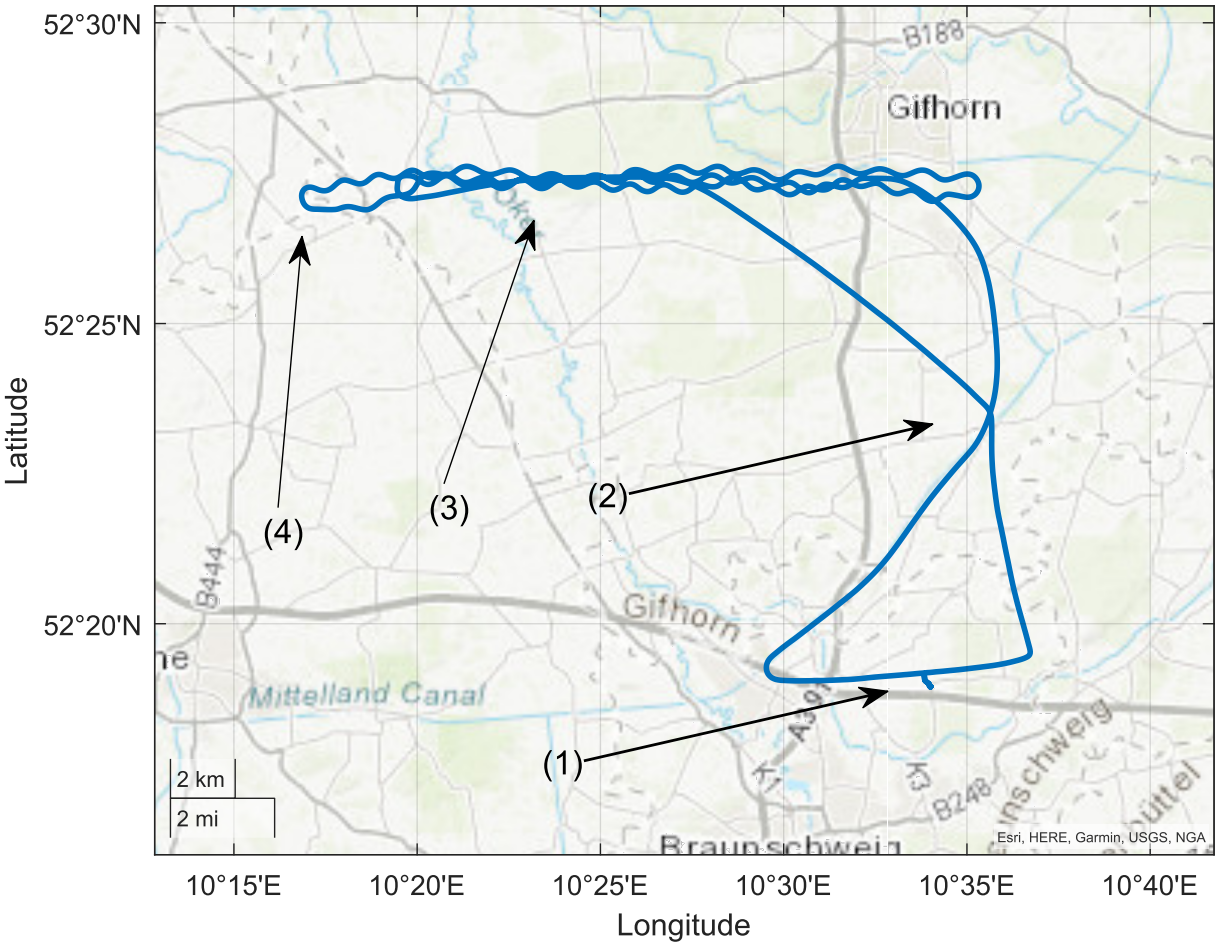

Figure 3.5: The trajectory of flight test #1, representative of a typical flight test. (1): Start/landing at Brunswick airport, (2): Transit flight to the test track, (3): 3x10 minutes horizontal oscillation legs, (4): turn-around curve between experiment legs

After some discussion with the test pilots and after conducting two experimental pre-flights in order to explore and validate the boundary conditions of the aircraft, aircrew and experiment, it was furthermore decided to only take two test subjects per flight. On the one hand, this measure ensured a less crowded cabin and therefore improved the comfort level of the remaining passengers as it was feared that a higher passenger density might negatively impact the speed of motion sickness onset [52]. On the other hand, this made the middle seat available for installation of a smartphone equipped with a special recording and logging software which plays a critical role in the data acquisition methodology as will be described in Section 3.6.2. In these pre-experiment test-flights, it was also determined that the maximum attainable frequency for a controlled harmonic side-to-side oscillation with simultaneous banking of the helicopter

would be $f \leq 0.1\,\mathrm{Hz}$ at a bank angle of $\varphi = 20°$. It should be noted that due to its innovative rotor design and resulting unprecedented maneuverability, the Bölkow BO-105 helicopter is the only helicopter in the world to have been certified as an aerobatics helicopter. Naturally, this highly agile machine is capable of achieving much higher oscillation frequencies. However, in the pre-flight tests it was determined that the test pilots were not able to steer the helicopter on a sinusoidal trajectory accurately enough above frequencies of $0.1\,\mathrm{Hz}$. It is worth pointing out that helicopters and VTOL systems such as the envisioned UAM which are controlled by digital flight control systems might possess the ability to accurately follow higher frequencies, however such systems were not available for the planned experiments.

Two test pilots were onboard each flight, one pilot flying who steered the helicopter on the sinusoidal path and one pilot non-flying in charge of look-out, communication with the tower as well as leading the experiment and communication with the test subjects. In order to enable the pilot flying to accurately steer the helicopter on a sinusoidal trajectory at the requested frequencies, an auditive cueing system was implemented which is described in detail in Section 3.4. At each flight experiment only one of a total of three discrete frequencies ($0.025\,\mathrm{Hz}$, $0.05\,\mathrm{Hz}$ and $0.1\,\mathrm{Hz}$) was used. Thus every flight was set up such that one of these three frequencies was exclusively flown. This was chosen in order to obtain an even spread of frequencies, therefore enabling the data to build a trend. The other reason for choosing exactly one frequency per flight, is that each test subject experiences only one frequency which benefits the clarity of data, as motion sickness stimuli are not mixed. It should be noted that initially higher frequencies of up to $0.2\,\mathrm{Hz}$ were planned for the flight tests, as at this frequency peak motion sickness is expected according to [16]. However, the aforementioned constraints did not allow to fly coordinated harmonic oscillations with frequencies higher than $0.1\,\mathrm{Hz}$.

Each 30 minutes experiment was divided into three ten minutes consecutive legs connected by a turn-around curve at the end of each leg. This measure should not only limit the flight test area, therefore shortening flight to and from the area, but also the flight test could be performed along a railroad which was suggested by the test pilots as a good landmark for orientation and would help the pilots to fly in a relatively straight line. As this railway line is situated out of controlled airspace, the flight tests could be performed without interfering with other air traffic. An example of the resulting trajectory is shown in Fig. 3.5.
As the Bölkow BO-105 helicopter is certified for Visual Flight Rules (VFR) only, all tests had to be conducted in clear flight weather. This offered the additional advantage that the tests all took place during relatively calm weather, with unhindered view from the

Figure 3.6: The helicopter boarded with two test subjects and two test pilots

helicopter.

3.3.1 Flight Test Execution

A total of 16 flights with 32 test subjects were scheduled and conducted in two flight test campaigns with 16 female and 16 male participants. The first campaign with seven flights took place from 13th to 16th of September 2021 with medium wind conditions and was terminated due to tail-rotor gearbox problems. After these problems were resolved, a second flight test campaign was conducted from 19th to 21st of October 2021 in slightly heavier wind conditions. The according data is listed in Appendix B in Table B.2 to Table B.6. While only two flights per day were scheduled in the first flight campaign, with increasing routine and experience, three flights per day could be realized for the second flight test campaign. An overview of the conducted flights and according dates is listed in Table 3.2.

For the flight tests, exclusively DLR employees mainly from the Institute of Flight Systems were recruited as test subjects. Most female participants were recruited from other institutes in order to achieve a $50-50$ gender ratio. No monetary compensation for participation was offered to the test subjects. DLR external test subjects could not be flown on the BO-105 helicopter due to insurance reasons. As the flight tests took place in 2021 during the Covid-19 pandemic, a mandatory corona concept was implemented for these tests. The plan detailed that only test persons could participate who proofed that

Table 3.2: Overview of performed flight test with according date and frequency flown

Flight ID	Flight test campaign	Date	Frequency (Hz)
1		13.09.2021	0.025
2		13.09.2021	0.05
3		14.09.2021	0.1
4	#1	14.09.2021	0.025
5		15.09.2021	0.1
6		16.09.2021	0.025
7		16.09.2021	0.05
8		19.10.2021	0.05
9		19.10.2021	0.1
10		19.10.2021	0.025
11		20.10.2021	0.05
12	#2	20.10.2021	0.1
13		20.10.2021	0.025
14		21.10.2021	0.05
15		21.10.2021	0.1
16		21.10.2021	0.1

they received a double vaccination against Covid-19 as well as a negative rapid test in the last 24 hours. Additionally, it was required that all participants wore a FFP2 filtering half-mask during briefing. The requirement was relaxed in the second flight test, in which only a FFP2 filtering half-mask was required.

Before each flight, a briefing was held with all participating parties, which included a safety briefing and a briefing concerning the procedure of the test flight. This briefing introduced the basic goals, the questionnaires which will be introduced in Section 3.5, the symptoms of motion sickness and the general rules of conduct in flight. The test subjects were instructed to take a comfortable posture in-flight and to look out of the cabin while indicating their motion sickness every two minutes on an in-flight questionnaire. The reason behind this instruction is the intended purpose of the experiment as stated in Chapter 2: The passengers are assumed to be not accustomed to this mode of transport and are therefore assumed to be looking out in order to enjoy the flight. It is argued that such a behavior can be assumed for passengers riding this kind of transport for the first time. Additionally, this assumption is a worst case assumption as no previous adaptation to the motion stimulus could have occurred. As an extension to this assumption, it was furthermore specified that test subject were not allowed to use the smartphones or other devices until *after* the test was completed, therefore after the

three test segments were finished and the helicopter was on its return flight. These instructions were issued to improve comparability between all flights.
After this introduction, the pilots and the two test subjects boarded the helicopter. The data acquisition system was checked and activated, then the helicopter engines were started, the helicopter took off and proceeded to fly to the test area. Upon arrival, the flight test was started by the test pilots. While the pilot flying manually flew the sinusoidal trajectory, the pilot non-flying oversaw the test. This mainly included signaling the test subjects every two minutes to make a cross on their respective in-flight questionnaires described in Section 3.5. The test subjects indicated their motion sickness state on the Griffin motion sickness scale from 0 (no symptoms) to 6 (moderate nausea and want to stop) as listed in Table 2.1. Again, this scale was used for better comparability with the Griffin dataset.

The pilot non-flying indicated to the test subjects and pilot flying when each ten minute segment was completed, upon which the helicopter was turned around and the next segment began. If a test subject indicated a motion sickness level of "6 - Moderate nausea and want to stop the experiment", the test subjects were instructed to abort the experiment and communicate this to the pilot. Upon this event, the helicopter crew was instructed to abort the experiment immediately and fly back to the airport. When the three test segments where completed nominally, the helicopter returned to the airport, the questionnaires were collected and the general impression by the crew and test subjects was recorded. Additionally, the data acquisition was stopped and the data transferred to a laptop computer.

One single sortie took about 50 to 60 minutes of flight time. In Fig. 3.8 a good representation of how this time is divided between the different segments of the flight is shown: Around 4 minutes for take-off and landing (1), 11 minutes to get to the experiment zone and another 11 minutes to fly back to the airport (2), 30 minutes of experiment time, in which the sinusoidal oscillations are flown (3) and around 1 minute for each turn around (4) summing up to a total flight time of around 58 minutes.

Also note that some spikes in the roll angle reach higher than $35°$. These can be explained with two effects: As mentioned before, some test subjects were recruited from DLR staff from the Brunswick Institute of Flight Systems. A lot of these employees hold private pilots licenses and therefore are much more accustomed to motions of an aircraft than non-pilots. After completing the experiments the test subjects prompted the pilots to show off the capabilities of the helicopter which the test pilots were very willing to do. This resulted in a number of unusual flight attitudes. Because of the undesired good adaptation to the motions of aircraft and the therefore higher than usual threshold for

Figure 3.7: The digital kneeboard running the custom iOS app described in Section 3.4

motion sickness, pilots of all sorts were excluded as test subjects for the second flight test campaign.
Additionally, the pilots felt compelled to fly very aggressive banking maneuvers at take off with some test subjects. This behavior was subsequently prohibited in order not to provoke motion sickness before the experiment began. Some test subjects still exhibited slight signs of motion sickness even before the experiment began.

3.4 Pilot Cueing

For the experiment, the pilot was tasked with flying coordinated harmonic oscillations at fixed frequencies. Because of the lack of automation alternatives, the helicopter had to be manually flown during the entire time. The task of flying a helicopter without autopilot support is a challenging one on its own: The pilot needs to simultaneously stabilize the velocity, height, pitch, roll and yaw axis. Additionally, because of the nature of helicopter control, the helicopter dynamics are coupled. This means that the pilot controls do not act on one output alone. For example, the purpose of the collective stick is to command the helicopter to increase the collective pitch angle of the rotor blades which prompts the helicopter to climb. However, if this command is given by the pilots, the additional air drag of the rotor blades will also induce an undesired yaw motion. This in turn also leads to small responses in the pitch and roll axis. Therefore, by giving one control input, the helicopter reacts in several ways. Controlling this coupled motion

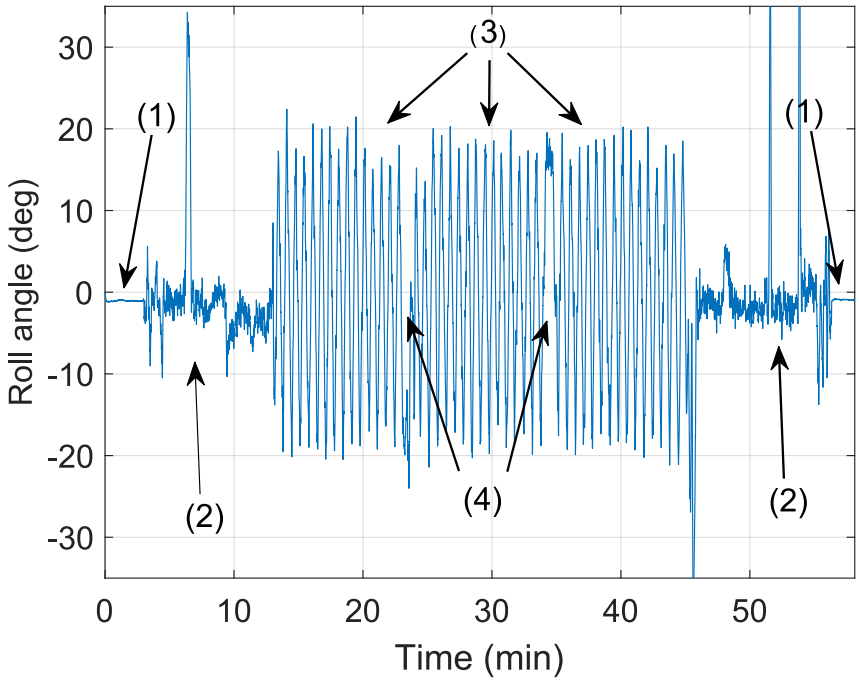

Figure 3.8: Plot of the roll angle of flight test #1, representative of a typical flight test. (1): Start/landing at Brunswick airport, (2): Transit flight to/from the test track, (3): 10 minutes horizontal oscillation legs, (4): turn-around curve between experiment legs

is a demanding job and accounts for much of a pilot's workload during flight. To enable the pilot to accurately follow the requested coordinated harmonic roll oscillation at serveral frequencies, a pilot cueing system was needed. Such as system would enable the pilot to fly the maneuvers precisely without overwhelming workload.

A pilot cueing system indicates to the pilot how to steer the helicopter such that a given task is executed. Additionally, this cueing system should be realized so that no additional hardware or permanent installation was needed, in order to avoid the high cost and time effort of certifying additional modifications of the helicopter. Three general types of cueing systems exist: Tactile cueing systems [53], visual cueing systems [54] and auditive cueing systems [55], however most of the time a combination of these systems is deployed [56]. As it was not possible to install any additional hardware, tactile cueing systems were discarded early. The intuitive solution of using a visual cue, in which a replication of the primary flight display with an artificial horizon overlaid with a second cross indicating the "desired" roll-attitude of the helicopter was evaluated as shown in Fig. 3.9a. This visual cueing system was intended to be displayed on the pilot's digital kneeboard, an Apple iPad, also visible in Fig. 3.7. However, it was soon discovered that this approach would require the pilot to always fly "head-down" looking at his kneeboard, which on the one hand is not allowed for a helicopter piloted in a VFR certification setup, and on the other hand makes it very hard to steer the other

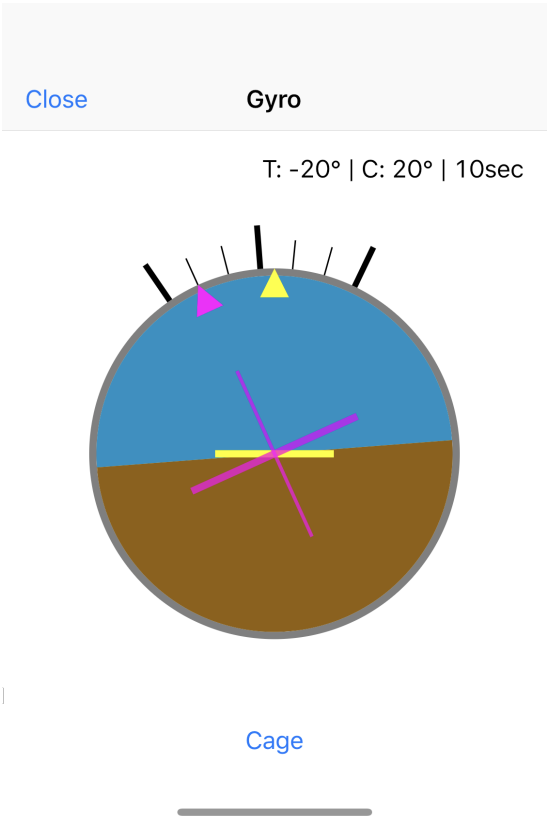

(a) The visual cueing artificial horizon display. Displayed in yellow and as an artificial horizon is the current roll attitude, while displayed in magenta is the desired roll attitude

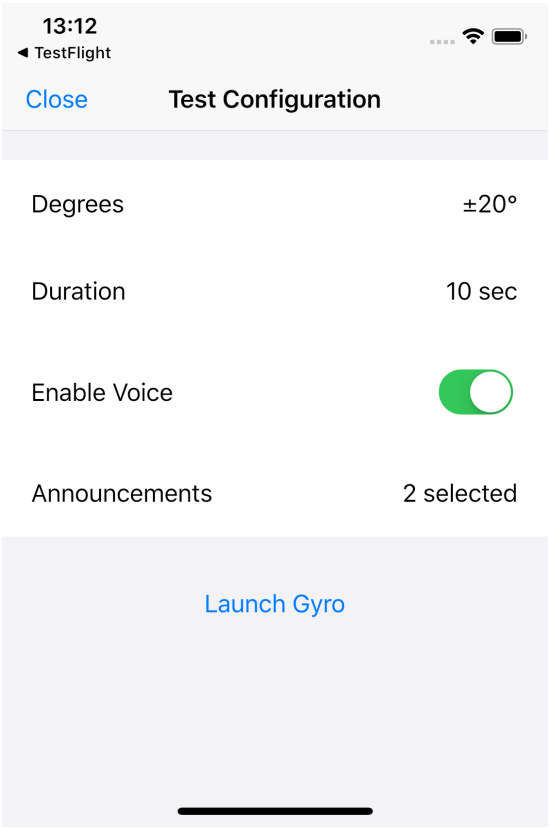

(b) The configuration screen of the IOS app. This page allows the user to configure the different settings of the cueing system

Figure 3.9: The DLR IOS Cueing App, specifically programmed for the flight tests with the BO-105 helicopter

axes of the helicopter as he lacks the visual cues such as horizon movement etc. from the outside view. Additionally, as the data source for the artificial horizon are the iPad's sensors which is unstably mounted on the knee of the pilot, this artificial horizon would display only very inaccurate data.

For this reason, an auditive cueing system was devised, which indicates the desired roll angle with the help of verbally spoken absolute roll angles. Therefore, the system would indicate the desired oscillating roll attitude by verbally stating the current roll angle which has to be flown, e.g. the system would announce: "0 *pause* 10 *pause* 20 *pause* 10 *pause* 0 *pause* -10 *pause* -20 *pause* -10 *pause* 0 etc." whereby the timing of the call outs of these numbers was chosen such that these describe a sinusoidal curve with an amplitude of $20°$. The task of the pilot was then to "capture" this sinusoidal curve and "interpolate" the roll angle between the different call outs smoothly. This approach was first tested in a mock-up in the AVES and then programmed as an iOS application which could be loaded onto the Apple iPad digital kneeboard of the pilots. The implementation of the app was outsourced to an external programming studio focusing on mobile apps. In the helicopter, the call outs were relayed to the intercom system of the helicopter via an appropriate cable, and therefore could be heard over the headsets of the pilots. Training the pilots on this approach proved to be easy. Pilots quickly adapted to the task, consisting of flying a sinusoidal curve and using the verbally spoken call outs as support or reminder while executing this oscillation. A good example is the "0" call out, at which the pilots knew that the horizon had to be level. This served as an intermediate "waypoint" at which the pilot knew that he had to increase or decrease the speed of the oscillation depending on the timing between the call out "0" and when the horizon actually was observed to be level. The same applies for the "20" and "-20" call out, which again served as "waypoints" for the extreme values of the harmonic oscillation. The IOS application also allowed the frequency selection of the harmonic oscillation and also an announcement density, governing at which roll angle intervals a call out would occur, as can be seen in Fig. 3.9b.
The performance of this cueing system will be evaluated in Section 4.2.2.

3.5 Questionnaires

In order to question the test subjects in preparation and during the flight tests, two types of questionnaires were used. A pre-flight questionnaire intended to determine general information about the motion sickness history of the test subject in question, and a second in-flight questionnaire, which the test subject had to fill out during the

flight tests in order to indicate his/her motion sickness state. In the following, both questionnaires will be presented.

3.5.1 Pre-flight Questionnaire

Motion sickness susceptibility differs significantly amongst the population [16, p. 27]. For this reason, a standardized approach to judge the individual susceptibility can be helpful in selecting the test subjects and in distributing these amongst the test conditions to prevent unintentional statistical dependencies. In order to avoid pitfalls in designing a suitable questionnaire, the motion sickness history questionnaire by Griffin and Howarth was adopted and extended [19]. The resulting questionnaire is called the pre-flight questionnaire in the following. The original motion sickness history questionnaire was designed in order to determine the personal susceptibility of an individual via a total of 15 questions regarding their travel behavior on relevant modes of transport, the occurrence of any motion sickness symptoms during these travels and their general health. Furthermore, the questionnaire is supplemented with a methodology of assessing the given answers via a set of measures, regarding the susceptibility of the given individual. For this, a number of metrics are calculated which will be presented in the following. A typical question of this questionnaire is given in Fig. 3.10. For the sake of applicability of this motion sickness history questionnaire to the flight

2. In the past YEAR, how many times have you felt ill, whilst travelling AS A PASSENGER in the following types of transport?

	NEVER	1	2	3	4-7	8-15	16+
CARS							
BUSES							
COACHES							
SMALL BOATS							
SHIPS							
AEROPLANES							
TRAINS							

Figure 3.10: Question 2 of the motion sickness history questionnaire taken from [19], as an example of a typical question

tests conducted in this thesis, small adjustments to the questionnaire were performed. These include the addition of a further category named Helicopters ("Hubschrauber" in German). Additionally, the category aeroplanes was split into a category for small aircraft, e.g. general aviation aircraft and commercial airplanes. Therefore, the changes

increased the number of rows from seven to nine. It is clear that the addition of helicopters to the questionnaire is necessary in order to discern people who have already flown on helicopters. Such distinction is necessary for the flight tests performed for this thesis, as it directly impacts the experience of the test subjects. The reason for the differentiation between small and large aircrafts is that the test subjects were recruited from the DLR staff. As a national research institution for aeronautics, a considerable number of hobby pilots has accumulated in the staff. This necessitates the separation between experiences in general aviation or commercial aviation settings. Furthermore, question number 15 "Are you under medical treatment [sic] or suffering affecting daily life.? [sic]" [19, p. 29] was deleted, as this was already asked in the initial email exchange with potential test subjects. Last but not least the questionnaire was translated to German for obvious reasons. The resulting questionnaire is given in Appendix C.

Griffin proposes to judge the answers to his motion sickness questionnaire via the following metrics [19], which are repeated for clarity. Due to the increased number of rows of the pre-flight questionnaire in contrast to the motion sickness history questionnaire, the metrics were adapted where necessary.

3.5.1.1 Travel Frequency in Past Year

Symbol: $T_{(yr.)}$
Formula:

$$T_{(yr.)} = \Sigma S_T \tag{3.46}$$

Description: The travel frequency in the past year, $T_{(yr.)}$ is determined from responses to Question 1. For each mode of transport, a "travel frequency score" (S_T) between 0 and 6 is assigned which depends on the column ticked (frequency of travel).

3.5.1.2 Illness Frequency while Traveling in the Past Year

Symbol: $I_{travel(yr.)}$
Formula:

$$I_{travel(yr.)} = \Sigma S_t \tag{3.47}$$

Description: Responses to Question 2 are used to determine the "illness frequency while traveling in the past year", $I_{travel(yr.)}$. For each mode of transport, an illness frequency

score (S_t) between 0 and 6 is assigned, depending on the column ticked (frequency of feeling ill).

3.5.1.3 Vomiting Frequency while Traveling in the Past Year

Symbol: $V_{travel(yr.)}$
Formula:

$$V_{travel(yr.)} = \Sigma S_V \tag{3.48}$$

Description: The responses to Question 3 are used to determine the "vomiting frequency while traveling in the past year", $V_{travel(yr.)}$. For each mode of transport, a vomiting frequency score (S_V) between 0 and 6 is assigned depending on the column ticked (frequency of vomiting).

3.5.1.4 Illness Susceptibility in Transport in the Past Year

Symbol: $I_{susc.(yr.)}$
Formula:

$$I_{susc.(yr.)} = \frac{\Sigma(S_I/S_T)}{N} \tag{3.49}$$

Description: Responses to Question 1 and 2 are used to determine the "illness susceptibility in transport in the past year", $I_{susc.(yr.)}$. For each mode of transport, the illness frequency scores (S_I) from Question 2 are divided by the travel frequency scores (S_T) from Question 1. Where N is the number of modes of transport in which respondents have traveled in the past. If respondents have not traveled in one of the modes of transport, scores for this mode are not included in the calculation of the mean. Possible values of $I_{susc.(yr.)}$ range from 0 to 1.67.

3.5.1.5 Total Susceptibility to Motion Sickness

Symbol: M_{total}
Formula:

$$M_{total} = \Sigma S_{hot} + \Sigma S_{head} + \Sigma S_{Pallor} + \Sigma S_{water} + \Sigma S_{drowsy} + \tag{3.50}$$

$$\Sigma S_{dizzy} + \Sigma S_{nausea} + \Sigma S_{vomit} + \Sigma S_{avoid} + \Sigma S_{self} \tag{3.51}$$

Description: Responses to Question 4 to 13 are used to determine the "total susceptibility to motion sickness", M_{total}. For each mode of transport, frequency scores are assigned for the frequency of *ever* experiencing each of eight symptoms. Frequency scores are also assigned for the avoidance due to motion sickness of each transport mode, S_{avoid} (Question 12) and to self-rated susceptibility to motion sickness, S_{self} (Question 13).

The pre-flight questionnaire was digitally distributed and collected in form of a Microsoft Word file to all pre-selected participants of the flight tests. In order to avoid any mistakes in manually reading the answers of the various participants, the filled out and collected Microsoft Word files were automatically parsed and processed using MATLAB®. The different metrics such as Travel frequency in past year $T_{(yr.)}$ or total suceptibility to motion sickness M_{total} could therefore also be automatically calculated directly from the digital files of the pre-flight questionnaires. This approach proved useful not only because of the time and effort saved for processing the questionnaires, but also because any human error in filling out the forms were caught. Faulty questionnaires could be easily identified and sent back to the test subjects for clarification. This approach improved the overall data quality.

3.5.2 Test Subject Selection and Pooling

Two test subjects were onboard of each flight of the flight tests, as described in Section 3.3. It is now perceivable that these two test subjects possess vastly different motion sickness susceptibility. In the worst case, one of the two test subjects could get severely motion sick and end the flight test, before the other test subject would feel significant levels of motion sickness which would diminish the "useful" flight time of the non-sick test subjects. As flight tests entail significant cost, such a situation should be avoided if possible.

For this reason it was decided to pool test subjects in pairs with similar motion sickness susceptibility. Each pair would then be assigned to the same test flight. It is important to note that no statistical dependency is created with this approach, as the assignation to the flights is still random. With the prerequisite of the aforementioned pre-flight questionnaire, the classification of motion sickness susceptibility of each test subject could be easily performed. For this task, the illness susceptibility in transport in the past year $I_{susc.(yr.)}$ was used. Based on the pre-flight questionnaire, an illness susceptibility $I_{susc.(yr.)}$ was computed for each test subject, then a list of ascending order was created.

From this list, pairs with similar $I_{susc.(yr.)}$ could be identified. In order to avoid statistical dependencies, the list of pairs itself was again randomly shuffled before each pair was assigned to a specific flight test.

3.5.3 In-flight Questionnaire

In order to be able to compare the results of the Griffin dataset with the test results of the flight tests, the same Griffin sickness scale described in Table 2.1 was used. For the flight tests, a corresponding questionnaire was designed which could be attached to the top of the knee via a so-called kneeboard. Every two minutes the pilot non-flying would give a signal over the intercom system, upon which the test subjects would indicate their respective motion sickness state on the questionnaire. The questionnaire contained four separate sheets, consisting of a cover sheet used for identifying the test subject and three sheets, each corresponding to one of the aforementioned ten-minute legs. On each sheet, a matrix is depicted, in which the columns correlate to the two minute intervals while the rows represent the Griffin motion sickness scale. The questionnaire is depicted in Fig. 3.11. It should be noted that some differences exist between the data acquisition performed during the flight test and that of the Griffin dataset. The test subjects contributing to the Griffin dataset had to indicate their motion sickness every minute [25,35,39–41]. As it was feared that shifting the concentration to the kneeboard and therefore away from the outside view could cause additional motion sickness, an interval of two minutes was chosen, which was deemed to be a good compromise. Another difference is that test subjects of the Griffin dataset were observed via a video camera and also asked to indicate which symptoms exactly led to their assessment. These measures could not be implemented for the flight tests, as it would have meant the installation of fixed hardware or prolonged focus on the kneepad.
After the flight test, the in-flight questionnaires were manually transferred to MATLAB® for the subsequent data analysis.

3.6 Data Acquisition

Another problem which needed to be solved was acquiring motion data of the helicopter during flight tests. First, the question arises: Which data has to be collected, and where does it have to be measured? The first part of this question is obvious: The intended purpose is to apply the improved Kamiji model as described in Section 2.3. As this model requires acceleration, attitude and rotational rates, these have to be measured.

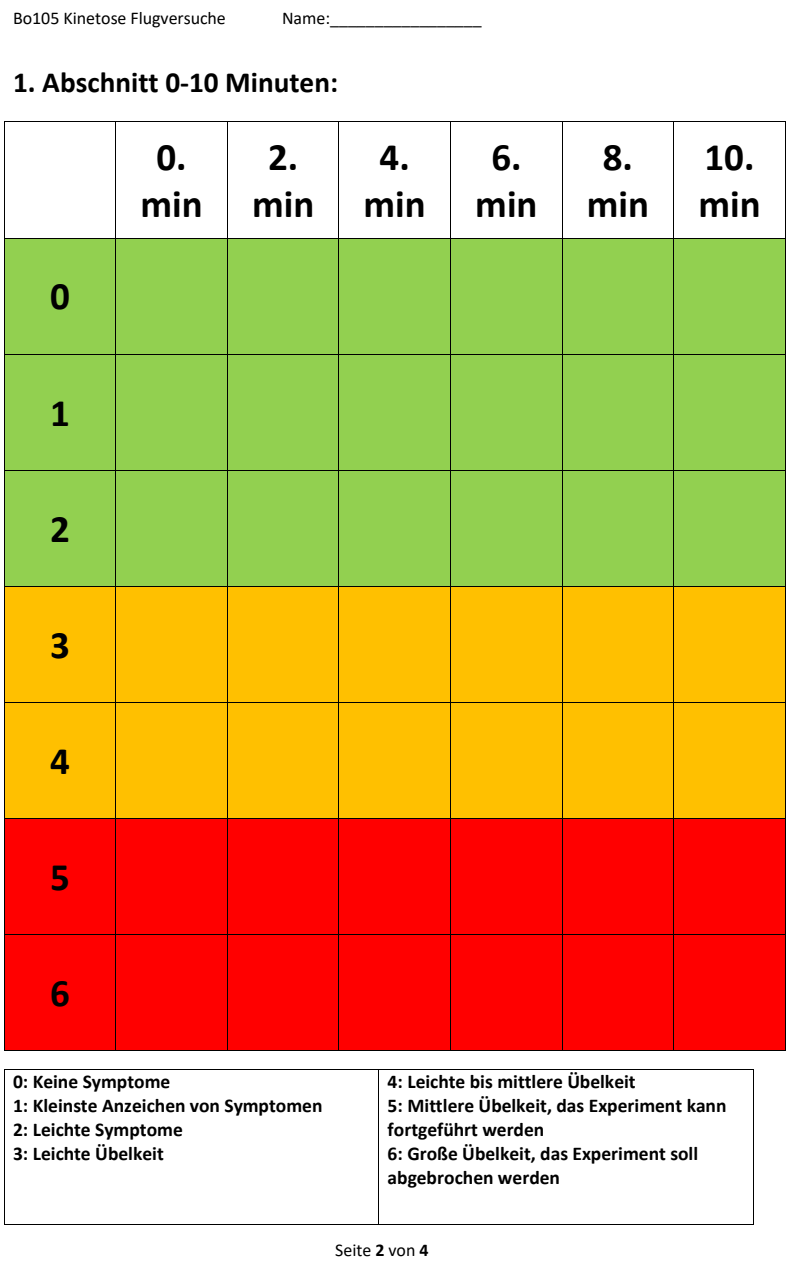

Bo105 Kinetose Flugversuche Name:_____

1. Abschnitt 0-10 Minuten:

	0. min	2. min	4. min	6. min	8. min	10. min
0						
1						
2						
3						
4						
5						
6						

0: Keine Symptome 1: Kleinste Anzeichen von Symptomen 2: Leichte Symptome 3: Leichte Übelkeit	4: Leichte bis mittlere Übelkeit 5: Mittlere Übelkeit, das Experiment kann fortgeführt werden 6: Große Übelkeit, das Experiment soll abgebrochen werden

Seite **2** von **4**

Figure 3.11: The in-flight questionnaire used in the flight tests

Concerning the measurement location, one can consults the ISO 2631 which states: "Vibration which is transmitted to the body shall be measured on the surface between the body and that surface." and further notes "Where direct measurements are not practicable, vibration may be measured at a rigid portion of the vehicle or building structure such as the center of rotation or the center of gravity." [16, 5.3.1, p. 4]. For vibrations involving health, comfort and perception in the frequency range of $0.5\,\mathrm{Hz}$ to $80\,\mathrm{Hz}$, the

ISO 2631 even specifies specific pick up locations, such as the seat surface or the surface upon which the occupant's feet are resting. For vibrations concerning motion sickness in the range of 0.1 to $0.5\,\mathrm{Hz}$, no guidance is given except for the definition of the motion sickness dose value as described in Section 2.1.1.1, which only states that the measurement direction is vertical [16, Table 1, p. 2].
While the ISO 2631 fails to mention the exact measurement locations for motion sickness measurements, it is clear that these lower frequency vibrations do not differ much depending on the measurement location in contrast to higher and/or structural vibrations. By taking into account Fig. 1.3 and a typical rotor frequency of $6.5\,\mathrm{Hz}$, it is evident that the main sources of vibrations relevant for motion sickness are the flight dynamics and the AFCS which are slow enough to justify a measurement location at or near the center of gravity.

Unfortunately, the Bölkow BO-105 helicopter of the DLR in contrast to many other DLR operated aircrafts is *not* equipped with a data recording system for basic flight dynamics data. Although the installation of a flight dynamics recording system for the BO-105 has been planned for many years, this system was not ready at the time of this experiment. For this reason, a different approach for recording this data had to be chosen. At the beginning of 2021, a new state-of-the-art Garmin G500H TXi digital multi-function display and avionics system was installed on the helicopter. This system measures and calculates the flight dynamic states of the aircraft digitally in order to be able to display these information to the pilot via the multi-function displays. Additionally, the requirements for a solution to extract this data from the avionics include no permanent installation of equipment onboard the helicopter in order to avoid extensive cost and time needed for certifying such modifications.

Several solutions were considered in order to extract these states, including installation of ARINC dataloggers or reading out the information over the encrypted Bluetooth protocol which is normally used to stream the flight dynamic state information to the proprietary Garmin Pilot™ app. After careful consideration, a hybrid approach of extracting and measuring the required data was adopted. The Garmin G500H TXi also supports the export of "maintenance" data onto a SD card *after* the flight [57, p. 2-38]. This function is mainly intended for recording engine parameters and indications but also records some flight instrument data which then could be used to monitor limit infringements of the helicopter. However, the data saved on the SD card does not contain all flight dynamics data. Additionally, the datastreams are only recorded at a rate of $1\,\mathrm{Hz}$, which unfortunately is much too low for using this data in motion sickness analysis. To overcome the limitations of the Garmin data recording, a second, lower-quality, cheap data recorder in the form of a portable smartphone was installed in a

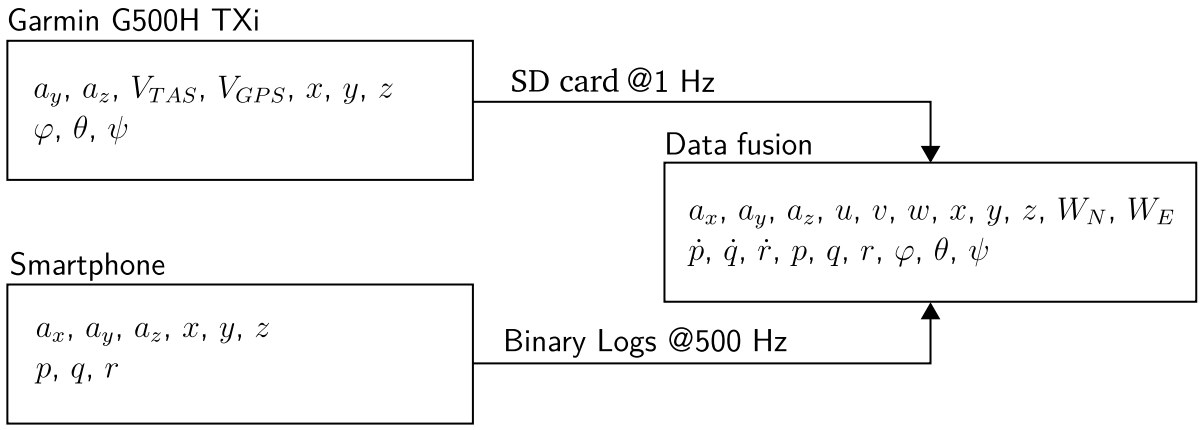

Figure 3.12: Flow diagram of the data fusion approach indicating data sample rate and types of data collected

non-permanent way inside the helicopter.
Both data sources were then combined by using a data fusion approach in post-processing, as sketched in Fig. 3.12. This method offers the unique advantage of combining the low-quality high-rate smartphone sensors with the high-quality low-rate Garmin avionics, but also delivers the full rotatory and translatory state of the rotorcraft, even those states which are not measured by either of the two sensors. While the data quality is not expected to match that of a dedicated experimental data recording device, it is expected to be good enough for the usage as a data basis for the evaluation of the motion sickness model presented in Section 2.3. The configurations of the Garmin avionics and the Smartphone device are described in Section 3.6.1 and 3.6.2. The subsequent data fusion approach is described in Section 3.7.

3.6.1 Garmin Avionics

As mentioned before, the BO-105 helicopter D-HDDP operated by the DLR in Brunswick is equipped with a Garmin G500H TXi helicopter touchscreen flight display. The installation features two 7” multi-function touchscreen displays configured as a Primary Flight Display (PFD) and two navigation and communication displays with 4.9” and 6.9” touchscreen displays. A photo of the cockpit installation is displayed in Fig. 3.13. Each PFD is connected to one of two Garmin GSU 75H combined air data and Attitude Heading Reference System (AHRS) units, one of two GMU 44 magnetometer units and one of two GTP 59 outside air temperature probes. This results in two strings of display systems with each string featuring its own set of instruments for data acquisition.
As mentioned before, several methods of extracting data from the avionic system were considered. The Garmin G500H TXi contains a "Flight Data Logging" functionality. Ac-

Figure 3.13: The Garmin G500H TXi of DLR's BO-105 registration sign D-HDDP

cording to the Pilot's Guide Handbook [57], amongst others, it contains the following features:

- Generates log files automatically upon unit power-up
- Records various parameters related to aircraft flight instruments, engine indications and configuration
- Writes logged data to an SD card if one is present in the top/left slot
- Saves files in the .csv format and stores them in the "data_log" folder

The data is saved internally in the unit until read out. It was extracted by inserting a suitable SD card into the appropriate SD card slot, and selecting the "Export Data Log" button on the touchscreen. This procedure was completed once after each flight test campaign.
The data was saved in .csv format with logging rate of $1\,\mathrm{Hz}$. These logs contain the (GPS) time, date, the latitude and longitude position, several altitude indications (altitude above mean sea level, barometric altitude, GPS altitude), outside air temperature, indicated airspeed, groundspeed, true airspeed, vertical speed, the attitude (roll, pitch, yaw), lateral and normal acceleration, magnetic variation and a couple of other datastreams. The relevant captured data is given by the measurement vector

$$\mathbf{z}_{BO} = \begin{pmatrix} a_y & a_z & V_{TAS} & V_{GPS} & x & y & z & \varphi & \theta & \psi \end{pmatrix} \tag{3.52}$$

with a_y and a_z being the accelerations, V_{TAS} and V_{GPS} denoting the true airspeed and the GPS speed (speed over ground), x, y and z being the position in a NED-frame and φ, θ and ψ being the Euler angles as defined in [58]. One peculiarity which should be noted is that the data does not contain longitudinal acceleration. Why the designers of this system decided to neglect this data field is unknown. This data was read in, converted to SI units if necessary and processed using MATLAB®. The resulting data was then used for the subsequent data fusion approach as described in Section 3.7.
Unfortunately, Garmin does not publish much information about the accuracy of this system. Upon inquiry, it became clear that such information could only be gained if a corresponding Non-disclosure Agreement (NDA) would be signed which of course would prohibit the publication in this thesis. However, some insights can be gained from the according certification of the Garmin GSU 75H AHRS: The root-mean-square error between a truth reference instrument and the Garmin unit in question multiplied by two shall not exceed the accuracy given in the certification document, in this case $2.5°$ [59, p. 29, 2.4.2.3.1.]. In other words, the attitude angles of this unit are more accurate then $\approx 1.25°$. Interestingly enough, the standard explicitly states that no specification on angular rates or linear accelerations is given in the document [59, p. 4, 1.5.3].[1]

3.6.2 Android Logging

It was decided to use a smartphone in order to support the data logging of the Garmin avionics unit. The idea of using a smartphone for data recording was conceived in order to overcome to main problems of the Garmin G500H TXi device: On the one hand the relative low data logging rate of only $1\,\mathrm{Hz}$, and on the other the incomplete sensor logging. Especially the fact that the Garmin avionics does not log *longitudinal* acceleration and also does not output rotational rates was regarded as critical, as the motion sickness model introduced in Section 2.3 relies on these measurements. Therefore, the smartphone was installed to support the Garmin G500H TXi with high-rate data, and also to deliver additional sensor sources for the subsequent data fusion. An overview of the resulting datastream and quantities logged by the different devices is shown in Fig. 3.12.

[1] The GSU 75H unit is certified under the CS-ETSO [60, p. 590] which states that the minimum performance standard is set forth in the RTCA/DO-334 "Minimum Operational Performance Standards (MOPS) for Solid-State Strap-Down Attitude and Heading Reference Systems (AHRS)" [59]. The installation manual of the GSU specifies that the unit adheres to the category A4 [61, Table 1-6] which states that in flight conditions the unit is more accurate then $2.5°$.

Concerning the logging hardware, several alternatives were considered including purchasing commercially available devices or building a data logging device from scratch by using a suitable single-board computer or a single-board microcontroller and coupling it with a suitable IMU, battery and user interface. In the end, this approach was dropped in favor of using a commercially available smartphone as the smartphone already offers all of these functionalities. Additionally, it was feared that if a data recorder was built and coupled to a battery, safety concerns might arise due to the risks of using such a homebuilt device in a helicopter. However, any concerns regarding carrying such a device on a helicopter flight can be discarded by using a smartphone, as practically all pilots and passengers already carry smartphones during the flights anyways. Therefore, it can be argued that it is widely accepted practice for people to carry these personal electronic devices on helicopter flights. Additionally, if the smartphone for whatever reason actually poses a threat, it can still be discarded by simply throwing it out of the window. While no concerns or discussions ever arose before or during the flight test upon the use of the smartphone as a recording device, such an argument was considered to be a valuable asset.

The installation itself was performed using a textile rubber band as shown in Fig. 3.14a, which contained a sewed-on pocket in order to hold the smartphone in place. In this way the smartphone could be installed non-permanently, again in order to avoid any certification efforts. The middle seat was chosen for this purpose as this spot was as close to the center of gravity as possible. The textile rubber band could be adjusted in length so that it would fit optimally around the seat cushion. The cushion was mounted itself via a hook-and-loop fastener (or velcro tape) to the wooden seat substructure bolted to the airframe.

As a software platform, Google's Android Operating System (Android OS) was chosen, a Linux based operating system primarily designed for mobile devices. A custom application running on this system was developed using the Java programming language and Android studio, an integrated development environment supplied by Google and itself based on the IntelliJ IDEA platform. The editor supports the programming, graphical layout and the deployment of an application for a mobile device equipped with Android OS. The application itself performs the following tasks:

- Supplies a graphical user interface for naming and starting/stopping logs
- Launches a separate foreground task which reads relevant sensor data installed on the smartphone
  - Accelerometer

  - Gyroscope
  - GPS position

- Writes all relevant sensors data to a binary log file at the highest available rate onto the internal memory of the smartphone
- Ensures continued, uninterrupted logging, regardless of the underlying operating system state, especially in regard to the power saving mode

Also listed as a sensor is the "orientation sensor", which outputs the attitude of the smartphone. However, trials indicated that this "sensor" delivers implausible or false data. Due to the available back-up in form of the Garmin avionics, the smartphone orientation sensor was therefore neglected for the data fusion approach.
The relevant captured data is given by the measurement vector

$$\mathbf{z}_{SM} = \begin{pmatrix} a_x & a_y & a_z & x & y & z & p & q & r \end{pmatrix} \tag{3.53}$$

again with a_x, a_y and a_z being the accelerations, x, y and z being the position in a NED-frame and p, q and r being the rotational rates of the body frame as defined in [58].

The Android OS and also software installed by the manufacturers of the smartphone try to ensure that the smartphone is as power efficient as possible. If these software elements however decide that an application is not used or needed at the moment, the application in question gets paused or terminated. Of course, a logging application is only useful if it runs uninterrupted, therefore special care was given to ensure continued and uninterrupted logging of the sensor data. The developed logging application implements a so-called "Foreground service", which according to the Android developer documentation, alerts the user of the ongoing resource consumption and therefore is allowed to run indefinitely [62]. However, during deployment on several smartphones it was found that software installed by some manufacturers is more aggressive in pausing or terminating applications than others. As this software installed by the manufacturer cannot be uninstalled, the easiest way to circumvent these restrictions was to force the application to always run with turned-on screen. As a result, the application is always deemed to be critical, as it continuously displays information to the user. However, if the on/off button of the smartphone is pressed, the screen would turn off which sooner or later would pause or terminate the logging application. In order to physically hinder unintentional pressing of the on/off button, a 3D printed cage made out of PETG plastic was installed around the smartphone during flight, which physically shielded the on/off button. The cage was designed such that the display could still be seen in order to confirm the state of the logging, yet it could be easily installed by snapping it onto the

Table 3.3: Selected specifications of the smartphone IMU TDK/INVESENSE ICM-42632-M MEMS IMU

Characteristic	Value	Unit
Accelerometer		
Range	± 8	g
Output RMS noise	0.7	$\mathrm{mg-RMS}$
Resolution	0.24	mg
Nonlinearity	± 0.1	$\%\mathrm{FS}$
Gyroscope		
Range	1000	$^\circ/\mathrm{s}$
Output noise	0.038	$^\circ/\mathrm{s-RMS}$
Resolution	0.03	$^\circ/\mathrm{s}$
Nonlinearity	± 0.1	$\%\mathrm{FS}$

smartphone. The smartphone with the cage installed and the logging software running is displayed in Fig. 3.14b.

The smartphone was selected to be a Samung Galaxy S20 FE model featuring a Qualcomm Snapdragon 865 Octo-core processor with a clock rate of up to $2.73\,\mathrm{GHz}$, six Gigabytes of RAM and $128\,\mathrm{Gb}$ of internal memory as well as a 6.5" display which is regarded to be a medium to high-end smartphone. The built-in gyroscope/accelerometer sensor is a TDK/InvenSense ICM-42632-M IMU featuring triple-axis MEMS gyroscope and accelerometer. The detailed specifications of this unit are listed in Table 3.3. The logged sensor data was stored in the internal memory of the smartphone. In order to reduce the size of a log, it was stored as a binary file in a custom format which resulted in a data rate of around $231\,\mathrm{Mb/h}$. The developed application together with the chosen smartphone hardware achieved a logging rate of $500\,\mathrm{Hz}$ for data measured by the gyroscope and accelerometer. GPS position data was recorded at $1\,\mathrm{Hz}$. The binary logs were read in and processed using MATLAB®. The resulting data was then used for the subsequent data fusion approach as described in Section 3.7.

3.7 Data Processing and Flight Path Reconstruction

The acquired data from the flight test consists on the one hand of the Garmin G500H TXi data log files and on the other hand of the data collected by the smartphone, also stored as log files. In order to enable the subsequent data analysis, both log files of each flight test had to be fused into one continuous datastream. The goal of this process is to fuse the measurement vectors of the Garmin G500H TXi Eq. (3.52) and the smartphone

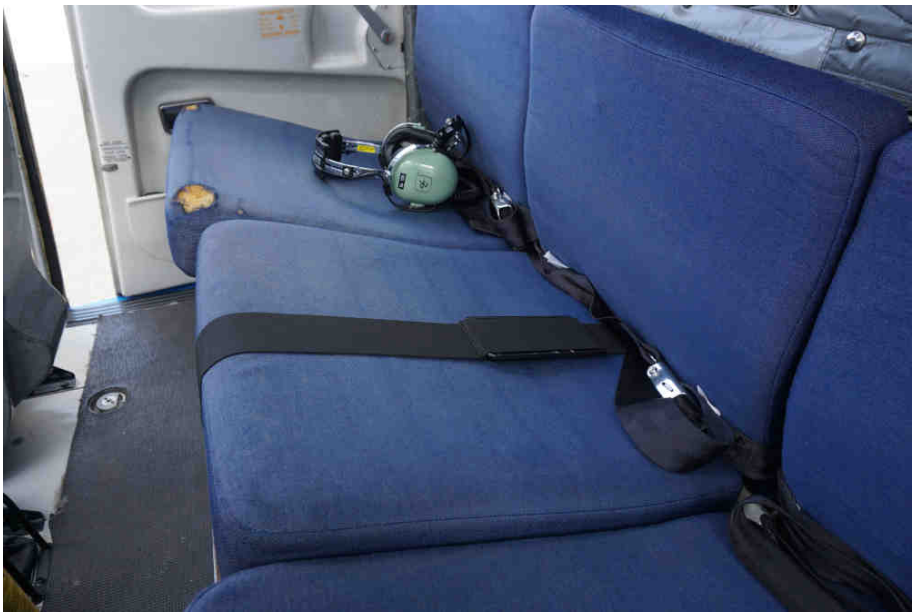

(a) Installation using a textile rubber band in the middle of the three back seats

(b) Smartphone measuring device with protective 3D printed cage

Figure 3.14: Hardware setup of the smartphone measuring device

Eq. (3.53) and at the same time estimate unkown states, such that one continuous data vector

$$\mathbf{x}_{fused} = \begin{matrix}(a_x & a_y & a_z & u & v & w & x & y & z & W_N & W_E \\ \dot{p} & \dot{q} & \dot{r} & p & q & r & \varphi & \theta & \psi)^T\end{matrix} \tag{3.54}$$

as sketched in Fig. 3.12 results.
The overall data analysis of each flight consists of several parts: The log files of the smartphone and the Garmin G500H TXi are read-in and preprocessed, which includes conversion to SI units and transformation of the smartphone specific coordinate frame to the aerospace frame of reference. Then data section of interest is selected, which shall mainly exclude non-relevant stretches of times at the beginning and end of the log files. After this part, the two logs are aligned in time via cross correlating the vertical acceleration a_z present in both logs, which will be further described in Section 3.7.1. Additionally, a uniformly sampled universal time vector is generated, which serves as a basis for the later unscented Kalman filter (UKF). Furthermore, the installation angle of the smartphone data was accounted for, which will be described in greater detail Section 3.7.2. As a last step before the data fusion can take place, the measurement vectors are inflated with empty values in case of the Garmin data, while the smartphone data is downsampled and low-pass filtered with a cutoff frequency of $50\,\mathrm{Hz}$ such that both datastreams featured a sample rate of $100\,Hz$. Both these steps are performed such that the resulting measurement vectors match the size of the generated universal time vector .

3.7.1 Cross-Correlation

An important preliminary step for the subsequent data fusion is the time alignment of the two sensor data streams from the smartphone and the Garmin G500H TXi avionics. Because both data recordings are started independently, the two datastreams exhibit different starting times. Naturally, the time difference of the data recordings has to be known, only then can the data fusion work in a meaningful manner. Therefore, this step is an important prerequisite for the data fusion.
If every datastream which shall be aligned includes a GPS time signal, intuitively it is clear that these datastreams can be accurately aligned in time using this very accurate GPS time signal. Unfortunately, the developed Android application presented in Section 3.6.2 was not designed with this technique in mind, and does not time-stamp its logged data with GPS time, but rather with system time, which cannot be converted to GPS time.

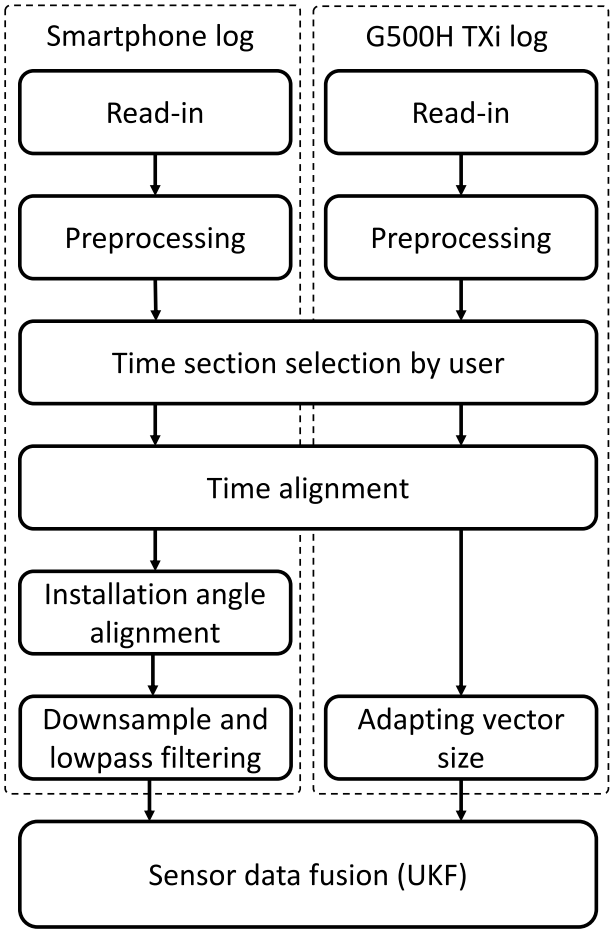

Figure 3.15: Flow graph of the performed data fusion, in order to combine data acquired by smartphone and Garmin G500H TXi logs

An alternative is the time alignment of two signals using their cross-correlation. This approach hinges on the assumption that two signals $x(t)$ and $y(t)$ are exact copies of one another, however shifted in time by some unknown time constant Δt [63]. The cross-correlation R_{xy} of the two signals can now be computed via

$$Rc_{xy}(\Delta t) = \int_{-\infty}^{\infty} x(t)y(t + \Delta t)dt. \tag{3.55}$$

For two discrete time signals $x[k]$ and $y[k]$ with a separation of n, the cross-correlation function is defined as [64, p. 401]:

$$Rc_{xy}(n) = \sum_{k=-\infty}^{k=\infty} x[k]y[k + n]. \tag{3.56}$$

By searching for the peak in the resulting cross-correlation function Rc_{xy}, the most likely time delay Δt (or discrete time delay n) can be identified.
For the task of identifying the time shift between the smartphone data and that of the Garmin G500H TXi avionic, the vertical acceleration signal a_z which is measured by both systems was chosen, because it contained enough signal energy for a reliable fit. An example of the two signals taken from flight 3 is displayed in Fig. 3.16. In this Figure, the vertical acceleration for the complete flight is displayed, whereby the abscissa was chosen to be the time sample index k, as opposed to the absolute time in seconds, in order to keep consistent with the formula presented in Eq. (3.56). It should be furthermore noted that the vertical acceleration signal of the Garmin G500H TXi was interpolated in order to achieve a sampling rate of $100\,\mathrm{Hz}$ while the vertical acceleration signal of the smartphone was downsampled to $100\,\mathrm{Hz}$. This is necessary to enable the comparability of both signals via the cross-correlation of the two.

Two facts are immediately evident in Fig. 3.16: On the one hand, the smartphone acceleration signal is considerably more noisy than that of the Garmin avionics. This is an inherent effect of the mounting and the quality of the smartphone sensors, and should emphasize that this is indeed a *low*-quality high-rate sensor. Despite these deficiencies, the cross-correlation shown in Fig. 3.16b displays a clear and unique peak, therefore enabling the easy identification of the discrete time delay n.
This time delay was then applied to all signals of the smartphone in preparation of the data fusion.

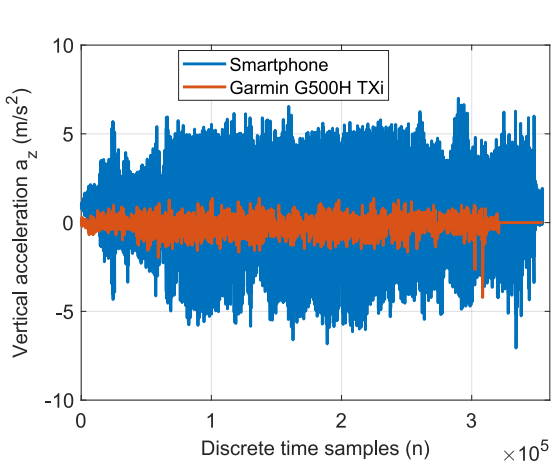

(a) The two unaligned vertical acceleration discrete-time signals

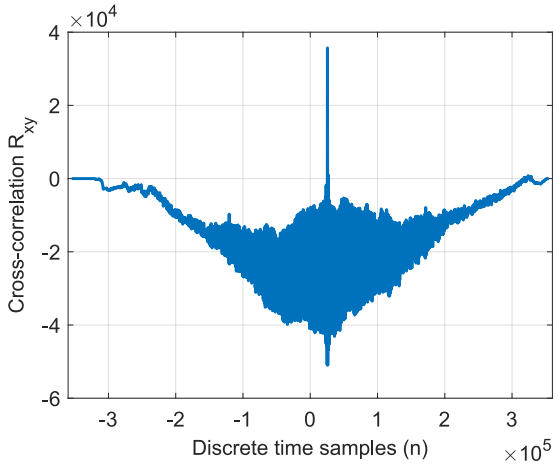

(b) Discrete cross-correlation $Rc_{xy}(n)$ of the two signals

Figure 3.16: Cross-correlation of the vertical acceleration measured by the smartphone and the Garmin G500H TXi both sampled at $100\,\mathrm{Hz}$. Data taken from flight 3

3.7.2 Smartphone Installation Angle Correction

When installed in its textile rubber band on top of the middle seat of the BO-105 helicopter, the smartphone was slightly inclined as can be clearly seen in Fig. 3.14a. Because the rotational rates p, q and r as well as the inertial accelerations a_x, a_y and a_z are measured in the body frame of the smartphone, a counterrotation of this installation angle was performed in order to augment the accuracy of the data acquired by the smartphone. As the Garmin G500H TXi avionic system was installed such that its frame of reference would be level when the helicopter stands on the ground, the compensation of the smartphone installation angles transforms the measurements into the same frame of reference.

The installation angle was determined via the gravity vector as measured by the smartphone shortly after it was installed in its textile rubber band, but before the helicopter took off. This ensured a steady and clean acceleration signal, from which the installation pitch angle $\theta_{installation}$ and roll angle $\varphi_{installation}$ could be estimated. Both angles are estimated by averaging the acceleration signals over the aforementioned time span and computing the angles via

$$\theta_{installation} = \arcsin\left(\bar{a}_x\right) \tag{3.57}$$

$$\varphi_{installation} = \arctan\left(\frac{\bar{a}_y}{-\bar{a}_z}\right) \tag{3.58}$$

whereby $\bar{a}_x$, $\bar{a}_y$ and $\bar{a}_z$ denote the mean accelerations in the respective axis. An overview of the installation angles determined via this method throughout the different flights is

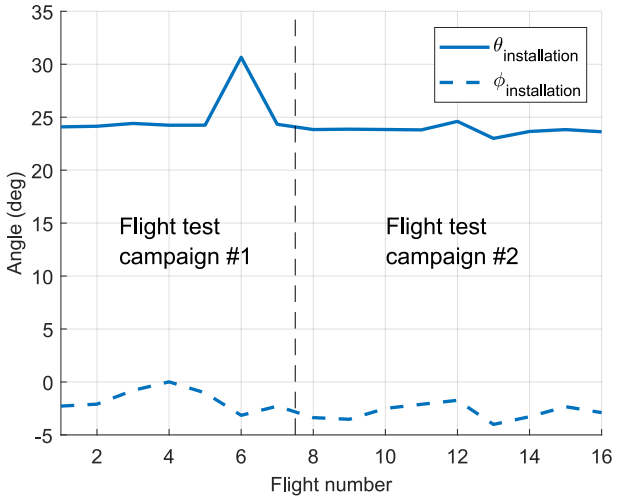

Figure 3.17: Installation angles of the smartphone over the different flight tests

given in Fig. 3.17.

After the installation angle was determined, the rotational rates and translational accelerations could be rotated via the well-known rotation matrices for the case of a 3D vector

$$\begin{pmatrix} p \\ q \\ r \end{pmatrix}_{B} = \mathbf{R}_{BB'} \cdot \begin{pmatrix} p \\ q \\ r \end{pmatrix}_{B'} \tag{3.59}$$

in order to transform the rotational rates p, q and r from the canted reference frame B' to the body frame B. The rotation matrix $\mathbf{R}_{BB'}$ for euler angles is defined as [58, p. 6, 1.2.2]:

$$\mathbf{R}_{BB'} = \begin{pmatrix} \cos\psi & -\sin\psi & 0 \\ \sin\psi & \cos\psi & 0 \\ 0 & 0 & 1 \end{pmatrix} \begin{pmatrix} \cos\theta & 0 & \sin\theta \\ 0 & 1 & 0 \\ -\sin\theta & 0 & \cos\theta \end{pmatrix} \begin{pmatrix} 1 & 0 & 0 \\ 0 & \cos\varphi & -\sin\varphi \\ 0 & \sin\varphi & \cos\varphi \end{pmatrix}. \tag{3.60}$$

Note that this method cannot estimate any yaw installation angle. Therefore, in order to obtain meaningful data from the smartphone, a consistent yaw orientation had to be ensured by accurate installation of the smartphone inside the textile rubber band. As shown in Fig. 3.17, $\theta_{installation}$ and $\varphi_{installation}$ are relatively consistent throughout the different flights, it is therefore assumed that the same holds true for the yaw angle.

3.7.3 Kalman Filter

The central algorithm for fusing the measurements of the Garmin G500H TXi and the smartphone is the Kalman filter. Originally proposed by Rudolf E. Kálmán in 1960 [65],

this filter represents a mathematical approach in which uncertain measurements are used in order to estimate the states of a dynamic system iteratively. Two assumptions are central to the filter:

- The state vector, measurements, noise of the process etc., can be modeled as normally (Gaussian) distributed random variables
- The mathematical model of the underlying dynamic system is explicitly incorporated

If the statistical parameters of the measurement and process noise are known (and normally distributed), the Kalman filter optimally reduces the errors of the estimated states [65].
These features make the Kalman filter a very widely-used and popular filter algorithm especially in the controls community. Applications cover diverse diverse topics such as the classical estimation problem of tracking an object, perhaps best illustrated by the Apollo space mission in which the midcourse navigation was realized on basis of a Kalman filter [66], over applications in economics [67] in which these filters are applied to foresee certain financial parameters up to sensor fusion applications in which multiple streams of sensor data are fused [68].

3.7.3.1 Linear Kalman Filter

Consider the case of discrete time, in which the time increments in fixed steps Δt uniquely identified by an integer k. As a shorthand notation, the k-th time step will be denoted in the following for all subsequent variables with the subscript $\ldots_k$. In the case of the discrete time vector, this results in the notation $t[k] = t_k = t_0 + k \cdot \Delta t$ with $k = 0, 1, 2, \ldots$.
The process which shall be observed in the case of the *linear* Kalman filter is given by the *linear* difference equation

$$\mathbf{x}_k = \mathbf{F}_{k-1}\mathbf{x}_{k-1} + \mathbf{B}_{k-1}\mathbf{u}_{k-1} + \mathbf{w}_{k-1} \tag{3.61}$$

with **x** being the state vector, **F** the *linear* state transformation matrix, describing the transformation of the state vector between to timesteps, **B** the input matrix, **u** the input and **w** being the process noise which introduces a random variable to the dynamic system. The addition of the random variable **w** is an important step, as it accounts for modeling errors and disturbances of the dynamic system. This, and all other stochastic

variables of the linear case, are modeled as a normally distributed variable with a mean of zero in the shorthand notation

$$\mathbf{w}_{k-1} \sim \mathcal{N}(\mathbf{0}, \mathbf{Q}_{k-1}) \tag{3.62}$$

and $\mathbf{Q}_{k-1}$ being the according process noise covariance matrix. Thus, the transition from the previous state $\mathbf{x}_{k-1}$ to the current state $\mathbf{x}_k$ is affected by the random variable $\mathbf{w}_{k-1}$. We also assume that the observation of this process can be described by a stochastic process. The dynamic system is observed via some measurement $\mathbf{z}$ at time step k. The measurement can be described by

$$\mathbf{z}_k = \mathbf{H}_k \mathbf{x}_k + \mathbf{v}_k \tag{3.63}$$

with the observation matrix $\mathbf{H}$ indicating which linear combinations of the system state are measured. The measurement underlies the stochastic Gaussian distributed measurement noise

$$\mathbf{v}_k \sim \mathcal{N}(\mathbf{0}, \mathbf{R}_k) \tag{3.64}$$

with $\mathbf{R}_k$ denoting the covariance matrix of the measurement noise.

For the following, let $\hat{\mathbf{x}}_{k|l}$ be the estimate of $\mathbf{x}_k$ with data observed up to and including time step l whereby $l \leq k$.
The Kalman filter estimates two quantities: The system state $\hat{\mathbf{x}}_{k|k}$ and the according estimation error covariance matrix $\mathbf{P}_{k|k}$. It does so by iteratively executing two distinct steps: First the a priori **prediction step**,

$$\hat{\mathbf{x}}_{k|k-1} = \mathbf{F}_{k-1} \hat{\mathbf{x}}_{k-1|k-1} + \mathbf{B}_{k-1} \mathbf{u}_{k-1} \tag{3.65}$$

$$\mathbf{P}_{k|k-1} = \mathbf{F}_{k-1} \mathbf{P}_{k-1|k-1} \mathbf{F}_{k-1}^T + \mathbf{Q}_{k-1} \tag{3.66}$$

which simply extrapolates the system state and error covariance matrix to the next time step by using the system dynamics.
The **measurement update step** incorporates measurement data into the estimates

$$\mathbf{K}_k = \mathbf{P}_{k|k-1} \mathbf{H}_k^{\mathrm{T}} \left(\mathbf{H}_k \mathbf{P}_{k|k-1} \mathbf{H}_k^T + \mathbf{R}_k \right)^{-1} \tag{3.67}$$

$$\hat{\mathbf{x}}_{k|k} = \hat{\mathbf{x}}_{k|k-1} + \mathbf{K}_k \left(\mathbf{z}_k - \mathbf{H}_k \hat{\mathbf{x}}_{k|k-1} \right) \tag{3.68}$$

$$\mathbf{P}_{k|k} = \left(\mathbf{I} - \mathbf{K}_k \mathbf{H}_k \right) \mathbf{P}_{k|k-1} \tag{3.69}$$

whereby $\mathbf{K}_k$ is frequently called the *Kalman gain* or *Kalman matrix*.

3.7.3.2 Unscented Kalman filter

The linear Kalman filter can give poor results or be unstable for some nonlinear systems. In order to address this, the unscented Kalman filter (UKF) was proposed by S. Julier and J. Uhlmann [69], which uses an *unscented transform* in order to approximate the mean and covariance of a probability distribution. Additionally, it is not necessary to calculate Jacobian or Hessian matrices for this algorithm which further eases the computation. This approach results in approximations that are accurate to the third order (Taylor series expansion) for Gaussian inputs for all nonlinearities. For non-Gaussian inputs, approximations are accurate to at least the second order [69,70]. In order to further increase numerical stability and efficiency, a Square-Root unscented Kalman filter (SR-UKF) was implemented as described in [70], which uses a Cholesky factorization. However, in this text the SR-UKF and the normal UKF will not be further discriminated as it is not relevant for the use other than the specific implementation.

One application of the unscented Kalman filter is the implementation of such a filter in the ACT/FHS helicopter (see Fig. 3.4b) developed and maintained by the author of this dissertation. The filter uses various sensor sources such as an INS, several pitot tubes, the experimental nose boom of the aircraft and one or several GPS-units in order to not only give an estimate of the current flight-dynamic states but also to estimate such variables as the current windspeed and bias parameters of the pitot tubes. This implementation proved to be very valuable as it is easy to incorporate changed hardware features e.g. if certain sensors are changed or are temporarily unavailable [68].

In contrast to the linear Kalman filter presented before, the unscented Kalman filter uses a nonlinear model of the dynamic system

$$\mathbf{x}_k = \mathbf{f}(\mathbf{x}_{k-1}, \mathbf{u}_{k-1}, \mathbf{w}_{k-1}, k) \tag{3.70}$$

$$\mathbf{z}_k = \mathbf{h}(\mathbf{x}_k, \mathbf{u}_k, k) + \mathbf{v}_k \tag{3.71}$$

again with $\mathbf{w}_{k-1} \sim \mathcal{N}(\mathbf{0}, \mathbf{Q}_{k-1})$ and $\mathbf{v}_k \sim \mathcal{N}(\mathbf{0}, \mathbf{R}_k)$. In contrast to the linear case, it is here assumed that both the system dynamics $\mathbf{f}(\cdot)$ as well as the measurement function $\mathbf{h}(\cdot)$ are nonlinear and time varying.

The underlying problem, is that of propagating a random variable x through a nonlinear function f in order to obtain a second random variable y

$$y = f(x) \tag{3.72}$$

and being able to state the mean and the probability distribution of y. In the linear case, this transformation and the thereby resulting mean and covariance can be trivially calculated. The linear Kalman filter hinges on this principle, which makes the derivation

and formulation of the Kalman filter equations relatively straight forward.
However, in the nonlinear case, it is not possible to give a general solution to the same problem. For this reason, the unscented Kalman filter *approximates* the resulting probability density function with the help of sigma points [69]. The idea is to encode the exact shape of a probability distribution by a limited number of sigma points. A 2D example, taken with adaption from [71], which compares a large set of sampled points to sigma points is displayed in Fig. 3.18. In this Figure, both sets of points are transformed by a nonlinear function, whereby the resulting mean and covariance of the transformation can be reasonably represented by the much lower number of sigma points.

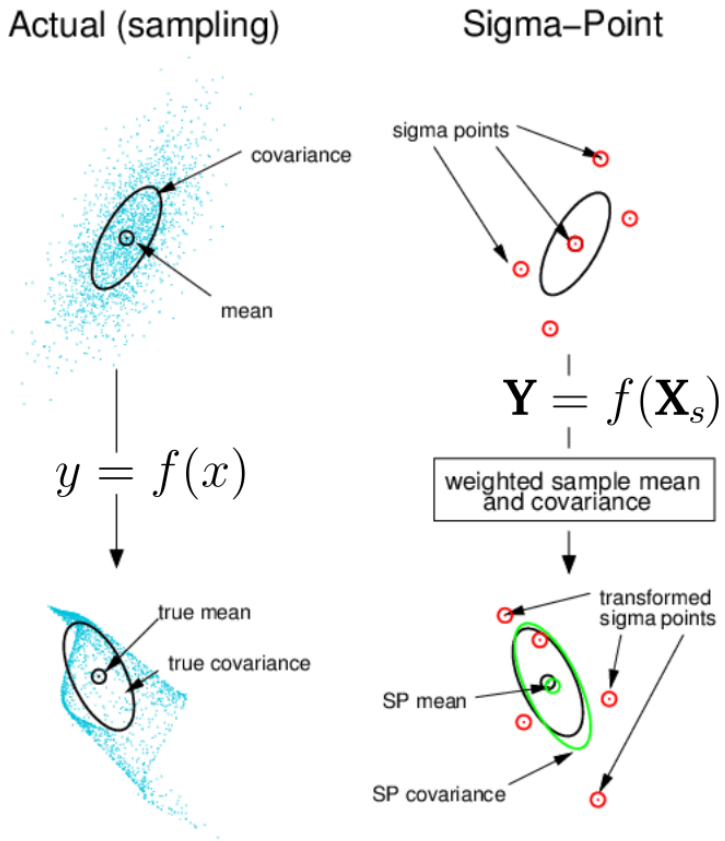

Figure 3.18: 2D example of sigma points approximating a probability density function, taken with adaption from [71]

Just as in the linear case, the UKF performs two steps: First, a prediction step in which the next state and error covariance are predicted, and second a correction step which incorporates the performed measurement into these estimations.

Prediction step

In order to facilitate the following calculations, first weights used for the calculation of

the mean ($\mathbf{w}_m$) and the covariance ($\mathbf{W}_c$) are defined by

$$w_m^1 = \frac{a^2(n+k)-n}{a^2(n+k)} \tag{3.73}$$

$$w_c^1 = \frac{a^2(n+k)-n}{a^2(n+k)} + 1 + b - a^2 \tag{3.74}$$

$$w_m^i = w_c^i = \frac{1}{2a^2(n+k)}, \qquad i = 2, \ldots, 2n+1 \tag{3.75}$$

with $a = 10^{-3}$, $b = 2$, $k = 3 - n$ and $d = a\sqrt{n+k}$ [70, 72]. By grouping the weights

$$\mathbf{w}_m = \begin{bmatrix} w_m^1 & \ldots & w_m^{2n+1} \end{bmatrix}^T \tag{3.76}$$

$$\mathbf{W}_c = \begin{bmatrix} w_c^1 & & \\ & \ddots & \\ & & w_c^{2n+1} \end{bmatrix} \tag{3.77}$$

the application of these weights e.g. in Eq. (3.81) is a bit easier.

The unscented Kalman filter algorithm itself, begins with sampling 2n + 1 sigma points around the last system state estimate $\hat{\mathbf{x}}_{k-1|k-1}$

$$\hat{\mathbf{X}}_{s,k-1|k-1} = \underline{\hat{\mathbf{X}}}_{k-1|k-1} + d\begin{pmatrix} \mathbf{0} & \sqrt{\mathbf{P}_{k-1|k-1}} & -\sqrt{\mathbf{P}_{k-1|k-1}} \end{pmatrix}, \qquad \hat{\mathbf{X}}_{s,k-1|k-1} \in \mathbb{R}^{n,2n+1} \tag{3.78}$$

with a column of zeros $\mathbf{0} \in \mathbb{R}^{n,1}$ and $\sqrt{\mathbf{P}_{k-1}} \in \mathbb{R}^{n,n}$. The matrix

$$\underline{\hat{\mathbf{X}}}_{k-1|k-1} = \begin{pmatrix} \hat{\mathbf{x}}_{k-1|k-1} & \cdots & \hat{\mathbf{x}}_{k-1|k-1} \end{pmatrix}, \qquad \underline{\hat{\mathbf{X}}}_{k-1|k-1} \in \mathbb{R}^{n,2n+1} \tag{3.79}$$

consists of $2n + 1$ columns of the last system state estimation, such that the matrix dimensions of $\hat{\mathbf{X}}_{s,k-1|k-1}$ are matched. The notation of an underlined capital letter $\underline{\square}$ to denote the arrangement of a vector into a matrix as shown in Eq. (3.79) will be repeatedly used in the following.

After the generation, the sigma points are propagated column by column through the nonlinear system dynamics function

$$\hat{\mathbf{X}}_{k|k-1} = \mathbf{f}(\mathbf{X}_{s,k-1|k-1}, \mathbf{u}_{k-1}) \tag{3.80}$$

in order to acquire the transformed sigma points. Note that the input $\mathbf{w}_{k-1}$ and k of Eq. (3.70) are neglected in Eq. (3.80) for brevity. The prediction step is then concluded by weighting Eq. (3.80) to acquire the predicted state

$$\hat{\mathbf{x}}_{k|k-1} = \hat{\mathbf{X}}_{k|k-1}\mathbf{w}_m \tag{3.81}$$

and the predicted covariance matrix

$$\mathbf{P}_{k|k-1} = \left(\hat{\mathbf{X}}_{k|k-1} - \underline{\hat{\mathbf{X}}}_{k|k-1}\right) \mathbf{W}_c \left(\hat{\mathbf{X}}_{k|k-1} - \underline{\hat{\mathbf{X}}}_{k|k-1}\right)^T + \mathbf{Q}_{k-1} \tag{3.82}$$

based on the propagated sigma points [69, 72]. Note that the matrix $\underline{\hat{\mathbf{X}}}_{k|k-1}$ is constructed from the predicted state $\hat{\mathbf{x}}_{k|k-1}$ similarly to Eq. (3.79).

Measurement update step

As in the linear case of the Kalman filter, the second step of the unscented Kalman filter is the update of predicted mean and predicted covariance matrix of Eqs. (3.81) and (3.82) with the measurements [70, 72]. First, a new set of sigma points is instantiated based on the predicted mean $\hat{\mathbf{x}}_{k|k-1}$ arranged in the matrix $\underline{\hat{\mathbf{X}}}_{k|k-1}$ analogously to Eq. (3.79)

$$\hat{\mathbf{X}}_{s,k|k-1} = \underline{\hat{\mathbf{X}}}_{k|k-1} + d \begin{pmatrix} \mathbf{0} & \sqrt{\mathbf{P}_{k|k-1}} & -\sqrt{\mathbf{P}_{k|k-1}} \end{pmatrix}. \tag{3.83}$$

These are then, column by column, projected through the nonlinear observation function

$$\hat{\mathbf{Z}}_{k|k-1} = \mathbf{h}(\hat{\mathbf{X}}_{s,k|k-1}) \tag{3.84}$$

and weighted

$$\hat{\mathbf{z}}_{k|k-1} = \hat{\mathbf{Z}}_{k|k-1} \mathbf{w}_m \tag{3.85}$$

which yields the predicted measurement vector. The predicted measurement covariance $\mathbf{S}_k$ can be computed by

$$\mathbf{S}_k = \left(\hat{\mathbf{Z}}_{k|k-1} - \underline{\hat{\mathbf{Z}}}_{k|k-1}\right) \mathbf{W}_c \left(\hat{\mathbf{Z}}_{k|k-1} - \underline{\hat{\mathbf{Z}}}_{k|k-1}\right)^T + \mathbf{R}_k \tag{3.86}$$

again with the predicted measurements $\hat{\mathbf{z}}_{k|k-1}$ arranged into a matrix $\underline{\hat{\mathbf{Z}}}_{k|k-1}$ as seen in Eq. (3.79). The Kalman filter gain is obtained by

$$\mathbf{K}_k = \left(\hat{\mathbf{X}}_{k|k-1} - \underline{\hat{\mathbf{X}}}_{k|k-1}\right) \mathbf{W}_c \left(\hat{\mathbf{X}}_{k|k-1} - \underline{\hat{\mathbf{X}}}_{k|k-1}\right)^T \mathbf{S}_k^{-1} \tag{3.87}$$

which is then used to finally compute the updated state vector estimate $\hat{\mathbf{x}}_{k|k}$ and covariance matrix $\mathbf{P}_{k|k}$ via

$$\hat{\mathbf{x}}_{k|k} = \hat{\mathbf{X}}_{k|k-1} + \mathbf{K}_k(\mathbf{z}_k - \hat{\mathbf{z}}_{k|k-1}) \tag{3.88}$$

$$\mathbf{P}_{k|k} = \mathbf{P}_{k|k-1} - \mathbf{K}_k \mathbf{S}_k \mathbf{K}_k^T. \tag{3.89}$$

3.7.3.3 Kalman Smoother

In addition to the Kalman filter, an Unscented Rauch-Tung-Striebel Kalman Smoother (URTSS) is implemented as proposed in [73]. The idea of a Kalman smoother is to increase the quality of the state variable estimation $\hat{\mathbf{x}}_{k|k}$ *a-posteriori* by using the fact that in offline applications, measurement data is not only available up to and including time-step k, but also for future time-steps. In fact, for Kalman smoothers it is generally assumed that the entirety of the data can be accessed from the first to the last time-step. Naturally, this approach does not work for online estimation of data.
The Unscented Rauch-Tung-Striebel Kalman Smoother works by going backwards over the estimated state variable $\hat{\mathbf{x}}_{k|k}$ and covariance matrix $\mathbf{P}_{k|k}$, starting at the last time-step $k = T$ and iteratively computing *smoothed* estimates of these variables *backwards* in time until $k = 0$. Therefore, the URTSS recursively updates the the smoothed covariance $\mathbf{P}_k^s$ and smoothed state mean $\hat{\mathbf{x}}_k^s$ at time-step k, based on the smoothed covariance $\mathbf{P}_{k+1}^s$ and state mean $\hat{\mathbf{x}}_{k+1}^s$ at time-step $k+1$. The corresponding algorithm is given in Eqs. (3.90) to (3.97). One big advantage of the URTSS is that it offers good performance without the need to compute the time inverse dynamics of the system, which obviously facilitates the application of this smoother.

As a first step, analogous to Eqs. (3.78) and (3.80), sigma points are generated

$$\mathbf{X}_{s,k|k} = \underline{\hat{\mathbf{X}}}_{k|k} + d\begin{pmatrix}\mathbf{0} & \sqrt{\mathbf{P}_{k|k}} & -\sqrt{\mathbf{P}_{k|k}}\end{pmatrix}, \qquad \mathbf{X}_{s,k|k} \in \mathbb{R}^{n,2n+1} \tag{3.90}$$

again with $\underline{\hat{\mathbf{X}}}_{k|k}$ being the matrix arrangement of the state vector estimate $\hat{\mathbf{x}}_{k|k}$. As before, the sigma pointsare then propagated through the nonlinear system dynamics function

$$\hat{\mathbf{X}}_{k+1|k} = \mathbf{f}(\mathbf{X}_{s,k|k}, \mathbf{u}_k) \tag{3.91}$$

whereby the propagation is again performed column by column. Note that no time inverse nonlinear dynamics function is needed.
As a second step, the predicted mean $\hat{\mathbf{x}}_{k+1|k}$, the predicted covariance $\mathbf{P}_{k+1|k}$ and the cross-covariance $\mathbf{C}_{k+1}$ are calculated

$$\hat{\mathbf{x}}_{k+1|k} = \hat{\mathbf{X}}_{k+1|k}\mathbf{w}_m \tag{3.92}$$

$$\mathbf{P}_{k+1|k} = \left(\hat{\mathbf{X}}_{k+1|k} - \underline{\hat{\mathbf{X}}}_{k+1|k}\right)\mathbf{W}_c\left(\hat{\mathbf{X}}_{k+1|k} - \underline{\hat{\mathbf{X}}}_{k+1|k}\right)^T + \mathbf{Q}_k \tag{3.93}$$

$$\mathbf{C}_{k+1} = \left(\mathbf{X}_{s,k|k} - \underline{\hat{\mathbf{X}}}_{k|k}\right)\mathbf{W}_c\left(\hat{\mathbf{X}}_{k+1|k} - \underline{\hat{\mathbf{X}}}_{k+1|k}\right)^T \tag{3.94}$$

again with $\underline{\hat{\mathbf{X}}}_{k+1|k}$ and $\underline{\hat{\mathbf{X}}}_{k|k}$ being the matrix arranged vectors $\hat{\mathbf{x}}_{k+1|k}$ respectively $\hat{\mathbf{x}}_{k|k}$. Note that Eqs. (3.90) to (3.93) are in principle no different than Eqs. (3.78) to (3.82).

The parameters d, $\mathbf{W}_c$ and $\mathbf{w}_m$ are the same as described in the UKF chapter 3.7.3.2, Eqs. (3.73) to (3.77).
As a final step, the smoother gain $\mathbf{D}_k$ and the smoothed state estimation $\hat{\mathbf{x}}_k^s$ and smoothed covariance matrix $\mathbf{P}_k^s$ are calculated via

$$\mathbf{D}_k = \mathbf{C}_{k+1}\mathbf{P}_{k+1|k}^{-1} \tag{3.95}$$

$$\hat{\mathbf{x}}_k^s = \hat{\mathbf{x}}_{k|k} + \mathbf{D}_k\left(\hat{\mathbf{x}}_{k+1}^s - \hat{\mathbf{x}}_{k+1|k}\right) \tag{3.96}$$

$$\mathbf{P}_k^s = \mathbf{P}_k + \mathbf{D}_k\left(\mathbf{P}_{k+1}^s - \mathbf{P}_{k+1|k}\right)\mathbf{D}_k^T. \tag{3.97}$$

This concludes the backward iteration step, which begins at time-step $k = T$ and ends at the beginning $k = 0$ [73]. Note that for the computation of the smoothing step, it is beneficial to save the prediction step results of the UKF Eqs. (3.78) to (3.82) such that they can be reused for the computation of the URTSS.

3.7.3.4 Equations of Motion

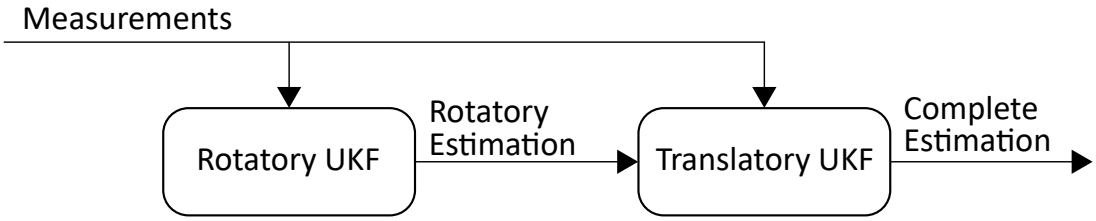

Figure 3.19: Overall filter structure

A prerequisite for using the UKF is the need for a dynamic model of the system. In the context of this work, it was decided to estimate a total of 20 flight dynamic states, based on the six-degrees-of-freedom rigid-body dynamics. The filter is further subdivided into two unscented Kalman filters. First, the rotational estimation is performed, which is then used to perform the translational estimation as depicted in Fig. 3.19. The reason such a division is possible is that for the purpose of filtering, it is assumed that the translational and rotational accelerations are zero

$$a_x = a_y = a_z = \dot{p} = \dot{q} = \dot{r} = 0 \tag{3.98}$$

which corresponds to a steady unaccelerated flight condition. This assumption is fairly common for a flight path reconstruction algorithm [72], as it does not require any specific knowledge or mathematical models about the aircraft for which the filter is designed. It should be noted that in reality, the aircraft of course does *not* always fly without acceleration. However, Kalman filtering can account for this via process noise Eq. (3.62), which was included exactly for this purpose as it (amongst others) accounts

for unmodeled dynamics. Therefore, by using the assumption of Eq. (3.98) the control engineer leans on the capability of the Kalman filter to capture unmodeled dynamics of the vehicle.
For the usage with the UKF of Section 3.7.3.2, the system dynamics as given in Eqs. (3.70) and (3.71) have to be defined. Note that in the following, the system dynamics and measurement dynamics are stated in time-continuous form, however for the later implementation these were (if necessary) discretized.
For the rotational case, the state vector and system dynamics are given by

$$\mathbf{x}_{rot} = \begin{pmatrix} \dot{p} & \dot{q} & \dot{r} & p & q & r & \varphi & \theta & \psi \end{pmatrix}^T \tag{3.99}$$

$$\mathbf{f}_{rot} = \begin{pmatrix} 0 \\ 0 \\ 0 \\ \dot{p} \\ \dot{q} \\ \dot{r} \\ p + q\sin(\varphi)\tan(\theta) + r\cos(\varphi)\tan(\theta) \\ q\cos(\varphi) - r\sin(\varphi) \\ q\sin(\varphi)\sec(\theta) + r\cos(\varphi)\sec(\theta) \end{pmatrix} \tag{3.100}$$

[72, 74]. The observation function depends on the measurements taken. In this case, the measurements are given by the rotational parts of Eq. (3.52) and Eq. (3.53). These can be compiled to form

$$\mathbf{H}_{rot} = \begin{pmatrix} p & q & r & \varphi & \theta & \psi \end{pmatrix}^T \tag{3.101}$$

whereby the rotational rates (p, q and r) are measured by the smartphone, while the Euler angles (φ, θ and ψ) are measured by the Garmin G500H TXi.

Similarly, the continuous system for the translational case is defined by

$$\mathbf{x}_{trans} = \begin{pmatrix} a_x & a_y & a_z & u & v & w & x & y & z & W_N & W_E \end{pmatrix}^T \tag{3.102}$$

$$\mathbf{f}_{trans} = \begin{pmatrix} 0 \\ 0 \\ 0 \\ a_x - q \cdot w + r \cdot v - g \cdot \sin(\theta) \\ a_y - r \cdot u + p \cdot w + g \cdot \sin(\varphi)\cos(\theta) \\ a_z - p \cdot v + q \cdot u + g \cdot \cos(\varphi)\cos(\theta) \\ \mathbf{R}_{EB} \cdot \begin{pmatrix} u \\ v \\ w \end{pmatrix} - \begin{pmatrix} W_N \\ W_E \\ 0 \end{pmatrix} \\ 0 \\ 0 \end{pmatrix} \tag{3.103}$$

with $\mathbf{R}_{EB}$ denoting the rotation matrix from the body to the NED frame [58]. These dynamics represent a standard six-degrees-of-freedom model [72,74]. The translational parts of Eqs. (3.52) and (3.53) are assembled to form the measurement function

$$\mathbf{H}_{trans} = \begin{pmatrix} a_y \\ a_z \\ \left\| \begin{pmatrix} u & v & w \end{pmatrix}^T - \mathbf{R}_{BE} \begin{pmatrix} W_N & W_E & 0 \end{pmatrix}^T \right\|_2 \\ \left\| \begin{pmatrix} u & v & w \end{pmatrix}^T \right\|_2 \\ x \\ y \\ z \\ a_x \\ a_y \\ a_z \\ x \\ y \\ z \end{pmatrix} \tag{3.104}$$

whereby the terms $V_{TAS} = \left\| \begin{pmatrix} u & v & w \end{pmatrix} \right\|_2$ for true airspeed and $\mathbf{v}_{GPS} = \begin{pmatrix} u & v & w \end{pmatrix}^T - \mathbf{R}_{BE} \begin{pmatrix} W_N & W_E & 0 \end{pmatrix}^T$ for the GPS speed (groundspeed) are used. For the computation of the UKF, these are written as a function of the states $\mathbf{x}_{trans}$ of the translational system [72,74]. Additionally, $\mathbf{R}_{BE}$ is the rotation matrix from NED frame to body frame of the vehicle [58].

3.7.3.5 Implementation

The implementation was performed in MATLAB®. Large parts of the UKF and URTSS implementation were taken from [72]. The system dynamics stated in Eqs. (3.99) to (3.104) are discretized with the chosen sample rate of $t_{sample} = 100\,\mathrm{Hz}$. It should be noted that not all measurements were available at each time step due to the different sample rates. As described in Section 3.6, the Garmin G500H TXi system delivered new data only with $1\,\mathrm{Hz}$, therefore only every 100th sample, while the data measured by the Android smartphone was recorded at $500\,\mathrm{Hz}$ and then downsampled to $100\,\mathrm{Hz}$. However, the dynamic structure of the UKF allows the dynamic assembly of the measurement functions $\mathbf{H}_{rot}$ and $\mathbf{H}_{trans}$, therefore, if any of the measurements displayed in these two functions is not available at a particular instance, these measurements are left out in the recursive step for that time-step.

Furthermore, the implementation was performed using a more efficient square-root unscented Kalman filter implementation as proposed by [70]. In this approach, instead of propagating the covariance matrix directly, the matrix square root $\mathbf{S}\mathbf{S}^T = \mathbf{P}$ is propagated instead, which offers higher numerical stability at less computational cost. Hereby, linear algebra techniques such as QR-decomposition and the Cholesky factorization and factor update are leveraged. The interested reader is referred to [70] for the exact algorithm. However, it should be noted that the SR-UKF does not alter the main idea of the UKF but changes the way the UKF is implemented in software.

3.7.3.6 Results

One of the primary reasons for the used approach of fusing smartphone and avionics measurements, is that the Garmin avionics measurements alone do not offer a high enough sampling frequency. The idea of the data fusion approach was therefore to support these measurements with low-quality but high-rate data from the smartphone. The result of this strategy is very nicely illustrated in Fig. 3.20 which depicts the roll angle and velocity of flight 3, tasked with performing oscillations at $0.1\,\mathrm{Hz}$. The relatively sparse $1\,\mathrm{Hz}$ sampling of the Garmin G500H TXi avionics is marked as a red line with crosses. Clearly seen can be the fact that it undersamples the underlying sinusoidal oscillation. On the other hand the data measured by the smartphone, marked in blue, does not offer a direct measurement of the roll angle but only data for the rotational velocity. Additionally, the smartphone data also contains a lot of noise which is also very well visible in Fig. 3.20. However, with these two information sources, the UKF estimation drawn in black is capable of estimating an interpolated signal of the roll angle φ

which captures the underlying oscillation better than the original roll angle data of the Garmin G500H TXi. The roll velocity estimation of p is much smoother and obviously contains less high-frequency noise than the original smartphone measurements, partly due to the low-pass filtering of the Android sensor data. Noteworthy is the difference between the original measurement of the roll angle φ and the estimation of the UKF, which at times exceeds the inaccuracy of the Garmin G500H TXI of $1.25°$ as described in Section 3.6.1. Such differences are not surprising given that a majority of the data stems from the relatively inaccurate and noisy smartphone. Additional error sources of the data could also be the mounting of the smartphone to the seat: While care was given to obtain a tight fit, it cannot be fully ruled out that the smartphone recorded minor movements during flight due to the temporary mounting with the help of a textile rubber band, resulting in false measurement signals which in turn would impact the data quality of the UKF results.

The second interesting plot showing the performance of the UKF is depicted in Fig. 3.21. This plot shows the vertical acceleration signal a_z measured by the smartphone in blue, measured by the Garmin G500H TXi in red and the resulting UKF estimation of this variable in black. Clearly visible again is the relatively high noise of the smartphone sensor which, however in the trend agrees well with the signals measured by the Garmin G500H TXi. Overall, the UKF estimation appears to be much smoother and more filtered then the two input signals.
Last but not least, an interesting side note is the performed wind estimation displayed in Fig. 3.22. For this plot, the difference between the groundspeed and true airspeed as measured by the Garmin G500H TXi was plotted over the heading flown at the time of measurement, which can be interpreted as the *measured* wind. The average of this signal also serves as the initial wind guess, marked in red in Fig. 3.22. The estimation of the UKF is displayed in black. It can be seen that the prevalent wind is low, reaching only an amplitude of $3\,\mathrm{m/s}$, which is also confirmed by Table B.4 in which the wind as reported by the pilots is stated (Wind at start/landing (groundlevel)). These plots are extracts from data gathered during flight 3. A complete overview of the time-series of this flight is given in Appendix D.

Overall, it is concluded that while the UKF estimation does have some drawbacks partly due to the deficiencies of the measurement setup such as imperfect mounting and high noise of the smartphone or the low sample frequency of the Garmin avionics, the approach yields comparatively good data. While it is expected that a dedicated experimental measurement system would offer better data quality, it is concluded that for the purpose of this study the resulting data is more than sufficient and therefore can be accepted.

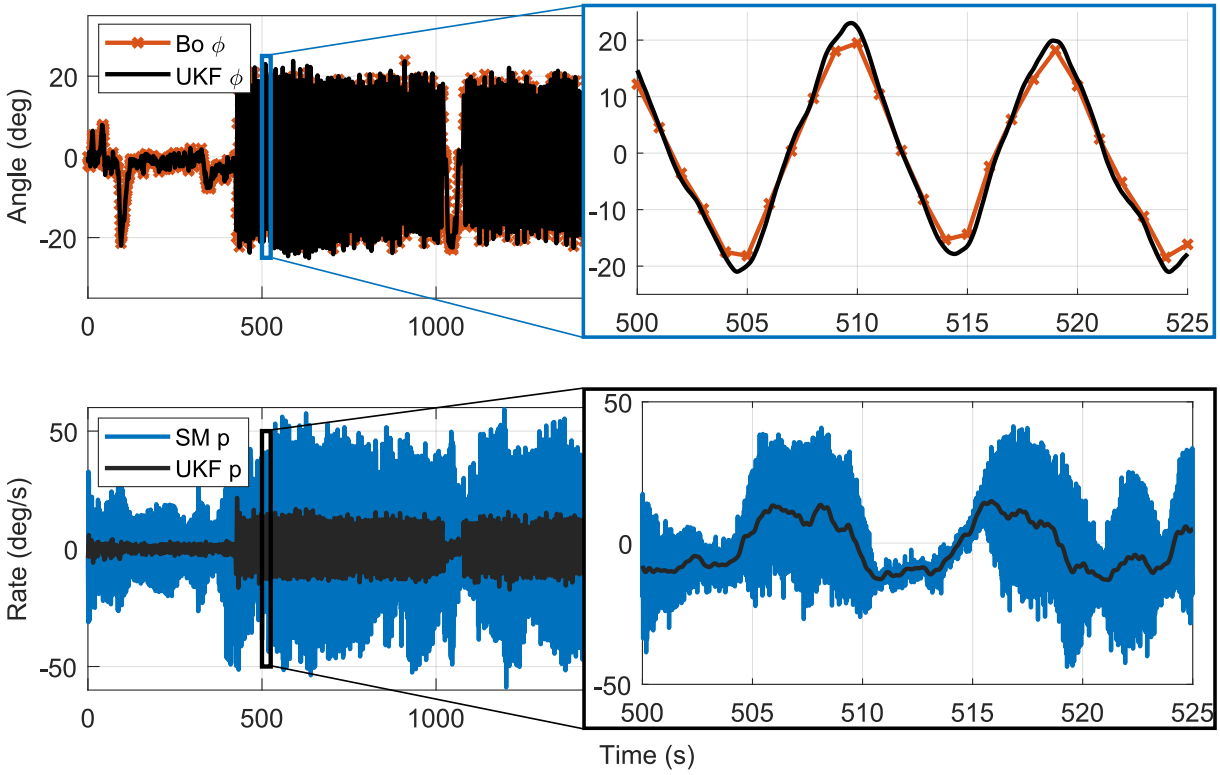

Figure 3.20: Measured and estimated roll angle and velocity of flight 3. Smartphone measurements in blue, G500H TXi measurement data in red, UKF estimation data in black

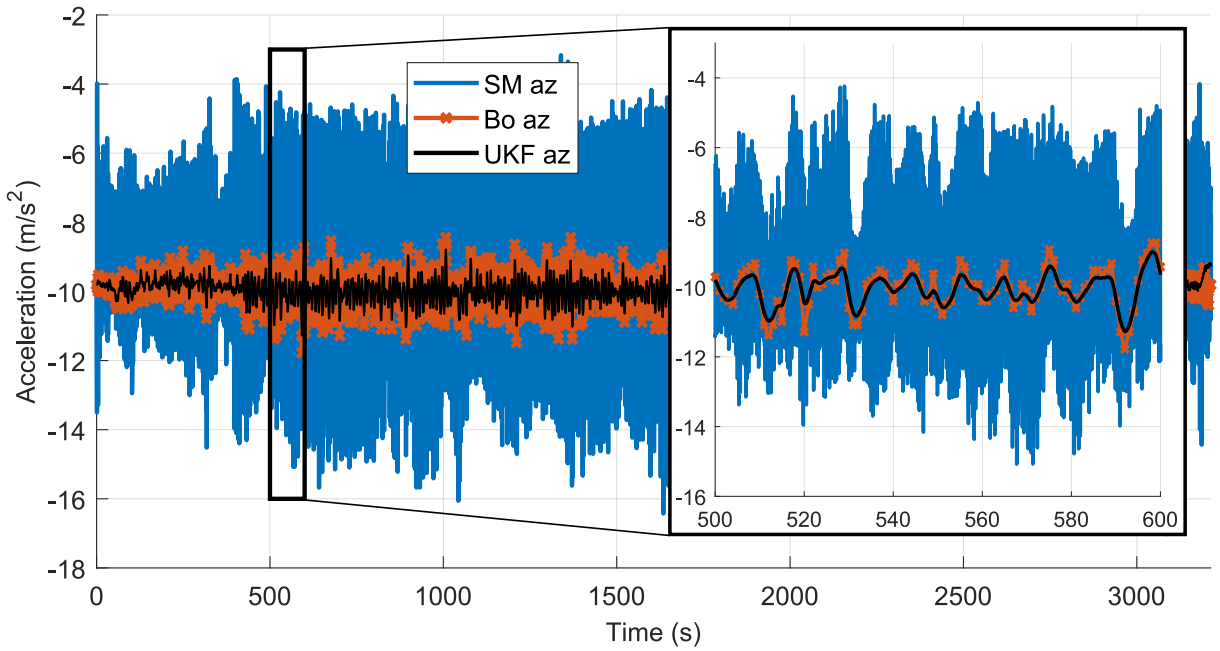

Figure 3.21: Measured and estimated vertical acceleration in body frame of flight 3. Smartphone measurements in blue, G500H TXi measurement data in red, UKF estimation data in black

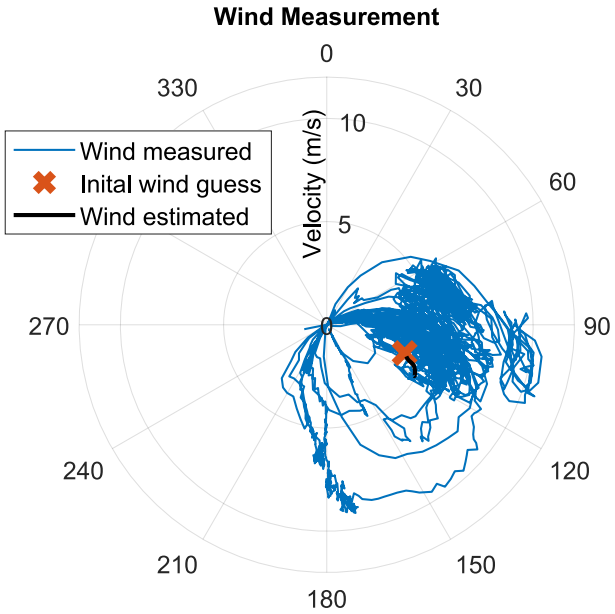

Figure 3.22: Polar plot of wind estimation of flight 3. Difference of groundspeed and true airspeed over heading in blue, wind estimation of UKF in black

4 Flight Test Results and Analysis

As stated in Chapter 3, the flight tests were performed in order to generate a motion sickness dataset for general use and to validate the motion sickness model developed in Chapter 2. The obtained results of these flight tests will be presented and subsequently analyzed in this chapter. Note that parts of the statistical analysis are taken from [18], who ran statistical tests as part of her master thesis in support of this project.
The chapter is structured as follows: First the statistical methods used in this work will be presented, followed by the evaluation of the flight tests with respect to flight conditions, performance of the auditive cueing system, general analysis of the test subjects and finally the evaluation of motion sickness during the test flights. After this a comparison between the motion sickness levels observed during flight and the motion sickness levels as predicted by the improved Kamiji model described in Section 2.3 is presented.

4.1 Methods for the Statistical Analysis

The performed flight tests were analyzed partly with the help of statistical analysis tools which will be presented in the following. For clarity, the definition of some basic statistical terminology as defined in [75] will be repeated in the following list:

1. Population: A set of items or events for which a statistical analysis shall be performed. In the case of this thesis, the population is defined to be adult humans of mixed gender with no specific origin.

2. Sample: A selected subset of the population, e.g. a random group of people who are used to represent the population.

3. Observation: The measured property or quantity of interest of one individual e.g. the measured motion sickness of one test subject.

4.1.1 Mann-Whitney U test

The Mann-Whitney U Test is a non-parametric test used to test if *two* samples originate from one single population and therefore represent a subset of this population, or if the samples are drawn from different populations. For this objective, a null hypothesis H_0 is formulated which is then either confirmed or rejected. The null hypothesis denotes the assumption that the differences between the drawn samples result coincidentally and do not indicate a statistical significant difference. Therefore, if the null hypothesis is confirmed, we conclude that the samples do not differ in a statistical significant way and that the samples therefore originate from the same underlying population. Vice versa if the null hypothesis is rejected, we concluded that there *is* a statistical significant difference hence the underlying population from which the samples originate are different [76, 77].

Instead of comparing absolute numbers, the Mann-Whitney U test compares the *ranks* of exactly **two** samples each containing several observations. The observations from both samples are pooled and then ranked based on the value which the specific observation possesses. If several observations share the same value (also called ties), the same rank is assigned. The different ranks are denoted by the variable R_{ij} whereby the subscript i denotes the *i-th* sample and j the *j-th* observation. After this step, the sum of ranks

$$R_i = \sum_{j=1}^{n_i} R_{ij} \tag{4.105}$$

is calculated for both samples (R_1 and R_2), with n_i the size of the sample. Now the U-values are calculated by comparing the sum of ranks to their expected values

$$U_1 = n_1 \cdot n_2 + \frac{n_1 \cdot (n_1 + 1)}{2} - R_1 \tag{4.106}$$

$$U_2 = n_1 \cdot n_2 + \frac{n_2 \cdot (n_2 + 1)}{2} - R_2. \tag{4.107}$$

After chosing the minimum of both U-values

$$U = min(U_1, U_2), \tag{4.108}$$

the expected value and standard error

$$\mu_U = \frac{n_1 \cdot n_2}{2} \tag{4.109}$$

$$\sigma_U = \sqrt{\frac{n_1 \cdot n_2 \cdot (n_1 + n_2 + 1)}{12}} \tag{4.110}$$

can be calculated. If shared ranks exist, an alternative calculation for the standard error

$$\sigma_U = \sqrt{\frac{n_1 \cdot n_2}{n \cdot (n-1)}} \cdot \sqrt{\frac{n^3 - n}{12} - \sum_{l=1}^{m} \frac{t_l^3 - t_l}{12}} \tag{4.111}$$

has to be used, whereby m is the number of tied ranks and t_l the number of values sharing the rank l and n the total number of observations $n = n_1 + n_2$.

$$Finallythez - valueorstandardscorez = \frac{U - \mu_U}{\sigma_U} \tag{4.112}$$

can be calculated which indicates the number of standard deviation this value deviates from the mean value of the probability distribution [78, p. 114].

4.1.2 Kruskal-Wallis test

For large parts of the statistic data analysis, the Kruskal-Wallis test was used. In contrast to their their parametric counterpart, the non-parametric Kruskal-Wallis test is employed if the data which shall be analyzed is not Gaussian distributed. This test assumes however that samples are random and independent and that the probability distribution of these is of the same shape. The test can be interpreted to be a generalization of the Mann-Whitney U test for several groups of data [76, 77]. In contrast to the Mann-Whitney U Test, the Kruskall-Wallis test confirms or rejects the null hypothesis H_0 for n_i samples ($n_i > 2$).

Instead of comparing absolute numbers, the Kruskal-Wallis assigns ranks to the observations of the different samples from smallest to largest observation. Therefore, the observations from all samples are pooled and then ranked based on the value which the specific observation possesses. The assigned rank is again denoted as R_{ij} whereby the subscript $_i$ denotes the *i-th* sample and the subscript $_j$ denotes the *j-th* observation. If several observations share the same value (also called ties), the same rank is assigned. After this step, the sum of ranks

$$R_i = \sum_{j=1}^{n_i} R_{ij} \tag{4.113}$$

is calculated for each sample, with n_i denoting the size of the sample. In difference to the approach of the Mann-Whitney U test, now the test statistic H is calculated

$$H = \frac{12}{n(n+1)} \sum_{i=1}^{k} \frac{R_i^2}{n_i} - 3(n+1) \tag{4.114}$$

whereby total number of observations is denoted by $n = n_1 + n_2 + \ldots + n_k$ and k the number of samples. If there are tied ranks, the modified equation

$$H_{ties} = H \cdot \left(1 - \frac{\sum_{l=1}^{m}(t_l^3 - t_l)}{n^3 - n}\right)^{-1} \tag{4.115}$$

has to be used, whereby m is the number of tied ranks and t_l the number of values sharing the rank j [18, 77].

The resulting test statistic H or H_{ties} can be used in order to verify if the medians of the samples differ in a statistical significant way. For this, the calculated test statistic is compared to a threshold value, whereby the null hypothesis is rejected on the right-hand tail of the chi-square distribution also used by similar statistical tests [76]. This threshold $H_{crit}(\alpha, df)$ is a function of the significance level α and the degrees of freedom defined as $df = k - 1$ and can be found in tables in the respective literature sources [78].

The significance level α indicates the confidence level upon which the null hypothesis is accepted. For example if the significance level is chosen to be 5% it means that the null hypothesis is correctly accepted with a confidence level of 95%. Typical values for the significance value α are 1% or 5%, however in the context of this work and given the relatively small sample sizes, a significance level of $\alpha = 5\%$ is chosen.

When using statistical tests like the Mann-Whitney U test or the Kruskal-Wallis test, the so-called p-value is often used. The p-value is the smallest level of significance that would lead to rejection of the null hypothesis H_0 with the given data [78][p. 294]. In other words, under the assumption that the null hypothesis is correct, the p-value denotes the probability of observing test results at least as extreme as actually observed during the tests. The p-value can therefore be directly compared to the significance level. The explicitly stated cases are:

1. $p \leq \alpha$: The null hypothesis is rejected - statistical significant differences between the different samples are present.
2. $p > \alpha$: The null hypothesis is accepted - there are no statistical significant differences between the different samples.

4.1.3 Boxplots

Another widespread tool for visualizing the distribution of statistical data are boxplotes. These types of graphs offer a good visual representation of the median, mean, outliers

and general distribution of a given statistical sample.
The boxplots used in this thesis show the median, the upper and lower quartile, upper and lower whiskers and outliers as shown in Fig. 4.1. In some instances, the mean is also added in the form of a red diamond. Whiskers have a maximum length of 1.5 times the interquartile distance, therefore the distance between the upper and lower quartile. If values lie outside of this area, they are denoted as outliers [18, 77].

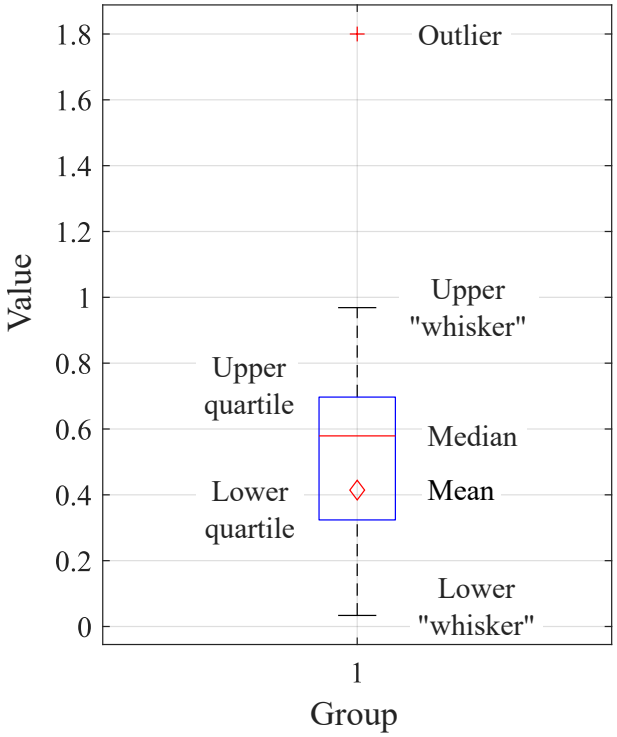

Figure 4.1: Exemplary boxplot with description from [18, 77]

4.2 Statistical Evaluation of Flight Experiments

In this chapter, the flight conditions, performance of the auditive cueing system, the response of the test subjects in general and with respect to motion sickness will be statistically analyzed.

4.2.1 Flight Conditions

In contrast to simulator tests, motion profiles generated by flight vehicles are affected by the general meterological conditions. For this reason a higher variance in the motion generation of flight tests is present. Additionally, the tests conducted during this study

were piloted manually and therefore underlie an even greater variance. For this reason some preliminary analysis has to be carried out in order to show that the performed flight tests were conducted under similar conditions.

In order to confirm that the general flight dynamics conditions were comparable throughout all flight tests, some key motion parameters were analyzed in comparison to the oscillation frequency which was flown. For this, each flight was divided into three segments whereby each segment contained one of the 10-minutes legs in which the test subject motion sickness response has been measured. For each of these legs, some flight parameters were extracted and pooled in order to obtain a statistical dataset. These variables were then visualized in correlation to the three nominal frequencies flown during the flight tests in order to show that the flight tests were performed under similar conditions. Some results of this correlation can be seen in Fig. 4.2. For example, it is visible that the spread of the true airspeed shown in Fig. 4.2 is comparable for all three frequencies.

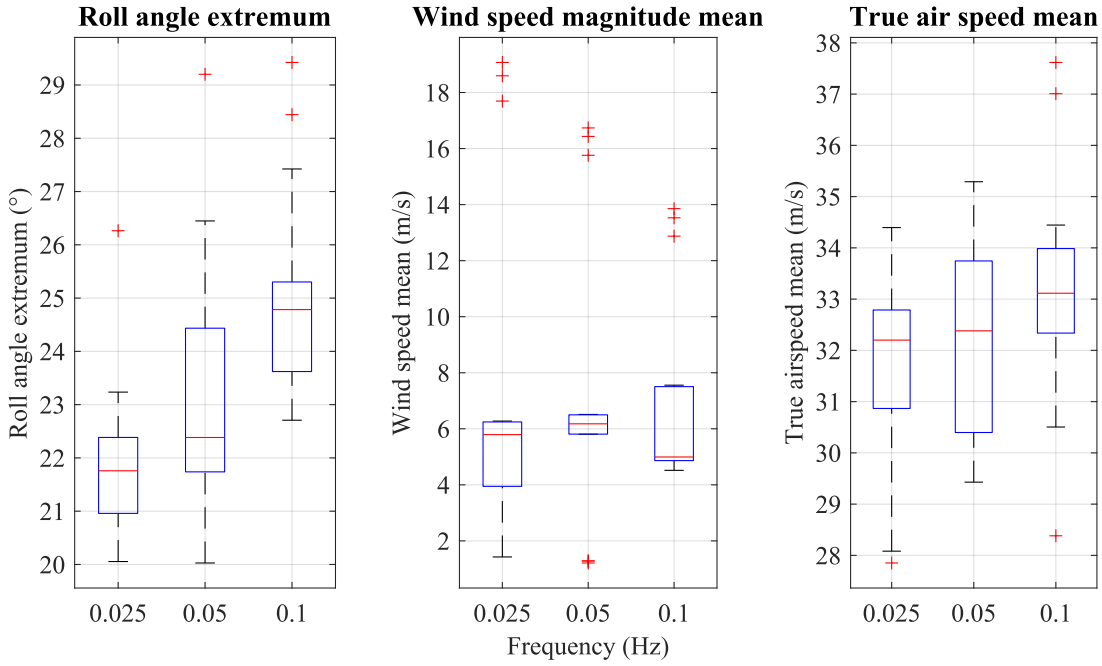

Figure 4.2: Some exemplary boxplots for the comparisons outlined in Table 4.1 [1]

To formalize this analysis, a Kruskall-Wallis test as described in Section 4.1.2 was applied to the mean value and maximum magnitude roll rate and angle, pitch rate and angle, true airspeed, height and wind speeds for each nominal oscillation frequency ($0.025\,\mathrm{Hz}$, $0.05\,\mathrm{Hz}$ and $0.1\,\mathrm{Hz}$). The p-value for this analysis is shown in tabulated form

[1] Red crosses mark data outliers, e.g in the middle of the three plots which denote especially windy flight segments. As detailed in Fig. 4.1, outliers are inserted if data points lie 1.5 times outside of the interquartile range

in Table 4.1. As can be seen from this table, most flight dynamic parameters do not

Table 4.1: P-values for the comparison of key flight dynamics parameter for the three nominal oscillation frequencies. Numbers marked in red are lower then the defined critical p-value of 0.05

	mean	maximum magnitude
Length of segment	0.091	-
Roll angle	0.108	0.0002
Pitch angle	0.121	0.141
Pitch rate	0.027	0.011
True airspeed	0.104	0.49643
Wind speed	0.620	0.620
Height	0.201	0.107

differ significantly over the different flight tests. Note that the roll rate is neglected in this table, as it is dependent on the frequency of the roll oscillation. A statistical evaluation of the relationship of these two parameters is therefore meaningless as they naturally correlate. Likewise, the deviation of maximum length was not evaluated, as such a value would also be of no meaning.

However, the maximum magnitude of the roll angle (see Fig. 4.2) and the mean and maximum magnitude of the pitch rate are lower then the previously defined critical p-value of 0.05 and are therefore viewed as dependent on the nominal oscillation frequency. Further analysis for the pitch rate reveals that the differences are very small ($\leq 1\frac{^\circ}{s}$) which is on the one hand close to the expected measuring uncertainty of this setup, and on the other hand can be safely attributed to cross-coupling and the manually piloted approach used in these tests. Either way, these small pitch angle rate differences are deemed to be acceptable.
The statistical significant difference of the maximum roll angle magnitude, or in other words the increased roll angle overshoot at higher frequencies, is a result of the natural steering behavior of the pilots. This correlation will be further described in Section 4.2.2.
Note that the flown height shows no statistical correlation, but differs throughout the flight tests. During the first ten flights, the flight height was chosen to be around 300-$400\,\mathrm{m}$ height above the (earths) ellipsoid (HAE) (≈ 200-$300\,\mathrm{m}$ Height above ground level (HAGL)), however because of a fear of noise complaints, the height of the flight was increased to roughly 700-$800\,\mathrm{m}$ HAE, or 600-$700\,\mathrm{m}$ HAGL. This decision was made independently by the pilots. Unfortunately, this was only discovered after the flight tests. It is unknown if this increase in flight height affected the visual stimulus and therefore the onset of motion sickness.

The remaining p-values presented in Table 4.1 exceed the critical p-value and can therefore be viewed as independent from the nominal oscillation frequency. Out of this reason, it is concluded that the flight dynamic parameters can be viewed as comparable throughout the flight tests.

4.2.2 Performance of the Auditive Cueing System

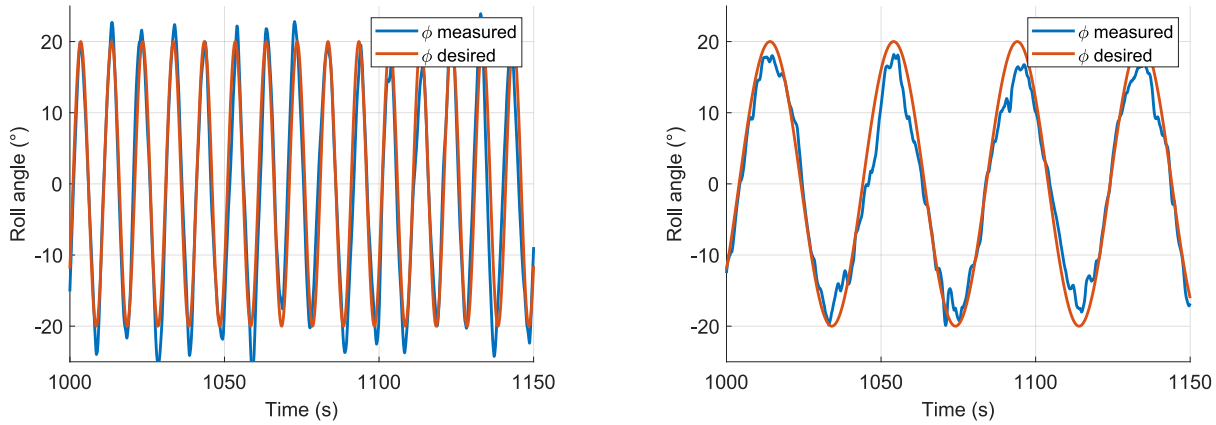

(a) Roll angle at $f = 0.1\,\mathrm{Hz}$ - Extract of first segment of flight 9

(b) Roll angle at $f = 0.025\,\mathrm{Hz}$ - Extract of first segment of flight 10

Figure 4.3: Two examples of resulting roll angle due to verbal pilot cueing. Desired roll angle which was verbally anounced in red, achieved roll angle in blue

In order to help the pilot fly the requested sinusoidal roll oscillation, an auditive cueing system was implemented as presented in Section 3.4. To analyze the performance of that system, the measured roll angle was compared to the reference signal which was generated and then verbally announced. As the reference signal could not be saved, the signal had to be reconstructed and aligned in time with the achieved roll angle. The reference signal is a harmonic oscillation of the form:

$$\varphi_{ref} = 20° \cdot \sin(2\pi f_{desired} \cdot (t + \Delta t_{shift})) \tag{4.116}$$

with $f_{desired}$ being the desired oscillation frequency, and Δt_{shift} being the unknown time shifting between the reference signal and the measured roll angle. The factor Δt_{shift} was determined via a cross-correlation approach, similar to that described in Section 3.7.1. Exemplary plots for the highest and lowest frequency flown during the flight tests comparing this reference signal to the roll angle achieved by the pilot can be seen in Fig. 4.3. Note that because of the fact that the reference signal is adjusted in phase via the cross-correlation approach, no *phase* information is given in the graphs. It is therefore unknown if the achieved sinusoid roll oscillation contained a time-shift or not. However, for the given task, such a time-shift would be irrelevant.

In Fig. 4.3a it can be observed that at a frequency of $0.1\,\mathrm{Hz}$ the pilot is able to follow the desired roll angle well, even though some overshoot is visible. At a frequency of $0.025\,\mathrm{Hz}$ shown in Fig. 4.3b, this overshoot is not present anymore. Similar conclusion can be drawn from the boxplot analysis shown in Fig. 4.2 which suggests that the higher the frequency, the more overshoot is present. It is evident that the pilot has some difficulties accurately following the desired roll angle especially near the reversal point of the oscillation. Pilots commented that at low frequencies they were sometimes overeager to roll back the helicopter especially when the oscillation reached this reversal point, simply because the oscillation was too slow for their natural steering behavior. At higher frequencies it can be concluded that the pilots were not able to dynamically control the helicopter in a tight enough way in order to ensure an accurate following of the reference signal. However, from Fig. 4.3 it can also be observed that the absolute frequency adherence of the roll oscillation is very good. This fact is nicely illustrated by a frequency analysis via a fourier transform. For the two specific segments shown in Fig. 4.3, these yield a frequency of $0.1003\,\mathrm{Hz}$ respectively $0.0251\,\mathrm{Hz}$ for the main frequency of the achieved roll angle oscillation during one complete 10 minute segment. In fact the *highest* frequency error over all recorded segments of the achieved vs. desired roll angle is not higher then $0.0004\,\mathrm{Hz}$. The complete results are detailed in Appendix B, Table B.3. It is therefore concluded that while the pilots were not able to perfectly steer the exact desired sinusoid waveform, the frequency adherence of the achieved roll oscillation is excellent for all segments of the flight tests.

This fact is a direct consequence of the chosen auditive cueing system. The auditive callouts are absolute in nature. Therefore, if the pilot can follow this reference signal with a constant delay, the desired frequency with a low margin of error will be achieved. The error between desired and achieved frequency is even lower the longer the segments are. With each segment having a nominal length of $600\,\mathrm{s}$, it is evident that this is an relatively easy task for the pilot. Of course this property is highly desirable for the overall experiment, as it ensures that the desired frequency could be easily and accurately steered by the pilots because of the chosen auditive cueing system therefore ensuring a constant test environment.
The tracking of desired roll angle is as good as it will be with a human piloted aircraft, shortcomings in the exact achieved waveform are acceptable given that the resulting frequency is the desired frequency. It is furthermore argued that it is hard to improve upon the achieved flight performance without either complete computer control of the helicopter or extensive pilot training. Both options could not be employed in the context of these flight tests. Because of the lack of alternatives and also good results of this approach, the setup is accepted without further improvements.

4.2.3 Test Subjects

Several key factors and metrics have been collected about the participating test subjects via the questionnaire described in Section 3.5.1. This was done for two reasons:

1. Pooling of test subjects
2. Statistical analysis of the corresponding metrics in order to rule out statistical correlation of test subjects and flown frequencies

The *pooling* approach was already described in 3.5.2, and will not be repeated here. Unfortunately it is not possible to evaluate this approach statistically. However, observation showed that this approach seemed to have worked well, as similar motion sickness susceptibility could be observed between the different test subject pairs. Therefore, if one of the two test subjects showed signs of motion sickness, the other one usually showed similar reactions.

The age of the test subjects lay between 18 and $54\,\mathrm{years}$ with a mean of $32.5\,\mathrm{years}$ and a standard deviation of $8.5\,\mathrm{years}$. Similarly, the weight was determined to lie between $57\,\mathrm{kg}$ and $100\,\mathrm{kg}$ with a mean of $75.75\,\mathrm{kg}$ and a standard deviation of $11.08\,\mathrm{kg}$. The height was found to be between $159\,\mathrm{cm}$ and $198\,\mathrm{cm}$ with a mean of $176.1\,\mathrm{cm}$ and a standard deviation $9.81\,\mathrm{cm}$. No statistical difference between the age (p-value: 0.963) in correlation to the three oscillation frequencies was found. The same applies for weight (p-value: 0.051) and height (p-value: 0.067). Boxplots of these variables are shown in Fig. 4.4 [18]. Additionally, some metrics described in Section 3.5.1 were analyzed concerning statistical relations. No statistical significant dependency for the travel frequency in the past year $T_{(yr.)}$ (p-value: 0.509), the illness susceptibility in transport in the past year $I_{susc.(yr.)}$ (p-value: 0.583) and the total susceptibility for motion sickness in the past year M_{total} (p-value: 0.597) could be found [18]. It is therefore concluded that the test subjects were evenly distributed among the different frequencies. Boxplots of these variables are displayed in Fig. 4.5.

4.2.4 Motion Sickness

Arguably the most important data gathered during the test flights is that of the motion sickness perceived by the test subjects during the flight. In total, 16 sorties with 32 test subjects have been performed. As mentioned in Section 3.3, the test subjects were asked to rate their subjective motion sickness perception on a scale from 0-6 defined in

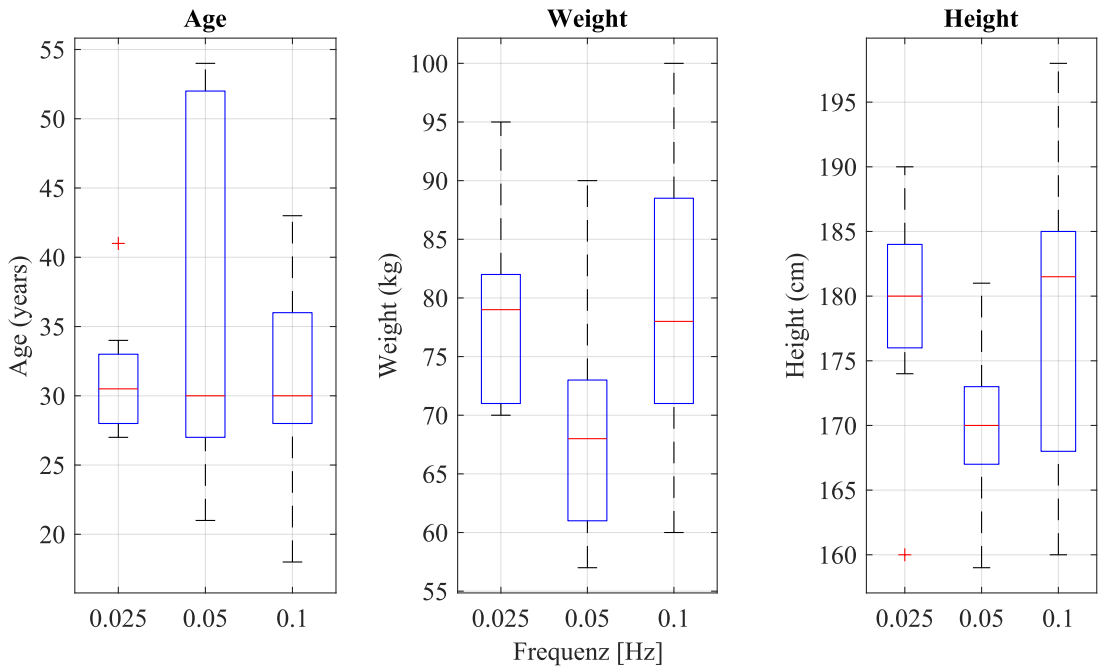

Figure 4.4: Distribution of the physical characteristics of the participating test subjects, taken with adaption from [18]

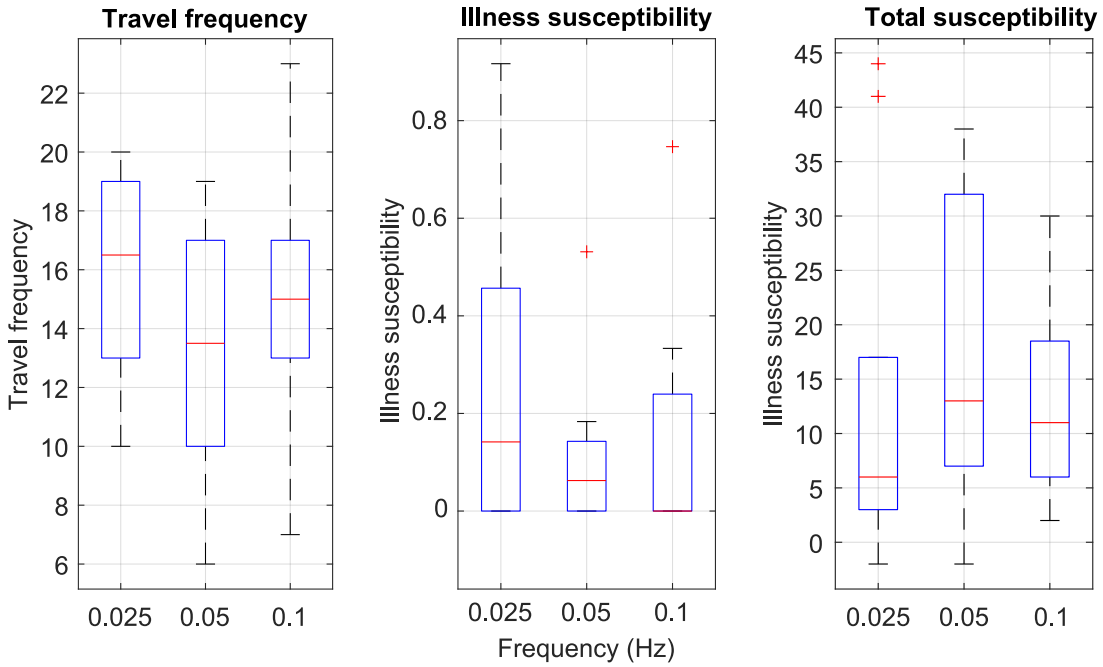

Figure 4.5: Distribution of pre-flight metrics of the participating test subjects, taken with adaption from [18]

Table 2.1 whereby level 6 corresponds to the maximum motion sickness and is considered to be crossed shortly before the test subject would throw up. One test flight was ended by the test subject because a motion sickness level of 6 was reached in the third and final leg at the 26 minute mark. Another test flight was ended by the test subject because of not further specified medical reasons, however the test person stated that it had nothing to do with motion sickness. The results of this test subject were discarded in order not to compromise the data. Only one vomiting event has been reported during the test flights, however only *after* the third and final leg of the test flight, when the helicopter was on its return journey. This incidence is therefore not marked in the flight test data. Interestingly enough the test subject in question reported only minor motion sickness ratings before vomiting.

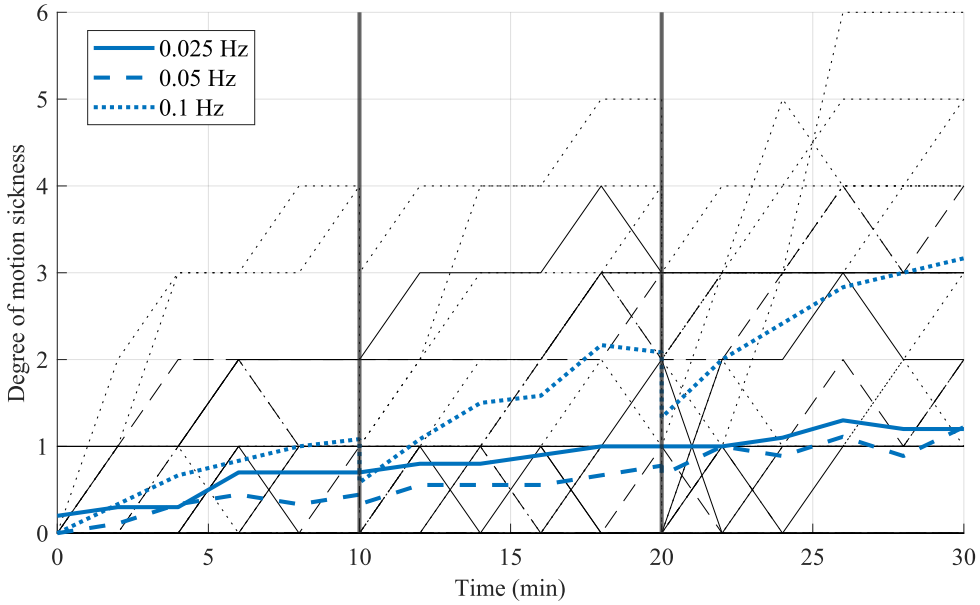

Figure 4.6: Time series of the recorded motion sickness ratings during the test flight. Faint grey lines represent individual test subjects, thick blue lines represent the mean motion sickness per frequency

An overview of the recorded motion sickness is shown in Fig. 4.6. In this graph, the mean of the reported motion sickness ratings during the flight is plotted in blue for the three different frequencies. Additionally, faint lines indicate the motion sickness degree as reported by individual test subjects. As described above, two test flights ended prematurely whereby the data of one test subjects was excluded due to reasons stated above. Therefore, in total the data of three test subjects ended before the nominal test length was achieved. For the data analysis of these cases, the last reported motion sickness degree was held constant for the remainder of the flight. The mean was then computed with these added-in values. It should be noted that especially the line representing the motion sickness degree for $0.025\,\mathrm{Hz}$ does not start at a rating of 0 at the beginning of the graph, as some test subjects reported slight symptoms as a result of the

transit flight to the test track. Noteworthy are also the drops of motion sickness degree at the 10 and 20 minutes mark, especially for the $0.1\,\mathrm{Hz}$ frequency. This stems from the fact that at these points the test flights were interrupted while the helicopter performed a $180°$ turn-around curve between each of the three experiment legs. Some test subjects felt this to be a relieve and consequently lowered their reported motion sickness rating at the beginning of the next leg. Interestingly enough, the general trend seems to make up for this intermediate drop after a couple of minutes.

All-in all, the motion sickness onset especially for $0.1\,\mathrm{Hz}$ is clearly visible. A Kruskal-Wallis test reveals a statistical significant difference in the motion sickness degree at the end of the flight ($= 30\,\mathrm{min}$) between the three frequencies, with a p-value of 0.0168, well below the 5% threshold set earlier. Additional Mann-Whitney U tests show that a statistical significant difference between the motion sickness degree at the end of flight for the frequencies $0.025\,\mathrm{Hz}$ and $0.1\,\mathrm{Hz}$ is present (p-value 0.0143), and likewise between $0.05\,\mathrm{Hz}$ and $0.1\,\mathrm{Hz}$ (p-value 0.0226), however no statistical significant difference is present between the motion sickness degree at the end of flight of $0.025\,\mathrm{Hz}$ and $0.05\,\mathrm{Hz}$ (p-value: 0.7646). The according boxplot is displayed in Fig. 4.7.

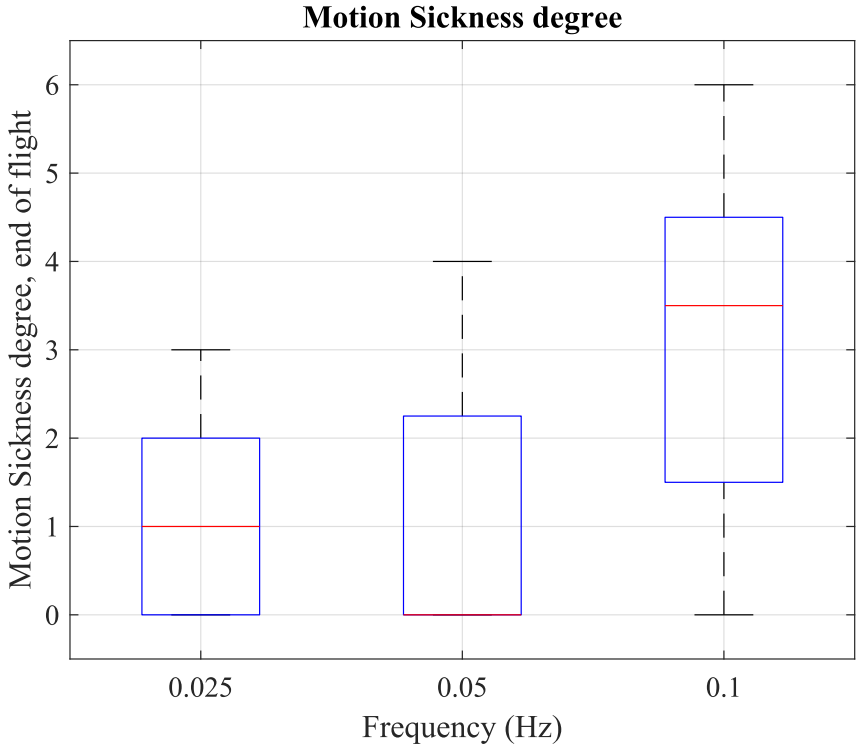

Figure 4.7: Boxplot of reported motion sickness over frequencies at the end of flights

In the experimental test of the Griffin dataset, the experimenter could monitor the test subjects via a video camera, additionally the test subjects had to indicate which symptom exactly led them to their motion sickness indication. Such sophisticated and accu-

rate control methods could not be implemented during the flight tests again for reasons of equipment certification and overall technical complexity.

4.3 Prediction of Motion Sickness

As a final step, this chapter will compare the motion sickness of the test subjects recorded during flight to the predicted motion sickness of the improved Kamiji model, described in Section 2.3, if that model is handed the movement data recorded during these test flights.

For this, the relevant motion data of each of the 16 flights as calculated by the flight path reconstruction algorithm described in Section 3.7 was cut to the time-sections containing the roll-oscillations, and then fed into the improved Kamiji model. The used data consists of the rotational rates, the euler angles and the inertial accelerations. As described in Section 2.3, several sets of parameters exist for this model, each tuned to predict the percentage of people reaching a certain motion sickness degree, whereby this degree runs from 1 to 6 as described in Table 2.1. The results of all 16 flights for each of the six developed model parameter sets is shown in Fig. 4.8. The x-axis of this model spans the 30 minutes of the flight tests, whereby some lines end a bit earlier, as these tests flights were ended prematurely due to the aforementioned reasons.

The subplots of Fig. 4.8 contain several important effects which will be discussed in the following. The ordinate of all of these graphs is denoted in percentage of people reaching a certain motion sickness degree, or rather the prediction of this value, which will be abbreviated as percentage of people reaching a motion sickness degree PMSD of x, with x ranging from 0 to 6. The lines for each oscillation frequency form a family of curves whereby the flight conditions between the flights apparently differed enough such that the motion sickness model estimated slightly different predicted PMSD of up to 10%. The family of curves of the different frequencies are however clearly separated especially for MSD 4, 5, and 6. Furthermore, it is noted that the predicted PMSD 1 shown in Fig. 4.8a is bigger than that of predicted PMSD 2 shown in Fig. 4.8b which in turn is bigger than that of Fig. 4.8 and so forth. This means that the models fitted to increasing MSDs infact predict increasing motion sickness. Therefore, the different parameter models seem to be consistent both in itself and also between each other. It is furthermore observed, that the family of curves for each oscillation frequency are clearly separated from one another and can be distinguished without any problems.
Note that especially models for MSD 1 and 2 however, may suffer from bad data quality, as the data used to optimize these models saturate often at 100%. While this effect was mitigated by choosing an optimization scheme which optimizes the models for MSD 1-6 in parallel, this effect may still be present. Due to the nature of the improved Kamiji

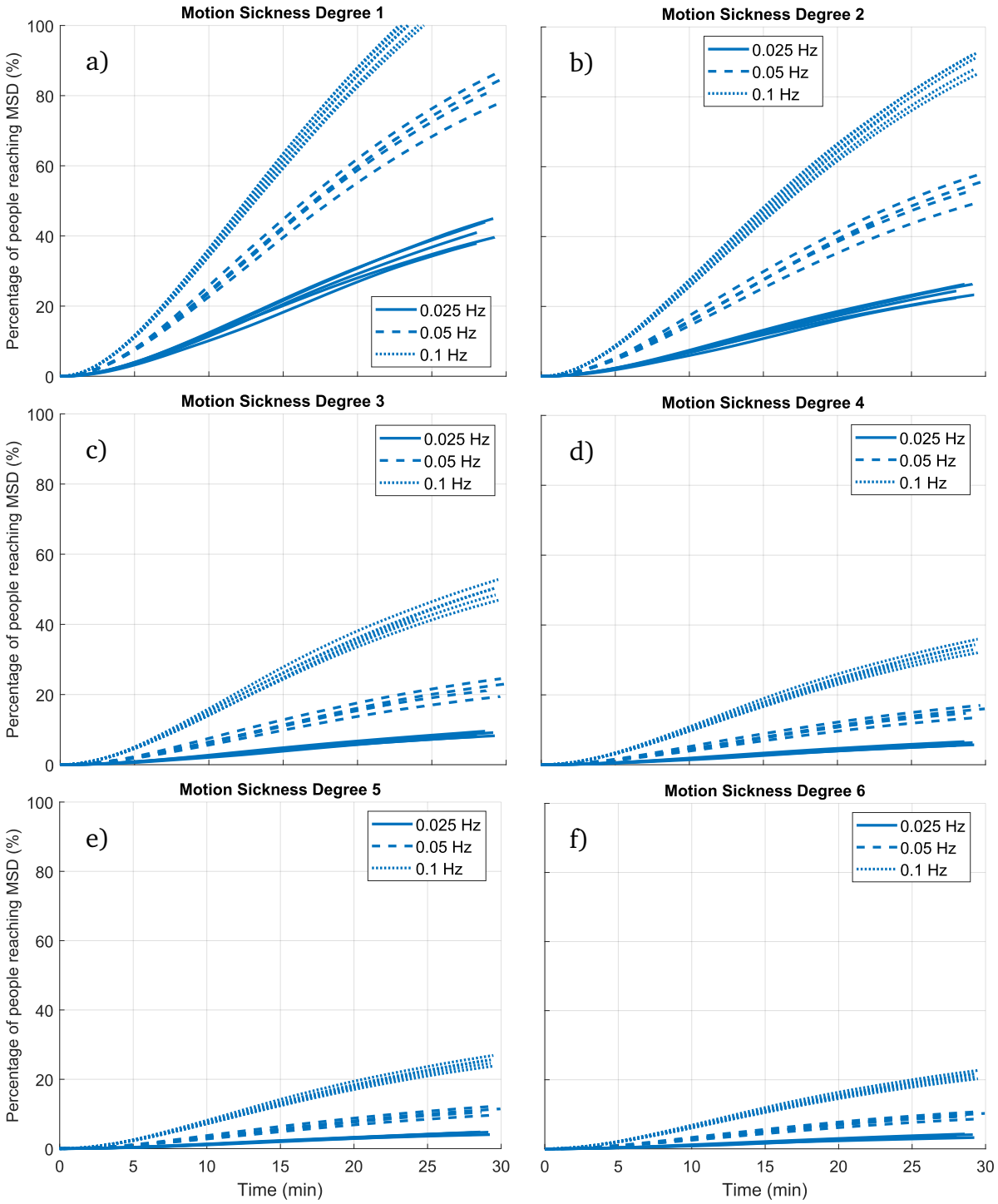

Figure 4.8: Predicted percentage of people reaching a certain motion sickness degree for each of the 16 flights. The used model is the improved Kamiji model with the six developed parameter sets

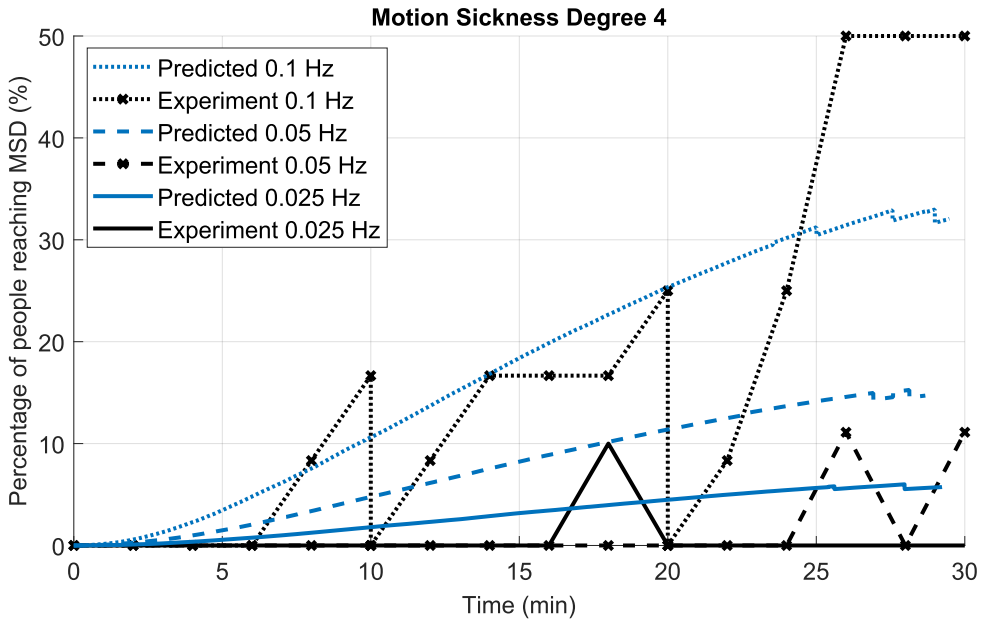

Figure 4.9: Time series comparison of mean predicted (blue lines) and experimental (black lines) percentage of people reaching motion sickness 4 for the performed flight tests

model, especially because of the added K_{out} gain, fitting to these conditions might result in less-then desirable results. As pointed out in Section 2.3.2 the introduction of this K_{out} gain block in the output path of the improved Kamiji model also leads to outputs which can exceed more than 100%. This effect is visible in Fig. 4.8a in which predictions for $0.025\,\mathrm{Hz}$ reach a level of over 100%. Again this is an expected effect which is unavoidable for the model modifications which were performed for the improved Kamiji model.

Probably the most interesting comparison is that of the predicted motion sickness compared to that observed during flight tests. Shown in Fig. 4.9 is the mean motion sickness for predicted PMSD 4 as computed by the improved Kamiji model in comparison to that observed during the flight tests. Note that the predicted mean for the different frequencies is calculated by taking the mean of the signals shown in Fig. 4.8d. This also explains the discontinuities beginning at $t = 25\,\mathrm{min}$: Some flights ended earlier then others, in that case the mean is calculated from the remaining lines which results in these discontinuities. The experimental data also shows cuts at the 10 and 20 minutes mark as the turn-around curves were located at these time instances, which offered a slight relieve in motion sickness for the test subjects introducing the cuts in reported motion sickness. After the completion of this turn-around maneuver, the motion sickness degree seems to recover quickly such that the overall trend is not significantly disturbed. What can be clearly observed in this figure is that the prediction, especially for the highest frequency of $0.1\,\mathrm{Hz}$, seems to agree well with the experimental data. Also the time series of the predicted and experimental data seems to agree inside the bounds which can be

expected for statistical data.
Such high coherence between experimental observations and computed prediction is however not given for all parameter models. An overview between the predicted and experimentally determined percentage of people reaching the different levels of motion sickness is shown in Fig. 4.10. These plots visualize the percentage of people reaching motion sickness degrees 1-6. The predicted motion sickness degree is shown in form of a boxplot whereby the red diamond indicates the mean predicted motion sickness degree for each of the six models. In comparison, the experimentally determined mean percentage of people reaching a certain motion sickness degree is overlaid as a black line. Note that it is not possible to visualize the statistical distribution of this value for the experimental case as that parameter is binary: Either people reach e.g. MSD level 3 or not. For this reason the computation of the median would also be meaningless, as it would be either 0, 0.5 or 1. Thus in Fig. 4.10 the mean of the reached predicted and experimentally determined motion sickness is compared.

As can be seen from Fig. 4.10, some models agree better then others. In the case of MSD 1 for example, the prediction is well above the 100% mark, a result of the additionally introduced gain in Section 2.3.2. In the case of MSD 6 of the same figure, the prediction, albeit close, does not perfectly capture the experimental results. Again the number of observations is low, but still a difference of 10% exists. It becomes evident that the model for MSD 4 might strike a good balance between data fidelity which enables a good fit of the model, and clearly recognizable motion sickness resulting in robust results for the experiment.

4.4 Discussion

The general systems and questionnaires needed for the evaluation of the flight tests performed as intended. The developed flight path reconstruction algorithm based on the Garmin G500H TXi and the smartphone temporarily installed on the back seat were presented in Section 3.7. It was evaluated that the estimates of the systems are not perfect in some aspects, for example the estimated roll oscillation presented in Fig. 3.20 does not agree 100% with the raw measurements of the Garmin avionics. This could be a result of the measuring accuracy of the avionics or due to the high noise level of the smartphone. Several options exist to improve this result, for example further tuning of the flight path reconstruction algorithm and the underlying unscented Kalman filter. A more rigid mounting of the smartphone or testing out other recording methods could

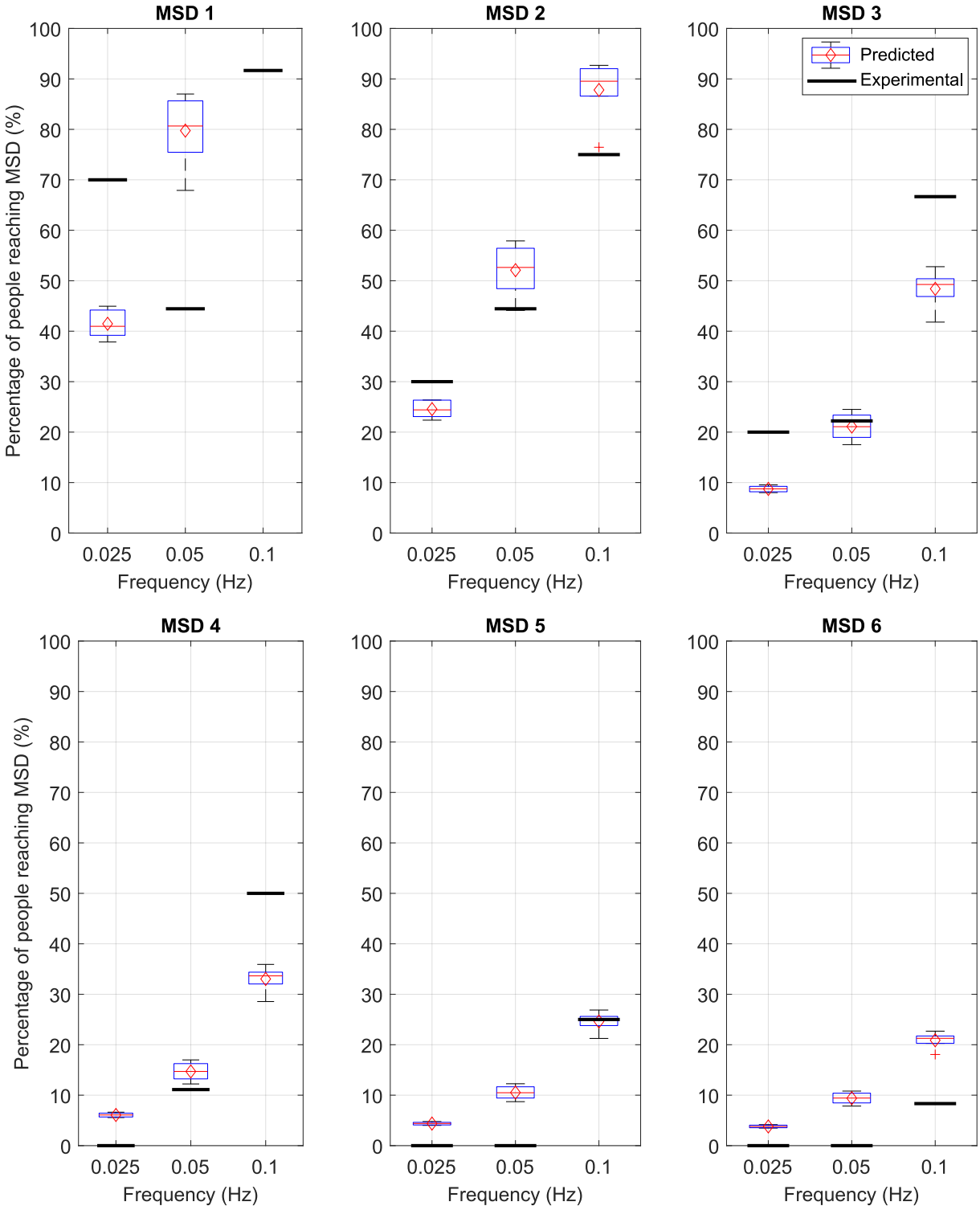

Figure 4.10: Boxplots of predicted and experimentally determined percentage of people reaching motion sickness degrees 1-6. Predicted mean is shown as a red diamond, experimental determined mean is shown as a black line

also lead to better data quality. However, after careful consideration of the data, the overall quality of the data was deemed to be acceptable.

The alternative to this flight path reconstruction approach would be to install a full-fledged experimental data acquisition system and while this is planned for the BO-105 helicopter, the system still has not be installed yet. All in all, the usage of the flight path reconstruction algorithm in conjunction with the Garmin G500H TXi avionics unit and the temporarily installed smartphone is considered to be a good replacement and overall a success!

In a similar fashion, the implemented cueing system for accurately following a fixed-frequency roll oscillation as presented in Section 3.4 worked equally satisfactory. Again some defects exist: At lower frequencies some disturbances can be observed in the following of the sinusoid, and at high frequencies overshoot is present. However, the frequency adherence of the resulting sinusoid oscillation is excellent, which underlines the effectiveness of this cueing system. Overall and for a manually piloted aircraft, the implementation usage and execution of the auditive cueing is also considered to be successful.

As a result, occurences of motion sickness could be observed during flight. Statistical analysis reveals that the driver for this is mainly the frequency, as was expected based on literature sources. Unfortunately, no statistical significant difference in motion sickness between the lower two frequencies, $0.02\,\mathrm{Hz}$ and $0.05\,\mathrm{Hz}$, can be identified. It is not clear why exactly such little difference between these two frequencies is seen. Noteworthy is that the improved Kamiji model predicts a difference of only 10% of people reaching MSD 4 for these two frequencies as can be seen in Fig. 4.9, which points in a similar direction as the experiment, namely that the motion sickness potential of these two frequencies is (equally) low. Obviously, the sample size of the experiments is low with only 10 people per frequency, therefore statistical noise may easily overlay the data. This theory is supported by the fact that the Griffin dataset has a minimum of 20 people per frequency point, and still some statistical noise can be observed in the dataset: For example in Fig. 2.14 at a compensation of 100% the datapoints do not follow a smooth line, and are in some cases even vertically distributed, a clear sign of too small observation size for the specific samples.

It is important to note, that in general the statistical results of the flight tests could be improved with a higher observation number per sample. In this study, the number of observations per frequency was set to 10 respectively 12 observations per frequency. Sometimes as a rule of thumb, 100 observations per sample is recommended [79]. However, a suitable number should be set in a dedicated analysis. The number of experiment

flights performed during this study was set in response to budget constraints, as flight tests are prohibitively expensive. This however is clearly adverse to the precision of the results.

Nevertheless, the improved Kamiji model as developed in Section 2.3 seems to agree well with the experimentally determined values. Especially the model developed for MSD 4 agrees well with the flight tests as can be seen in Fig. 4.9. The advantage of the model fitted to MSD 4 is that it offers a good compromise between meaningful motion sickness which is also recognized by test subjects during flight tests and therefore delivers robust results and good data fidelity with a significant number of people actually reaching this motion sickness degree, therefore enabling correct fitting of numerical models to this MSD. Models fitted to MSD 1 and 2 contain the drawback that too many people reach these degrees, which quickly saturates the percentage of people reaching those degrees at 100%. Consequently, the according models exhibit an improper fit, and therefore only contain limited data. The opposite is true for very high MSDs such as MSD 6. Practically no one reaches these high levels, which again results in suboptimal fits of the model for these cases. MSD 4 however, is described as "*Mild to moderate nausea*", which already is a meaningful state of motion sickness in contrast to MSD 1 and 2. It is argued that MSD 4 is more relevant for the design of flight control laws or similar applications, as higher levels of motion sickness should be avoided as these are likely to entail vomiting and extended periods of recovery.

For this reason it is concluded that the improved Kamiji model in combination with the tuning developed for motion sickness degree 4 is a good candidate for predicting motion sickness for VTOL applications such as traditional helicopters or air taxis.

5 Conclusion and Outlook

The goal of this work was to develop an appropriate tool for judging the severity of motion sickness on passengers and pilots for vertical lift applications. It is foreseen that such a tool will help with the design of flight control or path planning algorithms for existing and future VTOL aircraft such as conventional helicopters or for the application in the upcoming technology of urban air mobility vehicles. The following chapter will conclude the performed work and will give answers to the scientific questions as formulated in Section 1.5. Furthermore, a short outlook on possible future research directions will be provided.

5.1 Conclusion

The scientific question formulated for this thesis states "**How can the effect of motion sickness of pilots and passengers be quantified and predicted for the design of rotorcraft?**" whereby the question is structured in several parts. The first question is "**How can motion sickness be mathematically modeled and simulated as a function of a given trajectory or motion?**" To answer this, several motion sickness models were evaluated. It quickly became apparent that existing motion sickness models show several deficiencies, which hinder the application of the models to the specified problem. For instance the well known, well adopted ISO 2631 standard specifies frequency weighting curves which help to judge the impact of a specific vibration on motion sickness. However, such a frequency curve is only given for the vertical axis, neglecting the influence of longitudinal and lateral oscillations as well as any rotatory movement.

For this reason a different modeling approach was adopted from literature, which tries to explicitly model the human motion sickness mechanism. As a first step, the conflict theory was introduced in Section 1.3.1. This theory postulates that motion sickness in humans is caused by an information conflict between the inner ear and the eye. Shortly put, this theory states that if the motion information of the inner ear does not align

with the motion information perceived by the eye (and prior experience), motion sickness will arise. In Section 2.2.2, the Kamiji motion sickness prediction model which tries to explicitly model this conflict for three translatory and three rotatory axes was selected from literature. However, this original motion sickness model showed lacking congruency to experimental data of motion sickness simulators also taken from literature.
To improve this modeling deficiency, a two staged approach was taken in Section 2.3:

1. The model structure was adapted by introducing suitable additions to the model. On the one hand this improved the compatibility with current aerospace standards, and on the other hand it allowed more flexibility of the model in regards to the second step. This model is called the improved Kamiji model.

2. An optimization approach was adopted in order to find an revised set of parameters for the improved Kamiji model.

The data basis for the optimization was formed by experimental data taken from literature. This dataset, called the Griffin dataset in this thesis, consists of a total of seven different papers, each containing a set of motion sickness experiments. These were performed on the Southampton $12\,\mathrm{m}$ Tilting and Translating Cabin, which, as the name suggests, allows for translatory longitudinal or lateral oscillation that can be combined with a roll or pitch oscillation. During each experiment one motion candidate was evaluated with the help of the motion simulator whereby the resulting motion sickness of the test subjects was recorded. In total, the dataset contains data of 560 subjects completing roughly $620\,\mathrm{hours}$ of testing inside the Southampton motion simulator. Due to the extent, consistency in setup, and overall quality, this dataset is a valuable source for the intended purpose.

Using a nonlinear optimization algorithm, the parameters of the improved Kamiji model were tuned in order to better predict the experimental Griffin dataset. Six different model parameter sets were generated, each predicting the percentage of people *reaching* a certain motion sickness degree running from 1 (very low motion sickness) to 6 (very high motion sickness), whereby the models were optimized in parallel to avoid the optimization to a local minima. Furthermore, it was shown that the improved parameters yield a better prediction than the original parameters in regards to the Griffin dataset. Nevertheless, it has to be noticed that the modification of the Kamiji model breaks the original property that predicted motion sickness cannot reach more than 100%. While this disadvantage of the improved Kamiji model is not relevant for most use cases, this fact should be kept in mind.

The second part of the scientific question asks: "**How can the developed motion sickness model be validated?**" and further inquires "a) **Are motion simulators a viable option for validating the motion sickness model**"? This question is answered in Section 3.1 in which the bounds of two simulators, the AVES motion simulator and the University of Southampton's $12\,\mathrm{m}$ Tilting and Translating Cabin were examined. Hereby, it was shown that these two motion simulators only possess a limited ability to emulate movements of a rotorcraft vehicle due to the constraints in displacement, velocity and acceleration. Modern motion simulators often employ techniques which enable flight simulators to approximate and mimic flight motions by exploiting the limited perception capabilities of the human vestibular system. It is unknown if the same techniques can be used for motion sickness applications. However, it should be noted that that the vestibular system plays an important role in the formation of motion sickness, it is not evident if the vestibular system can be simultaneously tricked to cue a motion while measuring the onset of motion sickness of the same vestibular system.

It was therefore determined that the best way to validate the improved Kamiji model is to perform flight tests which mimic the intended flight profile. Due to this reasoning, flight tests were performed which featured horizontal oscillations at a typical cruising speed, comparable to maneuvering flight for example in densely used airspace.

Part 2b) of the scientific question "**How can a corresponding study be implemented from a technical standpoint?**" was answered in Chapter 3 which described the general test methodology and specific technical solutions necessary for the successful execution of these flight tests. The flight experiment was loosely based on the methodology of the papers of the Griffin dataset in order to enhance the comparability between the tests and the dataset. Horizontal flight maneuvers were chosen as it is argued that the majority of flight time of an UAM vehicle is spent during cruise flight, which primarily features horizontal maneuvering for obstacle avoidance.
Flight tests were performed using DLR's Bölkow BO-105 Helicopter with a total of 32 test subjects in 16 flights separated in two flight test campaigns. Two test subjects participated in each flight test and flew at one of three oscillation frequencies for a total test time of approximately 30 minutes. Test subjects did not participate in more than one flight test in order to rule out adaption effects. Furthermore, every test subjects was exposed to only one frequency. As a prerequisite, all participating test subjects filled out a pre-flight questionnaire which determined the self-conceived motion sickness susceptibility, travel frequency and other data. As a test flight was terminated if the test subjects would indicate excessive motion sickness, for each test flight two participants with similar motion sickness susceptibility were pooled in order to maximize flight time.

For data analysis with the aforementioned motion sickness prediction model, accurate motion information had to be available. The necessary data was acquired with the Bölkow BO-105 helicopter which was available, relatively cheap to operate and features up to three available passenger seats of which for experiment reasons, only two were occupied. While in theory also DLR's highly modified Airbus Helicopter EC 135 ACT/FHS could have been used, it was decided to favour the Bölkow BO-105, because of the aforementioned advantages. Especially significant is the fact that with the Bölkow BO-105 two test subjects could be carried per flight in contrast to a maximum of one test subject inside the ACT/FHS which, in addition, is more expensive to operate. Combined with the higher operating cost, the cost per test person could therefore be more then halved in comparison to similar flight tests with the ACT/FHS. However, the Bölkow BO-105 helicopter is not equipped with a data recording device. Due to this fact, an alternative approach for data recording was adopted in which data from the built-in Garmin G500H TXi avionic system was fused with data obtained from a temporarily installed smartphone via an unscented Kalman filter. This procedure combines the low frequency but high accuracy information of the Garmin G500H TXi system with the high frequency but low accuracy information of the smartphone and results in a complete state estimation with a unified sampling time and additional data such as a wind estimation. Later analysis involving the state information of the helicopter was then based on this estimation of the helicopter's dynamic state information.

Another important factor was that of accurate control of the helicopter during the flight tests. To ensure accurate adherence to the prescribed oscillation frequency during the flight trials, a spoken audio cueing system was implemented via a custom application running on the digital kneeboard of the pilot which was connected to the intercom system of the helicopter. The application could be configured to emit spoken roll angle commands which the pilot had to interpolate such that a smooth continuous roll oscillation would result. Data analysis showed that this setup performed well and the desired frequency could be flown with minimal frequency deviation. When comparing the requested roll oscillation to that recorded during flight, small deficiencies in the time-domain could be identified, however for the given application and a manually piloted helicopter, the performance was deemed acceptable. It should be noted that pilots commented that little training was needed for the adoption of the system and that it was possible to fly eyes-out, therefore normal operation of the helicopter was not disturbed. The resulting workload of the test setup for the pilot was high.

The obtained motion sickness data from the flight tests was statistically evaluated to rule out hidden dependencies. First, key flight dynamic parameters were evaluated in comparison to the oscillation frequency in order to confirm that comparable flight

dynamic situations were present during the flight tests which noted that overall the conditions were similar amongst all flight tests. Then a performance evaluation of the auditive cueing system was given, which concluded that satisfactory performance of this system was achieved. Furthermore, the distribution of test subjects amongst the different frequencies was analyzed, which also concluded that no statistical significant differences between the test subjects of the three frequencies were present.

Concerning motion sickness, several factors were analyzed with the goal of better understanding which parameter exactly caused the occurrence of motion sickness. Test subject parameters collected via pre-flight questionnaires such as travel frequency or illness susceptibility were tested against the occurrence of motion sickness. As expected, the only statistically significant relation was determined to be the oscillation frequency, which indicates a clean flight test execution.

Finally, subquestion 2c) "**How does the prediction quality of the motion sickness model compare to its validation?**" is answered in Section 4.4. The predicted motion sickness as computed by the improved Kamiji model parametrized with the different calculated parameters of the aforementioned tuning, was compared to the recorded motion sickness results. In order to compute the predicted motion sickness, the flight data as calculated by the flight path reconstruction algorithm was used. Comparing the predicted and observed motion sickness, it became evident that some models fit the experimental data better then others. The parameter tuning for motion sickness degree 4 was identified to render the best results, as this tuning offers a good compromise between data fidelity and meaningful motion sickness in contrast to other tunings which suffered from overfitting effects. It was furthermore concluded that the improved Kamiji model in combination with the parameter tuning of motion sickness degree 4 is the most promising combination for a suitable simulation tool in respect to predicting motion sickness.

Nevertheless, it is pointed out that the statistics of the experimental results have to be taken with a grain of salt, as the observation numbers are relatively low. In total, 32 observations distributed over three frequencies have been taken, a rule of thumb dictates that 10 times more observations would be needed for a reliable statistic.

Given these results and the development process of the improved Kamiji model, the third part of the scientific question 3. "**How can such a motion sickness prediction model be deployed and used for the development of more comfortable flight control systems?**" becomes clear. As stated in Section 1.5 the improved Kamiji model represents an numerical tool which can analyze a given trajectory, flight path, motions

or even single maneuvers supplied in the form of motion data. The designer of a corresponding vehicle or flight control system is therefore enabled to check and compare the design for motion sickness stimulation and can adjust accordingly.

5.2 Outlook

The contributions made in this thesis are aimed at engineers seeking to maximize passenger comfort of rotorcraft vehicles in general, but especially for UAM vehicles and their missions. The improved Kamiji model could be used for according design tasks. However, while the developed motion sickness models and validation techniques proofed to be successful, some potential for future developments and improvements were also identified.

As described in Section 2.2.2, the original as well as the improved Kamiji model represent the motion conflict theory by implementing a structure similar to the hypothesized motion sickness conflict mechanism. It should be noted that this structure in parts is a choice made by the authors of the Kamiji model. The chosen structure obviously directly impacts the solution such a model is capable of. Better results might be achieved by a different, yet to be determined, structure of the Kamiji model. For example some of the blocks of that model were chosen to have no dynamic, a first order dynamic or second order dynamics. A structured approach to explore other types of modeling choices could potentially further improve this model. One approach could be the usage of neural networks for parts of this model or the entire mechanism. The human brain itself consists of such neural networks, it is therefore an obvious idea to model the conflict theory also as such a neural network.
Another insight gained during the development of the improved Kamiji model is that the developed motion sickness model predicts the percentage of people *reaching* a certain motion sickness degree. It might be advantageous to reformulate the output of the model such that a certain motion sickness degree is given. It should be noted that the Griffin dataset as gathered for this thesis does not lend itself for this approach, as in the referenced papers this data is not published.

In Section 3.1 the limits of motion simulators for emulating motion sickness movements was discussed. Hereby it was shown that the motion simulators in question are severly restricted in the types of motion which can be simulated. Nevertheless, motion simulators offer a myriad of advantages compared to flight tests such as lower operation cost, better availability or better access to test persons. The recently introduced passenger

cabin [80] for the AVES is capable of seating 20 test subjects, which could be used to test very large numbers of test subjects simultaneously. While it should be noted that the sight of vomiting or excessive smell can lead to motion sickness in other test subjects [52] and therefore care has to be taken if one test subject shows symptoms of motion sickness, careful experiment design could circumvent these problems.
Another simulator which is worth noting is the new cable robot of the Max Planck Institute for Biological Cybernetics [81]. This machine is able to carry an adult human whereby the cabin can be moved inside a room of $8x5x5\,\mathrm{m}$ with a maximum acceleration of up to $\approx 15\,\frac{\mathrm{m}}{\mathrm{s}^2}$. The motion limits of this machine are much higher than those discussed in Section 3.1 and therefore most motions which would otherwise be only achievable in flight tests, can be simulated by this cable robot. The machine has already been used in motion sickness tests [82].

One factor which was not explicitly examined was that of atmospheric disturbance. Bahr et al. [30] note that atmospheric disturbance affecting a typical multirotor UAM vehicle lead to translational acceleration spectra with a low pass characteristic and a corner frequencies of $0.2\,\mathrm{Hz}$. Motion sickness sensitivity peaks at $0.2\,\mathrm{Hz}$ [35], therefore such turbulence may cause motion sickness. While the performed BO-105 flight test inherently contain turbulence, the experiment was designed to minimize the influence as relatively calm days were selected for flight tests. Nevertheless, the improved Kamiji model should be able to predict motion sickness also from unstructured movements such as turbulence although this capability has not been tested yet.

As a final thought, the application of the developed models should be practiced on an existing flight control structure. It has yet to be determined what the exact implications of such an applications are.

A ISO 2631-1: Definition of frequency filter

The ISO 2631-1 [16], specifies linear frequency filters for application to (acceleration) vibration data. For the analysis of vibration data in context of motion sickness, the W_f filter depicted in figure 2.1 is used. This filter is defined as a concatenation of four linear filters as follows:

$$H(s) = H_h(s) \cdot H_l(s) \cdot H_t(s) \cdot H_s(s) \tag{A.117}$$

These are a low-pass and a high-pass filter as well as so-called acceleration-velocity transition and an upward step.

$$H_h(s) = \frac{s^2}{s^2 + \sqrt{2}\omega_1 s + \omega_1^2 s} \tag{A.118}$$

$$H_l(s) = \frac{s^2}{s^2 + \sqrt{2}\omega_2 s + \omega_2^2 s} \tag{A.119}$$

$$H_t(s) = \frac{1/\omega_3 s + 1}{s^2/w4^2 + s/(Q4 * w4) + 1} \tag{A.120}$$

$$H_s(s) = \frac{s^2 + \omega_5/Q_5 s + \omega_5^2}{s^2 + \omega_6/Q6 + \omega_6^2} \tag{A.121}$$

With the following parameters:

Table A.1: Frequency weighting parameters for the frequency weighting curve W_f

Weighting	f_1	f_2	f_3	f_4	Q_4	f_5	Q_5	f_6	Q_6
W_f	0.08	0.63	∞	0.25	0.86	0.0625	0.8	0.1	0.8

It should be noted, that this filter shall only be applied to vertical acceleration data a_z. The frequency weighted signal $a_{z,w}$ can be easily calculated by applying $H(s)$ on the signal a_z via any numerical calculation program like MATLAB® or the python programming language.

B Flight Data Overview

The following appendix gives and tabelated overview of the flight tests performed. The tests were performed in two flight test campaigns, with up to three flights per day. Table B.1 indicates the date and general wind conditions on all flight test dates. Table B.2 to Table B.6 lists key values of the various flight tests in tabulated form.

Table B.1: List of performed flight tests in the two flight test campaigns

Flight ID	Flight test campaign	Date	Frequency (Hz)	Wind Condition at ground level (Beaufort scale)
1		13.09.2021	0.05	2: Light breeze
2		13.09.2021	0.1	2: Light breeze
3		14.09.2021	0.2	3: Gentle breeze
4	1	14.09.2021	0.05	3: Gentle breeze
5		15.09.2021	0.2	3: Gentle breeze
6		16.09.2021	0.05	3: Gentle breeze
7		16.09.2021	0.1	4: Moderate breeze
8		19.10.2021	0.1	3: Gentle breeze
9		19.10.2021	0.2	4: Moderate breeze
10		19.10.2021	0.05	4: Moderate breeze
11		20.10.2021	0.1	4: Moderate breeze
12	2	20.10.2021	0.2	3: Gentle breeze
13		20.10.2021	0.05	5: Fresh breeze
14		21.10.2021	0.1	2: Light breeze
15		21.10.2021	0.2	3: Gentle breeze
16		21.10.2021	0.2	3: Gentle breeze

Table B.2: Data overview of all conducted test flights - part 1

Flightnr	Duration (s)	Segment	Duration (s)	Frequency (Hz)
1	3491	1	595	0.0252
		2	596	0.0252
		3	563	0.0249
2	3820	1	599	0.0501
		2	580	0.0500
		3	597	0.0503
3	3213	1	589	0.1002
		2	590	0.1000
		3	590	0.1001
4	3221	1	560	0.0250
		2	560	0.0250
		3	562	0.0249
5	3620	1	598	0.1003
		2	580	0.1001
		3	580	0.1000
6	3424	1	596	0.0252
		2	559	0.0250
		3	560	0.0250
7	3513	1	600	0.0500
		2	598	0.0502
		3	581	0.0499
8	3600	1	619	0.0501
		2	598	0.0502
		3	580	0.0500
9	3402	1	588	0.1003
		2	590	0.1000
		3	590	0.1000
10	3665	1	596	0.0251
		2	592	0.0253
		3	559	0.0251
11	3689	1	560	0.0500
		2	580	0.0500
		3	580	0.0500
12	3291	1	588	0.1004
		2	579	0.1002
		3	579	0.1001
13	2794	1	565	0.0248
		2	558	0.0251
		3	557	0.0251
14	2898	1	578	0.0502
		2	581	0.0499
		3	200	0.0500
15	2681	1	589	0.1002
		2	589	0.1001
		3	580	0.1000
16	2858	1	580	0.1000
		2	579	0.1002
		3	280	0.1001

Table B.3: Data overview of all conducted test flights - part 2

Flightnr	TAS (m/s)				Height above ground (m)			
	mean	max	min	std	mean	max	min	std
	32.43	37.84	28.74	1.82	280.2	-218.7	-337.1	34.5
1	32.93	38.21	26.47	1.94	347.1	-312.7	-393.2	23.1
	31.72	38.26	26.44	1.92	345.2	-301.3	-447.9	32.5
	31.51	35.69	28.18	1.45	232.9	-208.4	-291.4	19.6
2	33.35	38.90	28.36	2.04	246.1	-223.3	-271.2	12.8
	34.45	39.10	30.58	1.67	236.9	-220.2	-268.1	12.4
	34.51	41.07	29.36	2.16	283.4	-235.4	-347.3	30.2
3	33.12	37.12	29.31	1.51	251.7	-185.2	-319.6	33.2
	34.05	37.38	30.14	1.40	286.3	-196.1	-344.2	40.5
	32.43	38.82	26.50	2.84	295.4	-255.0	-326.3	20.2
4	33.20	38.45	30.33	1.60	268.6	-233.0	-312.6	22.2
	33.04	39.07	28.06	2.59	291.2	-229.2	-331.0	24.1
	34.23	37.73	28.66	1.63	276.9	-233.1	-316.9	17.6
5	32.68	39.53	28.46	1.93	261.0	-180.3	-337.9	36.0
	32.48	37.20	26.34	1.92	347.4	-244.5	-379.1	29.3
	30.63	37.04	24.54	2.49	247.3	-203.2	-282.3	18.7
6	34.47	41.34	27.03	2.84	287.0	-240.1	-344.4	30.2
	32.23	38.38	26.62	2.55	291.1	-242.4	-329.8	21.9
	32.65	38.09	26.81	2.13	237.9	-201.8	-284.8	23.6
7	33.91	38.26	30.18	1.77	278.4	-231.1	-318.3	23.7
	32.43	39.89	24.88	2.14	232.3	-185.8	-269.1	21.3
	31.63	37.19	24.70	2.58	209.2	-179.9	-227.2	11.3
8	31.61	35.94	25.68	1.96	221.8	-199.5	-241.9	9.6
	29.45	35.61	23.53	2.31	220.0	-191.6	-240.9	10.4
	32.37	37.98	23.92	2.38	229.2	-206.7	-269.2	14.9
9	33.30	42.01	27.31	3.32	287.9	-220.1	-381.8	59.6
	32.98	38.80	26.26	1.83	297.3	-220.1	-351.2	35.1
	31.93	37.61	27.10	2.77	273.8	-255.8	-299.4	10.5
10	32.62	37.92	28.25	2.01	252.6	-208.3	-286.9	18.4
	31.79	42.28	24.94	3.45	255.2	-218.1	-306.5	20.1
	30.11	34.73	26.36	1.65	576.3	-511.8	-649.9	36.5
11	29.96	34.55	25.18	1.46	602.0	-554.6	-626.5	14.1
	33.99	37.68	29.08	1.70	683.6	-630.1	-728.5	28.6
	28.37	32.72	23.10	1.63	559.9	-519.0	-633.2	32.8
12	37.68	43.42	29.80	2.74	523.8	-471.0	-563.4	26.6
	30.48	35.27	25.41	1.80	533.0	-489.7	-559.7	14.8
	29.65	34.57	24.45	1.94	731.3	-627.0	-787.9	46.1
13	27.89	33.10	20.93	2.30	805.9	-704.0	-870.2	47.2
	28.17	32.78	22.20	1.91	834.2	-800.2	-878.2	20.7
	29.51	34.37	24.95	2.16	600.4	-543.2	-646.3	26.6
14	35.34	39.72	27.59	2.10	556.1	-502.7	-584.8	22.5
	32.68	36.07	29.35	1.57	562.2	-550.1	-574.8	5.8
	31.48	38.84	27.46	2.12	645.4	-585.2	-700.0	30.3
15	33.94	39.43	29.40	1.75	646.8	-589.5	-683.7	24.0
	30.95	34.97	25.13	1.74	614.5	-574.8	-653.3	23.3
	33.31	37.74	29.14	1.35	574.9	-516.6	-641.6	28.6
16	37.08	41.94	32.93	1.35	633.0	-604.1	-666.1	17.6
	33.99	35.89	31.27	1.04	543.0	-491.6	-595.4	39.5

Table B.4: Data overview of all conducted test flights - part 3

Flightnr	Wind at start (groundlevel)		Wind at landing (groundlevel)		Wind (m/s)			
	Dir (°)	Vel (m/s)	Dir (°)	Vel (m/s)	mean	max	min	std
1	340	3.087	339	2.572	1.418	1.478	1.359	0.035
					1.544	1.584	1.494	0.026
					1.603	1.618	1.589	0.009
2	VRB	1.543	330	2.572	1.207	1.240	1.174	0.019
					1.282	1.300	1.253	0.014
					1.294	1.298	1.292	0.002
3	90	3.087	80	3.601	4.509	4.640	4.365	0.080
					4.719	4.777	4.657	0.034
					4.846	4.882	4.792	0.028
4	100	3.601	80	4.630	3.907	3.977	3.822	0.045
					4.028	4.068	3.988	0.023
					4.147	4.191	4.093	0.028
5	110	4.630	100	4.116	4.727	4.795	4.647	0.043
					4.845	4.885	4.801	0.024
					4.955	4.992	4.908	0.025
6	260	4.630	250	5.144	5.767	5.883	5.627	0.074
					6.074	6.201	5.937	0.076
					6.236	6.241	6.222	0.005
7	260	6.173	250	7.202	5.801	5.909	5.691	0.063
					6.039	6.115	5.947	0.049
					6.181	6.231	6.129	0.030
8	230	3.087	220	4.116	5.812	5.950	5.669	0.081
					6.096	6.208	5.983	0.066
					6.266	6.283	6.226	0.017
9	220	6.173	230	5.144	4.680	4.778	4.576	0.059
					4.885	4.962	4.796	0.049
					4.989	5.002	4.969	0.010
10	230	5.659	220	4.116	5.469	5.642	5.276	0.106
					5.848	5.988	5.689	0.087
					6.087	6.148	6.017	0.037
11	220	6.688	230	5.659	15.738	16.056	15.369	0.198
					16.405	16.570	16.196	0.108
					16.699	16.757	16.605	0.045
12	210	5.144	200	5.144	12.836	13.170	12.434	0.212
					13.471	13.661	13.235	0.123
					13.779	13.802	13.710	0.026
13	210	8.231	230	7.717	17.687	18.108	17.222	0.255
					18.589	18.854	18.270	0.169
					19.063	19.116	18.952	0.049
14	150	1.543	160	2.058	6.180	6.315	6.025	0.084
					6.433	6.479	6.354	0.037
					6.483	6.484	6.480	0.001
15	220	4.116	210	3.087	7.192	7.316	7.045	0.078
					7.448	7.518	7.348	0.050
					7.496	7.522	7.457	0.020
16	200	4.116	260	4.116	4.901	4.985	4.799	0.054
					5.079	5.127	5.006	0.035
					5.114	5.124	5.101	0.007

Table B.5: Data overview of all conducted test flights - part 4

Flightnr	Roll angle φ (°)				Pitch angle θ (°)			
	mean	max	min	std	mean	max	min	std
	-0.02	22.40	-20.48	11.51	-0.23	6.13	-5.36	1.62
1	0.09	20.28	-21.41	11.21	-0.24	4.61	-6.90	1.76
	0.00	20.24	-21.17	11.48	-0.03	4.20	-5.57	1.66
	-0.29	19.72	-20.03	11.79	-0.50	5.09	-5.09	1.67
2	0.15	20.63	-21.72	12.01	-0.75	3.98	-4.83	1.63
	-0.04	20.28	-19.63	11.49	-1.17	4.10	-5.57	1.79
	-1.07	23.78	-25.09	13.54	0.01	7.80	-5.56	2.09
3	-0.65	22.07	-23.31	12.37	-0.87	5.36	-8.44	1.73
	0.07	22.35	-22.71	12.38	-0.93	3.72	-5.57	1.63
	-0.09	19.03	-20.06	11.77	-0.45	4.25	-4.90	1.44
4	0.37	19.94	-21.00	12.20	-0.73	3.26	-5.38	1.41
	-0.33	20.62	-20.94	12.66	-0.55	3.62	-6.22	1.69
	-0.83	24.04	-24.54	13.30	0.11	6.28	-6.22	1.83
5	-0.25	25.30	-23.99	13.29	0.01	7.03	-4.90	1.72
	-0.88	22.62	-23.64	12.52	0.22	5.36	-5.81	1.93
	-0.39	20.33	-20.50	12.94	-0.14	4.73	-4.25	1.44
6	0.15	21.76	-21.20	13.02	-0.23	5.09	-5.15	1.64
	0.05	21.42	-26.26	13.48	-0.19	4.43	-4.57	1.61
	-0.17	25.82	-29.20	14.79	0.14	7.46	-6.05	2.32
7	0.14	25.02	-26.45	13.52	-0.22	6.10	-6.73	2.00
	-0.41	25.16	-24.89	13.39	-0.13	5.83	-5.74	1.89
	-0.76	21.46	-24.25	13.30	-0.33	3.64	-6.10	1.31
8	0.14	23.65	-23.00	14.20	-0.18	4.22	-7.66	1.76
	-0.05	21.10	-22.38	13.31	-0.39	4.60	-5.56	1.54
	-0.77	26.35	-28.44	14.59	-0.24	7.11	-7.51	2.27
9	0.02	27.42	-24.61	13.85	-0.62	4.37	-5.38	1.74
	-1.13	26.69	-29.42	13.95	-0.76	3.90	-6.12	1.73
	-0.47	20.39	-20.95	12.50	-0.65	3.26	-5.35	1.27
10	0.13	21.57	-22.28	13.26	-0.07	4.72	-5.42	1.60
	-0.21	23.14	-23.13	13.10	-0.43	6.35	-8.09	1.82
	-0.91	21.82	-24.37	13.86	0.14	4.22	-5.44	1.83
11	-0.69	24.16	-24.46	13.39	-0.01	5.58	-5.47	1.91
	0.18	21.78	-21.81	12.67	0.58	6.47	-4.18	1.85
	-0.34	21.21	-23.62	12.53	-0.93	4.81	-6.19	2.38
12	-0.19	25.09	-22.36	12.76	-1.02	4.28	-4.82	1.85
	0.40	24.94	-23.54	12.56	-1.22	4.73	-7.24	2.04
	-1.12	20.23	-21.85	10.42	-0.58	4.33	-5.68	1.64
13	-0.73	22.35	-21.70	11.74	0.01	6.14	-6.01	1.76
	-0.94	23.24	-22.42	11.17	-0.40	4.36	-4.63	1.76
	0.02	21.60	-21.58	12.99	0.11	5.93	-4.73	1.98
14	-0.07	21.73	-21.78	13.02	-0.21	4.43	-4.64	1.84
	0.58	22.12	-21.92	12.62	-0.41	4.40	-4.62	1.54
	-0.18	24.14	-24.91	13.68	-0.11	7.52	-4.91	1.92
15	-0.15	22.35	-22.91	12.58	-0.44	5.70	-5.93	1.84
	-0.53	24.35	-23.70	13.16	-0.10	6.34	-4.82	1.92
	-0.45	21.19	-24.65	12.28	-0.84	4.15	-5.37	1.69
16	-0.09	24.19	-25.65	13.32	-0.93	5.78	-5.74	1.83
	-0.57	21.19	-23.01	12.23	-0.81	3.78	-4.54	1.58

Table B.6: Data overview of all conducted test flights - part 5

Flightnr	Roll angle rate p (°/s)				Pitch angle rate q (°/s)			
	mean	max	min	std	mean	max	min	std
	-0.05	6.58	-10.35	2.45	0.65	3.84	-2.39	0.90
1	-0.05	10.06	-7.43	2.39	0.63	4.08	-2.76	0.87
	-0.04	7.68	-7.80	2.46	0.63	4.17	-2.50	0.88
	0.05	9.94	-8.69	3.97	0.66	3.87	-2.50	0.88
2	0.04	9.41	-10.08	4.01	0.63	4.50	-2.26	0.86
	0.03	8.95	-9.13	3.86	0.55	4.66	-2.90	0.97
	-0.05	21.64	-16.54	8.84	0.63	5.53	-4.55	1.31
3	0.00	15.69	-17.34	8.14	0.48	4.49	-5.04	1.23
	-0.02	15.25	-17.53	8.11	0.46	4.78	-4.36	1.15
	0.02	7.98	-8.10	2.40	0.72	5.03	-3.23	0.94
4	0.01	11.41	-8.72	2.59	0.68	4.86	-3.35	1.07
	0.02	11.86	-7.88	2.56	0.75	5.48	-3.36	1.10
	-0.06	16.72	-18.92	8.75	0.53	5.70	-4.88	1.33
5	-0.04	16.41	-18.85	8.73	0.50	4.77	-4.32	1.29
	-0.04	16.89	-17.10	8.32	0.42	5.35	-5.98	1.40
	0.02	9.13	-9.39	2.68	0.82	5.41	-2.62	1.06
6	0.04	8.27	-7.27	2.57	0.82	4.77	-3.22	1.00
	0.02	9.06	-8.89	2.74	0.88	4.98	-2.68	1.09
	-0.04	13.51	-12.90	5.21	0.93	5.34	-3.53	1.25
7	-0.06	12.04	-11.63	4.74	0.77	4.96	-4.01	1.18
	-0.04	12.76	-12.00	4.78	0.70	5.10	-4.22	1.15
	-0.02	10.60	-10.93	4.51	0.87	5.43	-2.91	1.09
8	-0.04	11.27	-12.29	4.77	0.92	6.00	-3.42	1.14
	-0.02	11.11	-12.99	4.52	0.82	5.85	-3.81	1.14
	0.03	17.65	-17.62	9.51	1.01	6.00	-5.31	1.64
9	-0.03	18.18	-18.23	8.97	0.90	5.77	-3.79	1.24
	-0.04	18.07	-21.32	9.16	0.88	6.62	-3.74	1.38
	0.02	8.42	-8.74	2.49	0.77	4.55	-2.81	0.98
10	0.02	10.25	-7.69	2.63	0.90	5.23	-4.06	1.06
	0.06	9.56	-7.46	2.65	0.84	5.03	-3.75	1.12
	-0.05	9.63	-10.55	4.63	0.81	4.14	-3.03	0.88
11	-0.06	9.88	-9.56	4.44	0.76	3.70	-2.41	0.86
	-0.06	9.87	-9.03	4.24	0.67	4.21	-3.43	0.92
	0.07	16.29	-17.07	8.08	0.60	5.20	-4.36	1.65
12	0.03	15.13	-14.52	8.20	0.62	4.45	-4.05	1.24
	0.04	16.07	-15.91	8.04	0.51	5.03	-4.26	1.33
	-0.03	7.82	-8.25	2.38	0.48	4.89	-2.30	0.86
13	-0.05	8.97	-10.42	2.79	0.57	4.68	-4.08	1.09
	-0.04	8.81	-7.71	2.46	0.51	4.07	-2.65	0.88
	0.07	10.10	-10.07	4.29	0.84	4.21	-2.60	0.95
14	0.04	9.40	-8.88	4.29	0.81	5.14	-2.98	0.99
	0.06	7.90	-9.36	4.23	0.74	3.93	-2.49	0.92
	0.02	18.96	-16.21	8.91	0.76	6.79	-5.25	1.24
15	0.01	15.47	-13.69	8.22	0.64	4.45	-5.42	1.19
	0.01	14.25	-14.93	8.55	0.71	4.41	-5.21	1.27
	0.02	12.71	-14.89	7.88	0.51	4.49	-4.50	1.15
16	0.04	14.34	-14.40	8.50	0.69	5.96	-3.42	1.30
	0.03	13.24	-14.04	7.89	0.56	4.78	-4.03	1.20

C Pre-flight Questionnaire

Bo105 Kinetose Flugversuche Name: Klicken oder tippen Sie hier, um Text einzugeben.

Vor-Fragebogen BO 105 Kinetose Flugversuche

Name	Klicken oder tippen Sie hier, um Text einzugeben.
Alter	Klicken oder tippen Sie hier, um Text einzugeben.
Gewicht (circa)	Klicken oder tippen Sie hier, um Text einzugeben.
Höhe (circa)	Klicken oder tippen Sie hier, um Text einzugeben.

Einleitung

Kinetose ist der Überbegriff für verschiedene Formen der Bewegungskrankheit (Seekrankheit, Luftkrankheit, Autokrankheit, Simulatorkrankheit). Dieser Vor-Fragebogen soll Ihre bisherigen Erfahrungen mit Kinetose in verschiedenen Transportmitteln abfragen.

Die Abkürzung „Boot (kl.)“ steht für kleine Boote, also Ruderboote, kleine Segeljollen oder ähnliches.

Die Abkürzung „Flugzeug (kl.)“ bezeichnet in diesem Fragebogen kleine Flugzeuge. Gemeint sind „General Aviation“ Luftfahrzeuge, also Segelflugzeuge, Ultraleichtflugzeuge, Kleinflugzeug (Cessnas, etc.).

Bitte kreuzen Sie die Kästchen mit einem Mausklick an, damit diese anschließend automatisch ausgewertet werden können.

Bitte füllen Sie den nachfolgenden Fragebogen vollständig aus.

Bei Fragen, Anregungen oder Kommentaren wenden Sie sich bitte an mich entweder unter der Durchwahl 2663 oder unter philippe.petit@dlr.de.

1. In einem durchschnittlichen **Jahr**, wie oft haben Sie eines der folgenden Transportmittel als **Passagier** verwendet?

	Nie	1	2-3	4-15	16-63	64-255	256+
Auto	☐	☐	☐	☐	☐	☐	☐
Bus	☐	☐	☐	☐	☐	☐	☐
Fernbus	☐	☐	☐	☐	☐	☐	☐
Boot (kl.)	☐	☐	☐	☐	☐	☐	☐
Schiff	☐	☐	☐	☐	☐	☐	☐
Flugzeug (kl.)	☐	☐	☐	☐	☐	☐	☐
Flugzeug	☐	☐	☐	☐	☐	☐	☐
Zug	☐	☐	☐	☐	☐	☐	☐
Hubschrauber	☐	☐	☐	☐	☐	☐	☐

2. In einem durchschnittlichen **Jahr**, wie oft empfanden Sie Übelkeit in einem der folgenden Transportmittel (als **Passagier**)?

	Nie	1	2	3	4-7	8-15	16+
Auto	☐	☐	☐	☐	☐	☐	☐
Bus	☐	☐	☐	☐	☐	☐	☐
Fernbus	☐	☐	☐	☐	☐	☐	☐
Boot (kl.)	☐	☐	☐	☐	☐	☐	☐
Schiff	☐	☐	☐	☐	☐	☐	☐
Flugzeug (kl.)	☐	☐	☐	☐	☐	☐	☐
Flugzeug	☐	☐	☐	☐	☐	☐	☐
Zug	☐	☐	☐	☐	☐	☐	☐
Hubschrauber	☐	☐	☐	☐	☐	☐	☐

Bo105 Kinetose Flugversuche Name: Klicken oder tippen Sie hier, um Text einzugeben.

Hinweis zu den folgenden Fragen: Falls Sie das entsprechende Transportmittel nicht verwendet haben, machen Sie bitte ein Kreuz bei „nie“.

3. In einem durchschnittlichen **Jahr**, wie oft haben Sie sich als **Passagier** in einem der folgenden Transportmittel übergeben?

	Nie	1	2	3	4-7	8-15	16+
Auto	☐	☐	☐	☐	☐	☐	☐
Bus	☐	☐	☐	☐	☐	☐	☐
Fernbus	☐	☐	☐	☐	☐	☐	☐
Boot (kl.)	☐	☐	☐	☐	☐	☐	☐
Schiff	☐	☐	☐	☐	☐	☐	☐
Flugzeug (kl.)	☐	☐	☐	☐	☐	☐	☐
Flugzeug	☐	☐	☐	☐	☐	☐	☐
Zug	☐	☐	☐	☐	☐	☐	☐
Hubschrauber	☐	☐	☐	☐	☐	☐	☐

Die folgenden Fragen beziehen sich auf Ihre gesamten bisherigen Erfahrungen mit den genannten Transportmitteln.

4. Haben Sie Hitzewallungen oder Schwitzen Sie häufig in einer der folgenden Transportmittel, wenn Sie dieses als **Passagier** verwenden?

	Nie	Manchmal	Oft	Immer
Auto	☐	☐	☐	☐
Bus	☐	☐	☐	☐
Fernbus	☐	☐	☐	☐
Boot (kl.)	☐	☐	☐	☐
Schiff	☐	☐	☐	☐
Flugzeug (kl.)	☐	☐	☐	☐
Flugzeug	☐	☐	☐	☐
Zug	☐	☐	☐	☐
Hubschrauber	☐	☐	☐	☐

5. Leiden Sie unter Kopfschmerzen, wenn Sie in einem der folgenden Transportmittel als **Passagier** reisen?

	Nie	Manchmal	Oft	Immer
Auto	☐	☐	☐	☐
Bus	☐	☐	☐	☐
Fernbus	☐	☐	☐	☐
Boot (kl.)	☐	☐	☐	☐
Schiff	☐	☐	☐	☐
Flugzeug (kl.)	☐	☐	☐	☐
Flugzeug	☐	☐	☐	☐
Zug	☐	☐	☐	☐
Hubschrauber	☐	☐	☐	☐

6. Werden sie gelegentlich Blass (Sie verlieren Ihre Hautfarbe) oder verändert sich Ihre Hautfarbe, wenn Sie in einem der folgenden Transportmittel als **Passagier** reisen?

	Nie	Manchmal	Oft	Immer
Auto	☐	☐	☐	☐
Bus	☐	☐	☐	☐
Fernbus	☐	☐	☐	☐
Boot (kl.)	☐	☐	☐	☐
Schiff	☐	☐	☐	☐
Flugzeug (kl.)	☐	☐	☐	☐
Flugzeug	☐	☐	☐	☐
Zug	☐	☐	☐	☐
Hubschrauber	☐	☐	☐	☐

7. Leiden Sie unter Hypersalivation (Übermäßiger Speichelfluss), wenn Sie in einem der folgenden Transportmittel als **Passagier** reisen?

	Nie	Manchmal	Oft	Immer
Auto	☐	☐	☐	☐
Bus	☐	☐	☐	☐
Fernbus	☐	☐	☐	☐
Boot (kl.)	☐	☐	☐	☐
Schiff	☐	☐	☐	☐
Flugzeug (kl.)	☐	☐	☐	☐
Flugzeug	☐	☐	☐	☐
Zug	☐	☐	☐	☐
Hubschrauber	☐	☐	☐	☐

8. Werden Sie gelegentlich schläfrig oder müde, wenn Sie in einem der folgenden Transportmittel als **Passagier** reisen?

	Nie	Manchmal	Oft	Immer
Auto	☐	☐	☐	☐
Bus	☐	☐	☐	☐
Fernbus	☐	☐	☐	☐
Boot (kl.)	☐	☐	☐	☐
Schiff	☐	☐	☐	☐
Flugzeug (kl.)	☐	☐	☐	☐
Flugzeug	☐	☐	☐	☐
Zug	☐	☐	☐	☐
Hubschrauber	☐	☐	☐	☐

9. Fühlen Sie sich gelegentlich schwindelig oder benommen, wenn Sie in einem der folgenden Transportmittel als **Passagier** reisen?

	Nie	Manchmal	Oft	Immer
Auto	☐	☐	☐	☐
Bus	☐	☐	☐	☐
Fernbus	☐	☐	☐	☐
Boot (kl.)	☐	☐	☐	☐
Schiff	☐	☐	☐	☐
Flugzeug (kl.)	☐	☐	☐	☐
Flugzeug	☐	☐	☐	☐
Zug	☐	☐	☐	☐
Hubschrauber	☐	☐	☐	☐

10. Fühlen Sie sich gelegentlich schlecht (Unwohlsein im Magen, Übelkeit), wenn Sie in einem der folgenden Transportmittel als **Passagier** reisen?

	Nie	Manchmal	Oft	Immer
Auto	☐	☐	☐	☐
Bus	☐	☐	☐	☐
Fernbus	☐	☐	☐	☐
Boot (kl.)	☐	☐	☐	☐
Schiff	☐	☐	☐	☐
Flugzeug (kl.)	☐	☐	☐	☐
Flugzeug	☐	☐	☐	☐
Zug	☐	☐	☐	☐
Hubschrauber	☐	☐	☐	☐

Bo105 Kinetose Flugversuche Name: Klicken oder tippen Sie hier, um Text einzugeben.

11. Haben Sie sich jemals übergeben, wenn Sie in einer der folgenden Transportmittel als Passagier reisen?

	Ja	Nein
Auto	☐	☐
Bus	☐	☐
Fernbus	☐	☐
Boot (kl.)	☐	☐
Schiff	☐	☐
Flugzeug (kl.)	☐	☐
Flugzeug	☐	☐
Zug	☐	☐
Hubschrauber	☐	☐

12. Würden Sie eines der folgenden Transportmittel aufgrund von Kinetose (Bewegungskrankheit, Luftkrankheit, Seekrankheit etc.) vermeiden?

	Nie	Manchmal	Oft	Immer
Auto	☐	☐	☐	☐
Bus	☐	☐	☐	☐
Fernbus	☐	☐	☐	☐
Boot (kl.)	☐	☐	☐	☐
Schiff	☐	☐	☐	☐
Flugzeug (kl.)	☐	☐	☐	☐
Flugzeug	☐	☐	☐	☐
Zug	☐	☐	☐	☐
Hubschrauber	☐	☐	☐	☐

13. Wie anfällig würden Sie sich selbst hinsichtlich Kinetose (Bewegungskrankheit, Luftkrankheit, Seekrankheit etc.) einschätzen?

Viel anfälliger	☐
Etwas anfälliger als der Durchschnitt	☐
Durchschnittlich	☐
Etwas weniger anfällig als der Durchschnitt	☐
Viel weniger als der Durchschnitt	☐

14. Hatten Sie jemals einen schweren Unfall oder eine schwere Krankheit?

Ja: ☐ Nein: ☐

D Flight time series example

In the following a full complement of plots generated with the data recorded and estimated during flight 3 of the flight trials will be given. This serves as an example for all other flights which will not be displayed here as this would exceed the limits of this work.

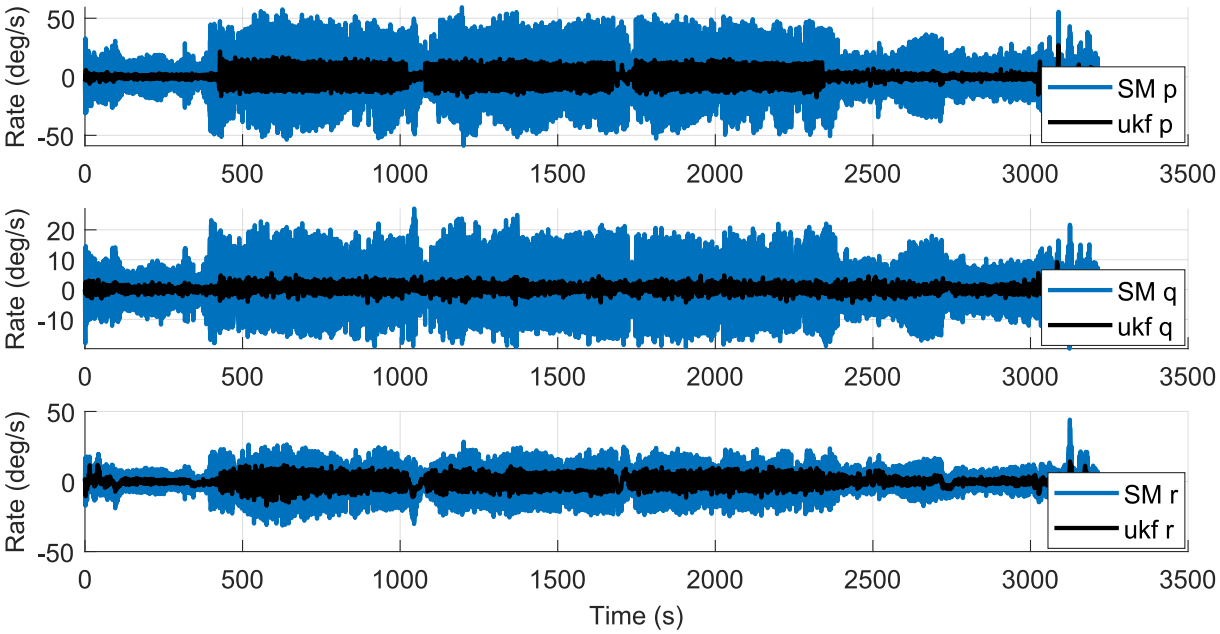

Figure D.1: Measured and estimated rotational velocities in body frame of flight 3. Smartphone measurements in blue, UKF estimation data in black

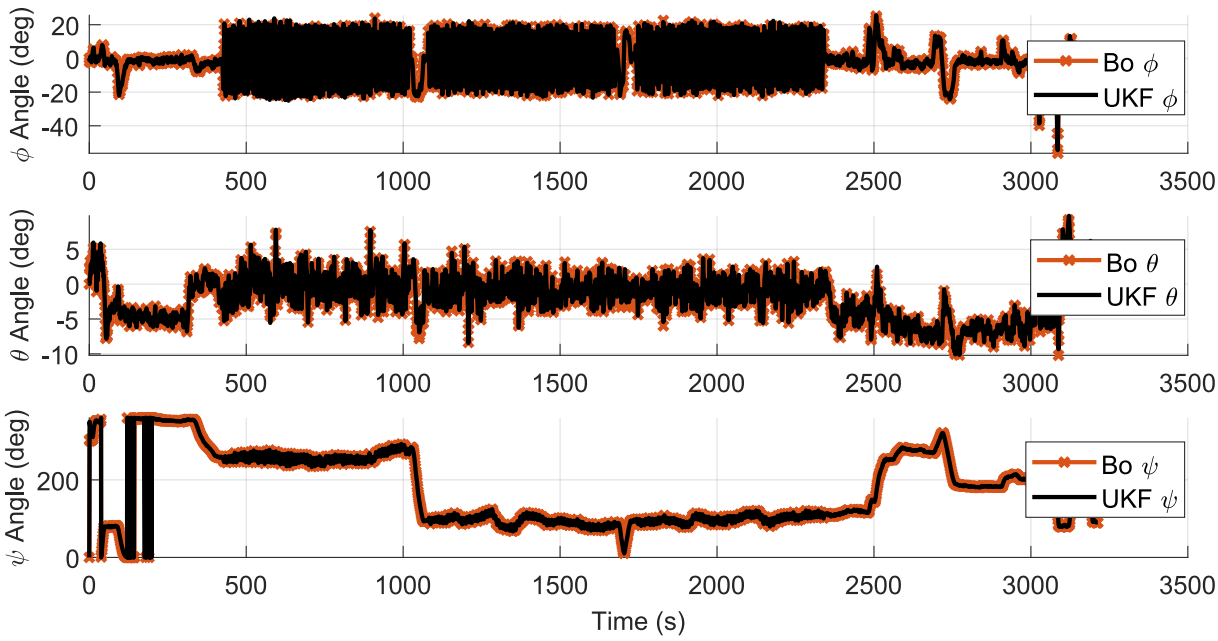

Figure D.2: Measured and estimated Euler angles of flight 3. G500H TXi measurement data in red, UKF estimation data in black

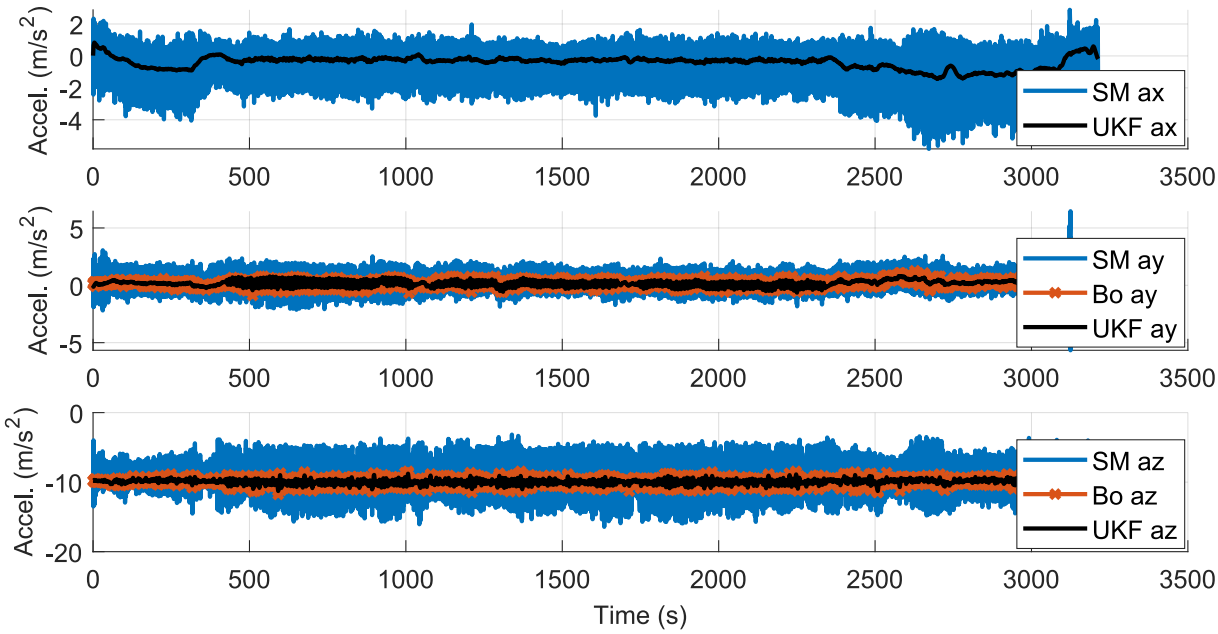

Figure D.3: Measured and estimated translational acceleration of Flight 3. Smartphone measurements in blue, G500H TXi measurement data in red, UKF estimation data in black

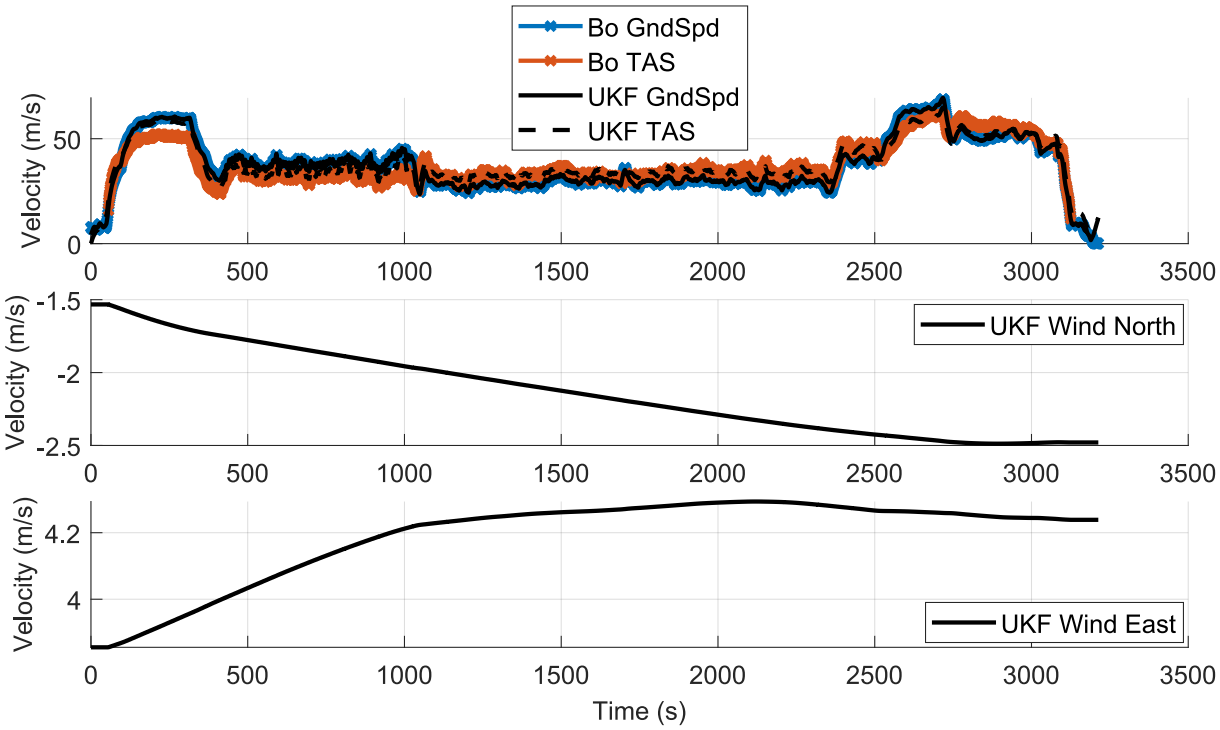

Figure D.4: Measured and estimated velocities and wind of flight 3. Groundspeed in blue, true airspeed in red, both measured by G500H TXi, UKF estimation data in black

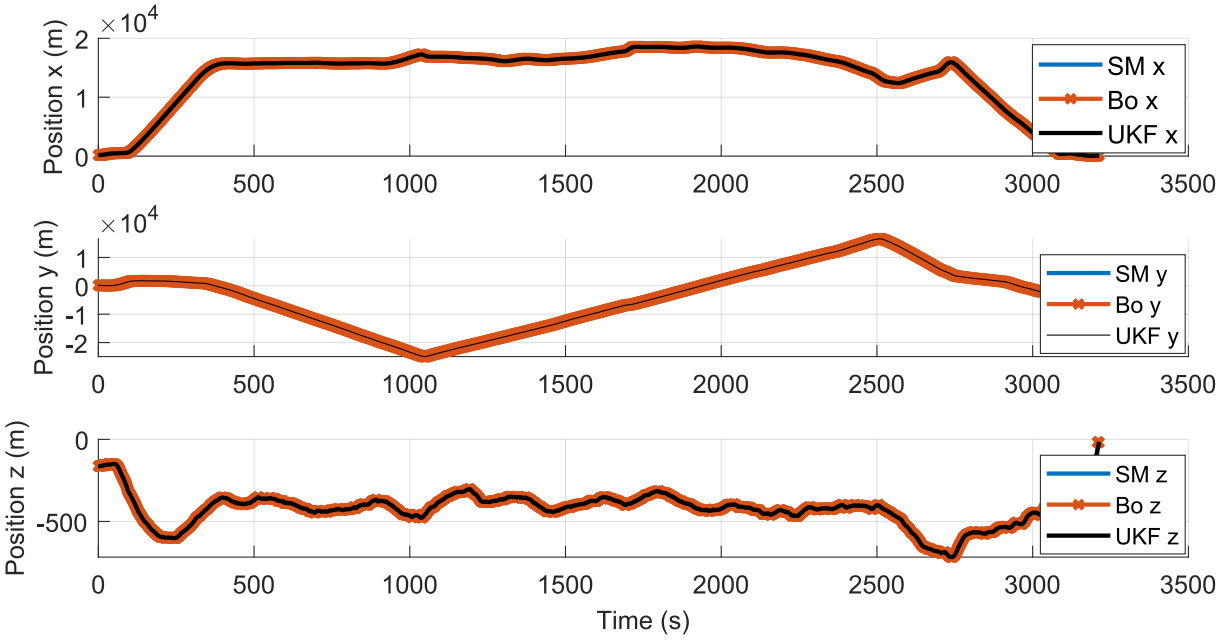

Figure D.5: Measured and estimated translational position of Flight 3. Smartphone measurements in blue, G500H TXi measurement data in red, UKF estimation data in black

Bibliography

[1] Whalley, M. S.; Takahashi, M. D.; Mansur, M. H.; Ott, C. R.; Minor, JS; Morford, Z. G.; Moralez, E.; Berrios, M.; Goerzen, C. L.; Schulein, G. J.: Flight Test Results for a New Mission-adaptive autonomy system on the rascal JUH-60A black hawk. In: *American Helicopter Society 72th Annual Forum*. West Palm Beach, Florida, May 2016

[2] Nonnenmacher, D. B.: *Automatische Stabilisierung von Hubschrauberaußenlasten an einer Rettungswinde*, TU Braunschweig, Dissertation, 2017

[3] Kim, H-M.: *Pilotenassistenzsystem zur automatischen Lastpositionierung bei Hubschrauber-Windeneinsätzen*, TU Braunschweig, Dissertation, 2017

[4] Zimmermann, M.: Flight test results of helicopter approaches with trajectory guidance based on in-flight acquired LiDAR data. In: *SPIE Defense and Commercial Sensing*. Baltimore, Maryland, USA, May 2016

[5] Frost, C.; Hindson, W.; Moralez III, E.; Tucker, G.; Dryfoos, J.: Design and Testing of Flight Control Laws on the RASCAL Research Helicopter. In: *AIAA Modeling and Simulation Technologies Conference and Exhibit*. Monterey, California, USA, August 2002

[6] Holden, J.; Goel, N.: Fast-forwarding to a Future of On-demand Urban Air Transportation. In: *Uber Elevate*. San Francisco, California, USA, October 2016

[7] Volocopter GmbH: *Volocopter's VoloCity Air Taxi for Commercial UAM Services*. `https://mediahub-volocopter.pixxio.media/collection/32/file/1016`, 2021. – [Accessed 18th January 2023, This image is copyright protected.]

[8] Joby Aero inc.: *Joby aircraft prototype in flight*. `https://drive.google.com/drive/folders/1t4toHp8bRrv25LDrKj0rdaauBQpwS6v2`, 2021. – [Accessed 18th January- 2023, Courtesy of Joby Aviation. This image is copyright protected.

[9] Aeronautical Design Standard: Performance Specifications - Handling Qualities Requirements for Military Rotorcraft - ADS-33E-PRF / US Army Aviation and Missile Command. Redstone Arsenal, Alabama, USA, March 2000. – Standard

[10] Volocopter GmbH: The Roadmap to scalable urban air mobility - White paper 2.0. (2021)

[11] Leatherwood, J. D.; Clevenson, S. A.; Hollenbaugh, D. D.: Evaluation of Ride Quality Prediction Methods for Helicopter Interior Noise and Vibration Environments - NASA-TP-2261 / National Aeronautics and Space Administration Hampton VA Langley Research Center. 1984. – Tech. Report

[12] Loewy, R. G.: Helicopter Vibrations: A Technological Perspective. In: *American Helicopter Society, Journal* 29 (1984), S. 4–30

[13] Reichert, G.: Helicopter vibration control: A survey. In: *Vertica* 5 (1981), S. 1–20

[14] Rath, T.; Fichter, W.: A Closer Look at the Impact of Helicopter Vibrations on Ride Quality. In: *American Helicopter Society 73th Annual Forum*. Fort Worth, Texas, USA, May 2017, S. 9–11

[15] Ch., Kessler.: Active rotor control for helicopters: motivation and survey on higher harmonic control. In: *CEAS Aeronautical Journal* 1 (2011), S. 3–22

[16] ISO Central Secretary: ISO2631-1:1997(E) Mechanical vibration and shock-evaluation of human exposure to whole-body vibration - Part 1: General requirements / International Organization for Standardization. Geneva, Switzerland, March 1997. – Standard

[17] Money, K. E.: Motion sickness. In: *Physiological reviews* 50 (1970), Nr. 1, S. 1–39

[18] J., Ulbrich: *Entwicklung und Implementierung eines Vorhersagemodells für Kinetose in Hubschraubern*, RWTH Aachen, Master thesis, May 2022

[19] Griffin, M. J.; Howarth, H. V.: Motion Sickness History Questionnaire - Technical Report No. 283 / University of Southampton, ISVR. 2000. – Tech. Report

[20] Bos, J. E.; Bles, W.: Modelling motion sickness and subjective vertical mismatch detailed for vertical motions. In: *Brain Research Bulletin* 47 (1998), Nr. 5, S. 537–542

[21] Reason, J. T.; Brand, J. J.: *Motion Sickness*. Academic press, 1975

[22] Beeres, F.: *Fokus Physikum: 2018/2019: Band 4*. MIAMED GmbH, 2017 (Bd. 4)

[23] *The APT*. Wikimedia Commons, the free media repository `https://commons.wikimedia.org/w/index.php?title=File:APT_at_Crewe.jpg&oldid=633543667`, 2022. – Accessed 13 January 2023

[24] Förstberg, J.; Andersson, E.; Ledin, T.: Influence of different conditions for tilt compensation on symptoms of motion sickness in tilting trains. In: *Brain research bulletin* 47 (1998), Nr. 5, S. 525–535

[25] Beard, G. F.; Griffin, M. J.: Motion sickness caused by roll-compensated lateral acceleration: Effects of centre-of-rotation and subject demographics. In: *Proceedings of the Institution of Mechanical Engineers, Part F: Journal of Rail and Rapid Transit* 228 (2014), Nr. 1, S. 16–24

[26] Andersson, E.; Nilstam, N.: The development of advanced high speed vehicles in Sweden. In: *Proceedings of the Institution of Mechanical Engineers, Part D: Transport Engineering* 198 (1984), Nr. 4, S. 229–237

[27] Suzuki, H.; Shiroto, H.; Tanaka, A.; Tezuka, K.; Takai, H.: Psychophysical Evaluation of Railway Vibrational Discomfort on Curved Sections. In: *Quarterly report of the Railway Technical Research Institute* 41 (2000), Nr. 3, S. 106–111

[28] Persson, R.: Tilting trains: technology, benefits and motion sickness / KTH, Aeronautical and Vehicle Engineering, Rail Vehicles. 2008. – Tech. Report

[29] Cutler, M.; Ure, N.-K.; Michini, B.; How, J.: Comparison of Fixed and Variable Pitch Actuators for Agile Quadrotors. In: *AIAA guidance, navigation, and control conference*, 2011, S. 6406

[30] Bahr, M.; Hebbar, U.; Ferede, E.; Gandhi, F.: Multi-rotor eVTOL Flight Simulation and Assessment under Atmospheric Turbulence. In: *77th Vertical Flight Society Forum and Technology Display*. Virtual, May 2021

[31] O'Hanlon, J. F.; McCauley, M. E.: Motion Sickness Incidence as a Function of the Frequency and Acceleration of Vertical Sinusoidal Motion. In: *Aviation, Space, and Environmental Medicine* 45 (1974), S. 366—-369

[32] Turner, M.; Griffin, M. J.; Holland, I.: Airsickness and Aircraft Motion during Short-Haul Flights. In: *Aviation, space, and environmental medicine* 71 (2000), Nr. 12, S. 1181–1189

[33] Aeronautical Design Standard: Requirements for Rotorcraft Vibration Specifications, Modeling and Testing / US Army Aviation and Missile Command. Redstone Arsenal, Alabama, USA, May 2006. – Standard

[34] Leatherwood, J. D.; Dempsey, T. K.; Clevenson, S. A.: A Design Tool for Estimating Passenger Ride Discomfort Within Complex Ride Environments. In: *Human Factors* 22 (1980), Nr. 3, S. 291–312

[35] Donohew, B. E.; Griffin, M. J.: Motion Sickness: Effect of the Frequency of Lateral Oscillation. In: *Aviation, Space, and Environmental Medicine* 75 (2004), Nr. 1, S. 649–656

[36] *12-m Tilting and Translating Cabin*. `https://www.southampton.ac.uk/hfru/laboratory-facilities/12m-tilting.page`, . – Accessed: 30th November 2022

[37] McCauley, M. E.; Royal, J. W.; Wylie, C. D.; O'Hanlon, J. F.; Mackie, R. R.: Motion sickness incidence: Exploratory studies of habituation, pitch and roll, and the refinement of a mathematical model / Canyon Research Group Inc Goleta Ca Human Factors Research Div. 1976. – Tech. Report

[38] Donohew, B. E.; Griffin, M. J.: Low frequency motions and motion sickness on a tilting train. In: *Proceedings of the Institution of Mechanical Engineers, Part F: Journal of Rail and Rapid Transit* 221 (2006), Nr. 1, S. 125–133

[39] Donohew, B. E.; Griffin, M. J.: Motion Sickness with Fully Roll-compensated Lateral Oscillation: Effect of Oscillation Frequency. In: *Aviation, Space, and Environmental Medicine* 80 (2009), Nr. 2, S. 94–101

[40] Donohew, B. E.; Griffin, M. J.: Motion Sickness with Combined Lateral and Roll Oscillation: Effect of Percentage Compensation. In: *Aviation, Space, and Environmental Medicine* 81 (2010), Nr. 1, S. 22–29

[41] Joseph, J. A.; Griffin, M. J.: Motion Sickness from Combined Lateral and Roll Oscillation: Effect of Varying Phase Relationships. In: *Aviation, Space, and Environmental Medicine* 78 (2007), Nr. 10, S. 944–950

[42] Joseph, J. A.; Griffin, M. J.: Motion Sickness: Effect of the Magnitude of Roll and Pitch Oscillation. In: *Aviation, Space, and Environmental Medicine* 79 (2008), Nr. 4, S. 390–396

[43] Joseph, J. A.; Griffin, M. J.: Motion Sickness: Effect of Changes in Magnitude of Combined Lateral and Roll Oscillation. In: *Aviation, Space, and Environmental Medicine* 79 (2008), Nr. 11, S. 1019–1027

[44] Kamiji, N.; Kurata, Y.; Wada, T.; Doi, S.: Modeling and Validation of Carsickness Mechanism. In: *SICE Annual Conference 2007* IEEE, 2007, S. 1138–1143

[45] Petit, P. J.: Prediction of Motion Sickness Onset for Vertical Lift Applications. In: *77th Vertical Flight Society Forum and Technology Display*. Virtual, May 2021

[46] Petit, P. J.: Prediction of Motion Sickness Onset for Vertical Lift Applications. In: *Journal of the American Helicopter Society* 68 (2022), December

[47] Griffin, M. J.; Kim, M. L.: Effect of Frequency and Direction of Horizontal Oscillation on Motion Sickness. In: *Aviation, Space, and Environmental Medicine* 73 (2002), Nr. 6, S. 537–543

[48] Jones, M.; White, M.; Fell, T.; Barnett, M.: Analysis of mMtion Parameter Variations for Rotorcraft Flight Simulators. In: *American Helicopter Society 73th Annual Forum*. Fort Worth, Texas, May 2017, S. 1812–1833

[49] Schmidt, S.; Conrad, B.: *Motion drive signals for pilot flight simulators*. National Aeronautics and Space Administration, 1970

[50] Natal, G.; Arjoni, D.; Oliveira, W.; Rodamilans, G.; Silva, E.; Silveira, L.; Villani, E.; Trabasso, L.: Implementation analysis of a washout filter on a robotic flight simulator-A case study. In: *Journal of Aerospace Technology and Management* 11 (2019)

[51] Springer, K.; Gattringer, H.; Bremer, H.: Towards washout filter concepts for motion simulators on the base of a Stewart platform. In: *PAMM* 11 (2011), Nr. 1, S. 955–956

[52] Leung, A.; Hon, K. L.: Motion sickness: an overview. In: *Drugs in context* 8 (2019)

[53] Müllhäuser, M.; Lusardi, J.: US-German Joint In-flight and Simulator Evaluation of Collective Tactile Cueing for Torque Limit Avoidance: Shaker versus Soft Stop. In: *Journal of the American Helicopter Society* 67 (2022), Nr. 3, S. 69–84

[54] Wang, Y.; White, M.; Owen, I.; Hodge, S.; Barakos, G.: Effects of visual and motion cues in flight simulation of ship-borne helicopter operations. In: *CEAS Aeronautical Journal* 4 (2013), Nr. 4, S. 385–396

[55] Simpson, B. D.; Brungart, D. S.; Gilkey, R. H.; Cowgill, J. L.; Dallman, R. C.; Green, R. F.; Youngblood, K. L.; Moore, T. J.: 3D audio cueing for target identification in a simulated flight task. In: *Proceedings of the Human Factors and Ergonomics Society Annual Meeting* Bd. 48, 2004, S. 1836–1840

[56] Schmerwitz, Sven; Müllhäuser, Mario; Wartmann, Johannes; Ernst, Johannes M.: Multimodal cueing and short-term pilot interaction during helicopter low-level operation under automatic trajectory following. In: *Virtual, Augmented, and Mixed Reality (XR) Technology for Multi-Domain Operations III* Bd. 12125 SPIE, International Society for Optics and Photonics, 2022

[57] Garmin Ltd.: *G500(H)/G600/G700 TXi Pilot's Guide*, January 2022. – Version: 190-01717-10 - Revision M

[58] DIN 9300: Begriffe, Größen und Formelzeichen der Flugmechanik. Berlin, October 1990. – Standard

[59] RTCA, Inc.: Minimum Operational Performance Standards (MOPS) for Strapdown Attitude and Heading Reference Systems (AHRS). Washington DC, USA, March 2012. – Standard

[60] European Aviation Safety Agency (EASA): Easy Access Rules for European Technical Standard Orders (CS-ETSO)(Amendment 14). Cologne, Germany, November 2018. – Standard

[61] Garmin Ltd.: *GSU 75 ADAHRS Installation Manual*, May 2017. – Version: 190-01639-00 - Revision 6

[62] Google Inc.: *Android Developer Guide*, June 2022

[63] Rhudy, M.: Time Alignment Techniques for Experimental Sensor Data. In: *International Journal of Computer Science and Engineering Survey* 5 (2014), Nr. 2, S. 1

[64] Rabiner, L. R.; Gold, B.: *Theory and Application of Digital Signal Processing*. Michigan, USA : Englewood Cliffs: Prentice-Hall, 1975

[65] Kalman, R. E.: A New Approach to Linear Filtering and Prediction Problems. In: *Transactions of the ASME–Journal of Basic Engineering* 82 (Series D) (1960)

[66] McGee, L. A.: *Discovery of the Kalman filter as a Practical Tool for Aerospace and Industry*. Bd. 86847. National Aeronautics and Space Administration, 1985

[67] Pasricha, G. K.: Kalman Filter and its Economic Applications. (2006). `https://mpra.ub.uni-muenchen.de/22734/`

[68] Petit, P. J.: The Extended/Unscented Kalman Filter of DLR's ACT/FHS / Deutsches Luft-und Raumfahrt Zentrum. 2018. – Tech. Report

[69] Julier, S. J.; Uhlmann, J. K.: A New Extension of the Kalman Filter to Nonlinear Systems. In: *Signal processing, sensor fusion, and target recognition VI* Bd. 3068. Orlando, Florida, USA, 1997, S. 182–193

[70] Van Der Merwe, R.; Wan, E. A.: The square-root unscented Kalman filter for state and parameter-estimation. In: *International Conference on Acoustics, Speech, and Signal Processing* Bd. 6. Salt Lake City, UT, USA, May 2001, S. 3461–3464

[71] Merwe, R. van d.; Wan, E. A.: Sigma-Point Kalman Filters for Integrated Navigation. In: *Proceedings of the 60th Annual Meeting of the Institute of Navigation*. Dayton, Ohio, USA, July 2004, S. 641–654

[72] Wartmann, J.; Wolfram, J.; Gestwa, M.: Sensor fusion and flight path reconstruction of the ACT/FHS rotorcraft. In: *CEAS Aeronautical Journal* 6 (2015), Nr. 4, S. 529–539

[73] Särkkä, S.: Unscented Rauch–Tung–Striebel Smoother. In: *IEEE transactions on automatic control* 53 (2008), Nr. 3, S. 845–849

[74] Teixeira, Bruno O.; Tôrres, Leonardo A.; Iscold, Paulo; Aguirre, Luis A.: Flight path reconstruction – A comparison of nonlinear Kalman filter and smoother algorithms. In: *Aerospace Science and Technology* 15 (2011), Nr. 1, S. 60–71

[75] Thompson, S. K.: *Sampling*. Bd. 755. John Wiley & Sons, 2012

[76] Ostertagova, E.; Ostertag, O.; Kováč, J.: Methodology and Application of the Kruskal-Wallis Test. In: *Applied Mechanics and Materials* 611 (2014), S. 115–120

[77] Lange, T.; Mosler, K.: *Statistik kompakt–Basiswissen für Ökonomen und Ingenieure*. Springer-Lehrbuch, 2017

[78] Montgomery, D. C.; Runger, G. C.: *Applied statistics and probability for engineers*. John Wiley & Sons, 2010

[79] Crocker, L.; Algina, J.: *Introduction to classical and modern test theory*. Michigan : Holt, Rinehart, and Winston, 1986

[80] *Passagiere im Simulator: DLR nimmt Passagierkabine für den Air Vehicle Simulator (AVES) in Betrieb*. `https://www.dlr.de/content/de/artikel/news/2018/4/20181017_passagierkabine-air-vehicle-simulator.html`, . – Accessed: 17th October 2022

[81] Miermeister, P.; Lächele, M.; Boss, R.; Masone, C.; Schenk, Ch.; Tesch, J.; Kerger, M.; Teufel, H.; Pott, A.; Bülthoff, H.: The CableRobot Simulator Large Scale Motion Platform Based on Cable Robot Technology. In: *IEEE, International Conference on Intelligent Robots and Systems*. Daejeon, South Korea, December 2016, S. 3024–3029

[82] Özkurt, S.; Fichter, W.; Bülthoff, H.; Fischer, C.: On the Impact of Flight Control Systems on Kinetosis of Helicopter Passengers. In: *78th Vertical Flight Society Forum and Technology Display*. Red Hook, New York, USA, May 2022

ISSN 1434-8454

ISRN DLR-FB--2024-16